

UNIVERSITY OF CALGARY

Downhole Weight on Bit Prediction with Analytical Model and Finite Element Method

by

Lingyun Lei

A THESIS

SUBMITTED TO THE FACULTY OF GRADUATE STUDIES

IN PARTIAL FULFILMENT OF THE REQUIREMENTS FOR THE

DEGREE OF MASTER OF SCIENCE

GRADUATE PROGRAM IN CHEMICAL AND PETROLEUM ENGINEERING

CALGARY, ALBERTA

JUNE, 2014

© Lingyun Lei 2014

ABSTRACT

Horizontal drilling is an innovative technology applied for exploiting unconventional resources in North-America and around the world.

To acquire better drilling performance, weight on bit (WOB) needs to be accurate and monitored. However, the weight on bit recorded on the surface panel is most often incorrect because wellbore friction along the drillstring is not considered. Drillstring force modeling computer simulation can be utilized to economically determine the actual WOB value. In this thesis, two drillstring force models are programmed and compared: an analytical model and a finite element method (FEM). In conclusion the analytical model computes faster, but FEM is more accurate.

Simulations are performed to verify and compare both methods, where friction factors and WOB are calculated for a horizontal well in Western Canada, in a depth interval from 2500m to 3800m. The results from both methods are comparable to results obtained from measured downhole WOB (DOWB).

ACKNOWLEDGEMENTS

I would like to express my appreciation to my supervisor Dr. Geir Hareland for his supervision, advice and guidance all the way through my research work at the University of Calgary. Thank you for being so inspiring and for your trust in giving me enough space to deal with research obstacles.

I also want to thank Dr. Zebing Wu for his inspiration, expertise and unconditional help and contributions while programming the torque and drag analytical model and the finite element method.

Special thanks to Ms. Patricia Teichrob for arranging and organizing meetings and paperwork.

My gratitude is also expanded to my friend Mr. Dongcheng Deng. Your professional C/C++ programming knowledge greatly helped the program debugging process.

I am deeply thankful to the Department of Chemical and Petroleum Engineering, University of Calgary for granting me the chance to pursue my Master of Science degree.

Last but not the least I would thank my family for their unconditional love, trust and support. Your love will always lighten my way in darkness.

TABLE OF CONTENTS

ABSTRACT.....	2
ACKNOWLEDGEMENTS.....	3
TABLE OF CONTENTS.....	4
LIST OF TABLES.....	6
LIST OF FIGURES.....	7
NOMENCLATURE.....	9
Chapter 1 : INTRODUCTION	1
1.1 Recourses in Canada	1
1.2 Drilling Technologies for Unconventional Reservoir.....	2
1.3 Challenges for Directional Drilling.....	4
1.4 Solutions for Challenges.....	5
1.5 Auto-Driller System	6
Chapter 2 : LITERATURE REVIEW	7
2.1 Analytical Model	7
2.2 Finite Element Method	11
Chapter 3 : ANALYTICAL MODEL.....	15
3.1 Buoyancy Factor.....	17
3.2 Straight Section	18
3.3 Curved Section	20
3.4 Combined Axial Motion and Rotation.....	25
3.5 Other Factors	27
Chapter 4 : FINITE ELEMENT METHOD	28
4.1 Hamilton’s Principle	28
4.2 3-D Beam Element	28
4.3 Discrete System.....	30
4.4 The Mass Matrix.....	30
4.5 The Stiffness Matrix	32
4.6 The Damping Matrix.....	35
4.7 Gravity Force Vector	37
4.8 Horizontal Model	38
4.9 Global Matrixes	43

4.10 Boundary Conditions.....	44
4.11 Solution – Wilson Theta Method	48
4.12 Stabilizer.....	50
4.13 Computational Logic	52
4.14 Programming Language	54
Chapter 5 : SIMULATION EXPERIMENTS.....	55
5.1 Field Data	55
5.1.1 Survey Data	55
5.1.2 Real-time Drilling Data	58
5.1.3 Data Choosing Principle	59
5.2 Calculation with Analytical Model	65
5.3 Calculation with FEM	73
5.3 Discussion.....	83
5.3.1 Friction Factors.....	83
5.3.2 Weight on Bit	84
Chapter 6 : CONCLUSIONS AND RECOMMENDATIONS.....	89
Reference	90

LIST OF TABLES

Table 5.1 Drillstring Components	58
Table 5.2 Real-time Drilling Data from 2505.3m to 2505.99m	60
Table 5.3 Depth versus SWOB	61
Table 5.4 Depth Versus SWOB	63
Table 5.5 Friction Factor from 2500m to 2800m.....	65
Table 5.6 CoPilot-DWOB and Analytical-DWOB from 2500m to 2800m.....	66
Table 5.7 Friction Factor from 2800m to 3100m.....	67
Table 5.8 CoPilot-DWOB and Analytical-DWOB from 2800m to 3100m.....	68
Table 5.9 Friction Factor from 3100m to 3450m.....	69
Table 5.10 CoPilot-DWOB and Analytical-DWOB from 3100m to 3450m.....	70
Table 5.11 Friction Factor from 3450m to 3750m.....	71
Table 5.12 CoPilot-DWOB and Analytical-DWOB from 3450m to 3750m.....	72
Table 5.13 Friction Factor from 2500m to 2800m.....	75
Table 5.14 CoPilot-DWOB and FEM-DWOB from 2500m to 2800m	76
Table 5.15 Friction Factor from 2800m to 3100m.....	77
Table 5.16 CoPilot-DWOB and FEM-DWOB from 2800m to 3100m	78
Table 5.17 Friction Factor from 3100m to 3450m.....	79
Table 5.18 CoPilot-DWOB and FEM-DWOB from 3100m to 3450m	80
Table 5.19 Friction Factor from 3450m to 3750m.....	81
Table 5.20 CoPilot-DWOB and FEM-DWOB from 3450m to 3750m	82

LIST OF FIGURES

Figure 1.1 Conventional and Unconventional Recourse triangular chart	2
Figure 1.2 Brief Schematic of SAGD Technology	3
Figure 1.3 Flow chart of Auto-Driller System.....	6
Figure 2.1 Forces and Geometries of Various Curved Hole.....	8
Figure 2.2 Forces and Geometries for Curved Section	9
Figure 2.3 Bottom-hole Assembly Configurations.....	12
Figure 2.4 Bottom-hole Assembly Configurations.....	13
Figure 3.1 Schematic of 3-D Analytical Model.....	16
Figure 3.2 Schematic of Buoyancy Force	17
Figure 3.3 Force Analysis for Straight Section	19
Figure 3.4 Friction Analysis (Part one) for Curved Section	20
Figure 3.5 Friction Analysis (Part Two) for Curved Section	22
Figure 3.6 Johancsik Model for Compression Calculation	24
Figure 3.7 Drag and Torque for a Drillstring Element.....	25
Figure 3.8 Relationships between Hoisting/Lowering and Rotational Speed	26
Figure 4.1 Displacements and Rotations for Each Beam Element.....	29
Figure 4.2 Gravity Distributions for One Beam Element	37
Figure 4.3 Local and Global Coordinate systems for Horizontal Well	38
Figure 4.4 Global Coordinate and Local Coordinate system	39
Figure 4.5 Rotate around Z-axis.....	40
Figure 4.6 Rotate around Y-axis.....	41
Figure 4.7 Main Boundaries for Whole Well	45
Figure 4.8 Hole Size Constraint.....	48
Figure 4.9 Linear Change of Acceleration for a Dynamic Vibration System	49
Figure 4.10 Stabilizers with three different blades	51
Figure 4.11 Flowchart of FEM Program	53
Figure 5.1 Well Trajectory 3D Diagram.....	56
Figure 5.2 Well Trajectory Transversal Projection.....	57
Figure 5.3 Well Trajectory Top View.....	57
Figure 5.4 Off-bottom and On-bottom Scenarios	59

Figure 5.5 SWOB at Different Depth.....	62
Figure 5.6 Comparison Between CoPilot-DWOB and SWOB.....	64
Figure 5.7 Friction Factor from 2500m to 2800m	66
Figure 5.8 Comparison Between CoPilot-DWOB and Analytical-DWOB from 2500m to 2800m.	67
Figure 5.9 Friction Factor from 2800m to 3100m	68
Figure 5.10 Comparison Between CoPilot-DWOB and Analytical-DWOB from 2800m to 3100m	69
Figure 5.11 Friction Factor from 3100m to 3450m	70
Figure 5.12 Comparison Between CoPilot-DWOB and Analytical-DWOB from 3100m to 3450m	71
Figure 5.13 Friction Factor from 3450m to 3750m	72
Figure 5.14 Comparison Between CoPilot-DWOB and Analytical-DWOB from 3450m to 3750m	73
Figure 5.15 Iteration Procedures for Friction Factor Calculation	74
Figure 5.16 Friction Factor from 2500m to 2800m	75
Figure 5.17 Comparison Between CoPilot-DWOB and FEM-DWOB from 2500m to 2800m	76
Figure 5.18 Friction Factor from 2800m to 3100m	77
Figure 5.19 Comparison Between CoPilot-DWOB and FEM-DWOB from 2800m to 3100m	78
Figure 5.20 Friction Factor from 3100m to 3450m	79
Figure 5.21 Comparison Between CoPilot-DWOB and FEM-DWOB from 3100m to 3450m	80
Figure 5.22 Friction Factor from 3450m to 3750m	81
Figure 5.23 Comparison Between CoPilot-DWOB and FEM-DWOB from 3450m to 3750m	82
Figure 5.24 Comparison of Friction Factor for Analytical Model and FEM	83
Figure 5.25 WOB Comparison from 2500m to 2800m	84
Figure 5.26 WOB Comparison from 2800m to 3100m	85
Figure 5.27 WOB Comparison from 3100m to 3450m	85
Figure 5.28 WOB Comparison from 3450m to 3800m	86
Figure 5.29 WOB Comparison for Whole Well Path.....	87

NOMENCLATURE

α	Inclination angle, radian
β	Buoyancy factor
γ	Specific weight, N/m ³
ν	Poisson's ratio
μ	Friction coefficient
θ	Dogleg, rad/30m
η	Sheave efficiency
ρ	Density, kg/m ³
Ω	Rotational speed of drillstring, RPM
χ	Standpipe Coefficient
ψ	Angle between axial and tangential pipe velocities, radian
n	Number of lines
ϕ	Azimuth angle, radian
ϕ_x, ϕ_y, ϕ_z	Rotational displacement in local coordinate, m
Φ_x, Φ_y, Φ_z	Rotational displacement in global coordinate, m
ω	Unit length weight density, N/m
Δd	Clearance between wellbore and drill string, m
ΔL_i	Length of each element, m
Δt	Time step, s
A	Cross sectional area, m ²
D	Drillstring outer diameter, m
d	Drillstring inner diameter, m
F_{top}, F_{bottom}	Tension or compression at top and bottom of element, N
F_n	Normal force, N
HL_s	Hook Weight, N
HL_a	Adjusted Hookload, N

KH	Stiffness of the spring
I_{xy}, I_z	Axial or radial moment of inertia
J_z	Mass moment of inertia
T_{top}, T_{bottom}	Torque at top and bottom of element, N.m
R_α	Curve radius, m
q_x, q_z	Unit weight per meter on x-axis or z-axis direction, N/m
r	Drillstring diameter, m
spp	Standpipe pressure, Pa
U	Displacement on global coordinate system, m
u_x, u_y	Displacement in local coordinate x-axis or y-axis, m
V_h, V_r	Axial or tangential speed while hoisting/lower operation, m/s
X, Y, Z	Global system coordinate axis
x, y, z	Local system coordinate axis
$[M]$	Mass matrix
$[\tilde{M}]$	Effective mass matrix
$[C]$	Damping matrix
$[K]$	Stiffness matrix
$[T]$	Transformation matrix
$[T]^T$	Reversed-transformation matrix
$\{U\}$	Displacement vector
$\{\dot{U}\}$	Velocity vector
$\{\ddot{U}\}$	Accelerating vector
$\{F\}$	Force vector
$\{FF\}$	Effective force vector

Chapter 1 : INTRODUCTION

1.1 Recourses in Canada

Petroleum production in Canada is a major industry that plays an important role for the economy in North America. Canada is the sixth largest oil producing country in the world. In 2008 it produced an average of 438,000 cubic meters per day (2,750,000 bbl/d) of crude oil, bitumen and natural gas condensate. Of that amount, 45% was conventional crude oil, 49.5% was bitumen from oil sands, and 5.5% was condensate from natural gas wells (National Energy Board, 2009). Most of Canadian petroleum production, approximately 283,000 cubic meters per day (1,780,000 bbl/d), is exported, mostly from Alberta (National Energy Board of Canada, 2009).

Conventional oil and gas development is characterized by vertical wells with good recovery factors and large drainage areas. However, the productivity of conventional oil and gas wells has declined significantly in recent years since less and less oil and gas resources left in the reservoir as production goes by. The development of unconventional oil and gas is associated with advanced technologies, such as long-reach horizontal wellbores and hydraulic fracturing, as well as unique operating strategies based on different reservoir characteristics and engineering challenges.

Unconventional resources are a key part of the future of Alberta's energy resource sector as Alberta has significant unconventional resource potential. (Energy Resources Conservation Board, 2012). Just how large the resource potential could be is the focus of some current studies, for instance, Keith evaluated the Coal Bed Methane resource in Alberta (Keith, 2000).

The term unconventional describes a shift towards resources of larger potential with increased technical challenges to recover (see Figure 1.1). The term unconventional has typically been applied to oil- or gas-bearing zones with low to very poor permeability that require increased reservoir access and/or extensive stimulation for producing at commercial scale. Advanced drilling and completion technologies are required. Unconventional resource deposits cover broader areas than conventional oil and gas reservoirs due to the geological conditions at the time of deposition, which favored deposits of shale and other very fine grained rocks. Consequently, unconventional resources are not difficult to discover relative to conventional oil

and gas reservoirs; the challenge lies more in resolving technical issues, for example: advanced drilling and completion technologies, and maintaining the economic feasibility of the resource extraction.

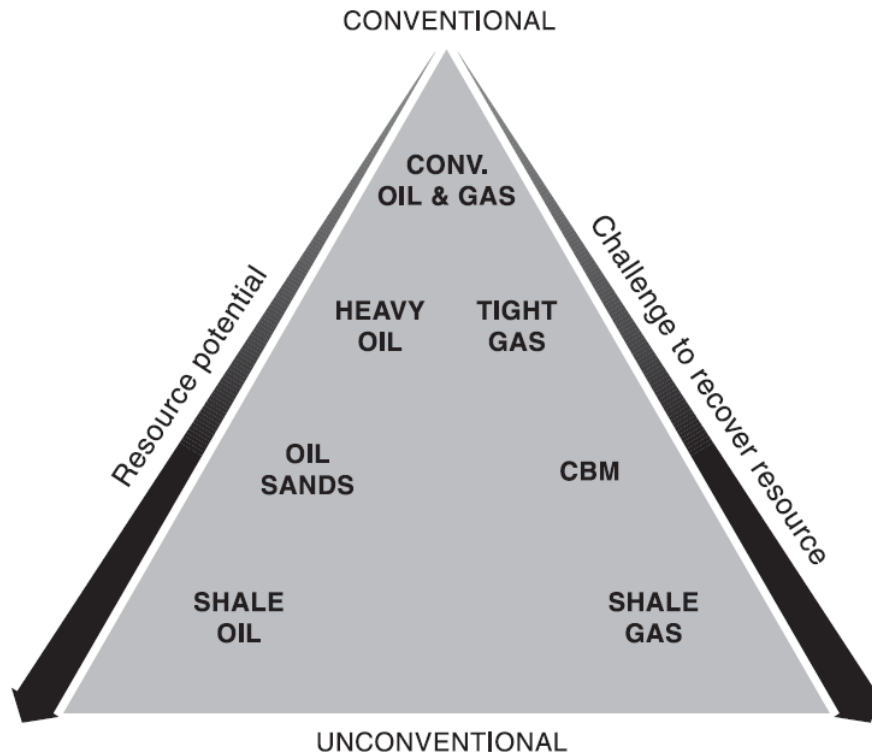


Figure 1.1 Conventional and Unconventional Resource Triangle (Stephen, 2013)

1.2 Drilling Technologies for Unconventional Reservoir

For many decades, the only way to access underground resources was by drilling vertical wells. However, in many instances, these (vertical wells) are not suitable, or not economical. For most cases, unconventional reservoirs don't have an economical producing thickness for vertical wells. Directional drilling (or slant drilling) is the practice of drilling non-vertical wells. It is the science of deviating a wellbore along a planned path to a target located a given lateral distance and direction from vertical. However, for directional wells and horizontal wells, the production area depends on the total length of the horizontal section passing through the reservoir. The benefits derived from drilling horizontal wells are not limited to just increase in the production area. The benefits are include (Joshi, 2003):

- Greater wellbore length exposure to the pay zone, resulting in increased production rate;
- Reduced pressure drop around the wellbore;
- Lower fluid velocities around the wellbore;
- Larger and more efficient drainage pattern leading to increased overall recovery;
- Reduced water and gas coning because of reduced drawdown in the reservoir for a given production rate, thereby reducing the remedial work required in the future.

Heavy crude oil and bitumen recovery in Alberta often involve, Steam Assisted Gravity Drainage (SAGD). SAGD is an advanced form of steam stimulation in which a pair of horizontal wells are drilled into the oil reservoir, a few meters above the other. High pressure steam is continuously injected into the upper wellbore to heat the oil and reduce its viscosity. The heated oil drains into the lower wellbore, where it is pumped out of the formation. In order to use this technology for heavy oil production, horizontal wells are necessary. Figure 2 is a brief illustration of the concept of SAGD technology.

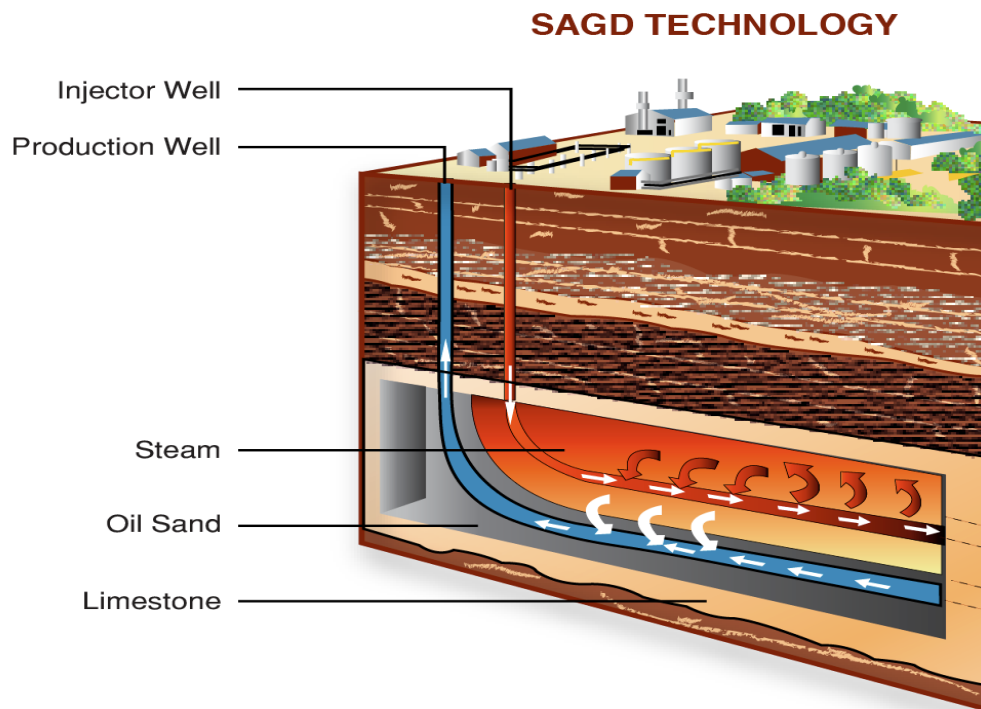


Figure 1.2 Brief Schematic of SAGD Technology (Surmont Energy, 2014)

1.3 Challenges for Directional Drilling

Horizontal drilling can bring great benefits for the oil and gas industry and are thus increasingly drilled in North America. However, there are some challenges when applying this technology in field operation. Two main challenge are the torque and drag issue and the weight on bit (WOB) transfer and control.

In field operations, WOB is a significant parameter for drilling optimization. Usually, for different formations that have different hardnesses, there is one optimal WOB to achieve best rate of penetration for a specific drilling bit. Therefore, precise control of WOB can greatly increase the overall rate of penetration, decrease operation time and reduce overall drilling cost. On the contrary, some problems will occur if the WOB isn't controlled precisely, for instance: if the WOB is much greater than the optimal value, the rate of penetration for some specific rock can decrease and accelerate bit wear, or the drillstring can buckle causing bit wobble or accelerate drillstring vibrations. If the WOB is smaller than the optimal value, it slows down the rate of penetration and best drilling performance is not obtained, which also means more time and money cost. Based on those reasons, WOB needs to be monitored.

In the field, WOB is shown on the surface panel during operation. It is obtained based on one simple equation:

$$\text{WOB} = \text{String Weight} - \text{Hookload}$$

It shows acceptable accuracy for vertical wells, but for horizontal wells, it cannot be used because of low accuracy due to wellbore friction.

For horizontal wells, the inclination for the entire well is 0°. For the buildup sections and horizontal sections of horizontal wells, the inclination is not equal to 0°. For buildup sections, the inclinations increase from 0° to 90° and in the horizontal sections the inclination equals or is close to 90°. Since there are inclination changes, the bottomhole assembly (BHA) and drillstring will contact the wellbore by gravity or due to buckling while rotating. Because of the existence of friction between drillstring and wellbore, torque and drag will occur and accumulate from bottom hole to surface. The additional drag will partially offset WOB believed to set at surface. This is

also the reason why the WOB on surface panel is inaccurate for horizontal wells. Generally, the WOB on surface is greater than the downhole WOB.

This has been an issue for a long time, but hasn't caused enough attention for drilling companies. Gazaniol conducted a study about the weight and torque transmission to the drill bit (Gazaniol, 1987). It shows good transmission in vertical wells, but bad transmission in horizontal wells.

1.4 Solutions for Challenges

In order to resolve this problem, some drilling service companies designed and developed some subs (downhole tools) dedicated for measuring real WOB. Two of these are: the CoPilot from Baker Hughes, and the Enhance Measurement System (EMS) from National Oilwell Varco (NOV). Real WOB is also called as downhole weight on bit (DWOB). Even though the subs can be used to measure DWOB accurately, they are relatively expensive. Driven by the potential for saving money by eliminating the cost of the subs, computer simulation could be a less expensive way to calculate the DWOB based on real-time drilling data.

For computer simulation, two models can be used. The first model is named: the torque and drag model, also known as the analytical model. The second model is named: the Finite Element Method (FEM). Each method has advantages and disadvantages, for the analytical model, the drillstring along the well path is simplified as a soft string without considering stiffness. The benefits of this assumption are: higher computing speed and acceptable accuracy for real-time calculation. For the FEM, stiffness of each drillstring element is considered, the advantages of considering stiffness are: the result will be more accurate and the vibration/shocking of drillstring can be analyzed. However, it takes around 2000 iterations until the results get convergent, so the calculations are more time-consuming. For the calculations, both methods use the same information from the field. This includes: survey data (bit depth, inclination and azimuth), BHA information (components, unit length weight, density as well as inside/outside diameters), mud density and hookload. When using both models after the friction factor is determined, the computer program will increase the "input DWOB" stepwise to calculate the "model hookload" until the "model hookload" equals to the measured hookload on surface panel. The calculation will then stop, and the "input DWOB" is the calculated DWOB. In the field operation, the driller

simply adjusts the hookload for a given calculated DWOB, then the DWOB is transferred to the bit. More details about both methods can be found in Chapter Three and Four, and simulation experiments section in Chapter Five.

1.5 Auto-Driller System

Acquiring the DWOB with computer simulation has another benefit: it can be used in a new Auto-Driller system for real-time monitoring.

An Auto-Driller is a system that can maximize rate of penetration by controlling DWOB. It is designed to reduce costs by reducing drilling time and extending the life of drill bits. By using an Auto-Driller System, drilling operations can be taken into an optimum level of accuracy and control. Through constant monitoring and adjustment, the system ensures that WOB is automatically maintained at a precise and consistent level. The driller will input the DWOB, then the system will calculate how much hookload is needed, then the system will change the hookload to the calculated value. As a result, it can maximize the overall rate of penetration and decreases the cost. Figure 1.3 explains how an Auto-driller system works.

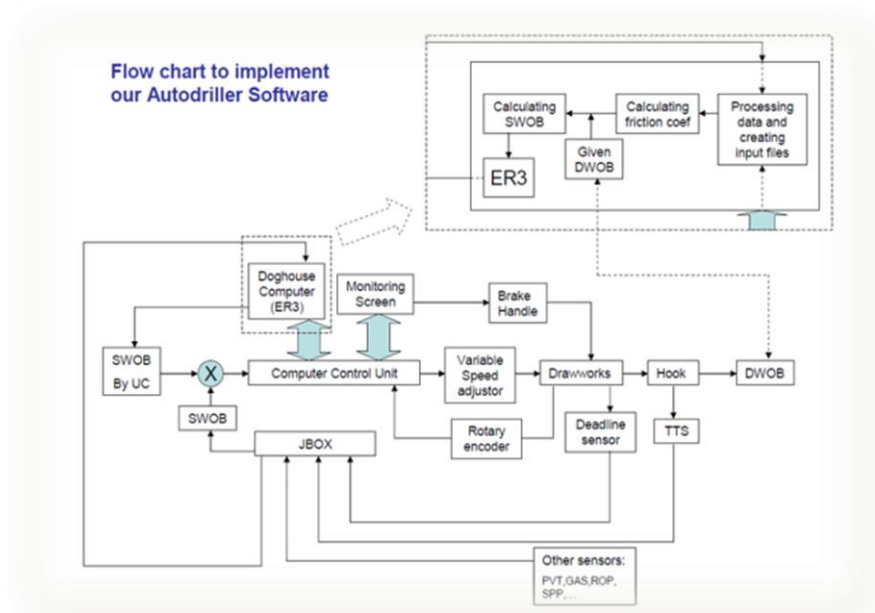


Figure 1.3 Flow chart of Auto-Driller System

The WOB showing on surface panel does not equal to the real DWOB, therefore, models need to be applied and the calculated DWOB can be input into the Auto-Driller system for real-time monitoring.

Chapter 2 : LITERATURE REVIEW

In this chapter, the most important research associated with torque and drag models will be introduced. The chapter is divided into two parts: the analytical model and the finite element method.

2.1 Analytical Model

In 1984, Johancsik et al. developed the first analytical model for torque and drag analysis (Johancsik, 1984). In this model, the entire drillstring is treated as a soft string without considering stiffness. It is assumed that both torque and drag are completely caused by sliding friction, which mainly depends on the normal force and the friction coefficient between the drillstring and wellbore. The friction force is mainly depends on the friction factor and the normal force. Numerous factors contribute to the normal force. Johancsik only considered two: the gravity of the drillstring and the buoyancy. Other factors such as the flowing hydraulics effect and the bit piston effect, are not considered. This model is simple to program, and has been widely used in the drilling field applications.

M.C. Sheppard conducted research on torque and drag, using mud pressure as an additional factor. Sheppard also derived the Johancsik model into a standard differential form (Sheppard, 1987). This research showed that an undersectional trajectory (a trajectory lying below the conventional tangent section and constantly building to target) can exhibit lower drag and torque than a conventional well geometry in certain circumstances.

Brett conducted field case study using the Johancsik model. For the case study, Brett developed a pre-planned well trajectory and used real-time drilling data to back-calculate the friction coefficient for monitoring the hole condition (Brett, 1989). Brett's research shows that extra torque and drag can be caused by the trajectory of the well path, as well as other factors (e.g. accumulating cuttings and hydraulics). Brett also used data from two drilled wells for post-analysis. By changing trajectories of both wells, a reduction of torque and drag was achieved and some drilling problems were explained by this model. Brett's research demonstrates the success of using a torque and drag model for well planning, monitoring drilling problems and normal post-analysis of wells, as opposed to spot applications limited to problem wells.

Researchers Aarrestad and Blikra addressed various aspects of torque and drag problems encountered in drilling extended-reach wells (Aarrestad, 1994). Their research explains how to use torque and drag calculations and measurements to plan long-reach well profiles, to execute drilling operations that minimize torque and drag effects, to monitor hole cleaning, to plan jarring and handle stuck casing and liners.

Aadnoy developed friction models for a number of different well geometry's (Aadnoy, 1998). Explicit equations were used to model both the rotary torque and drag forces associated with hoisting or lowering the drill string. More equations were developed for combined motion, drilling with a motor and to compute well friction for a fully 3-dimensional well. These equations may be applied to any type of well, using a spreadsheet. Figure 2.1 shows the friction model schematics.

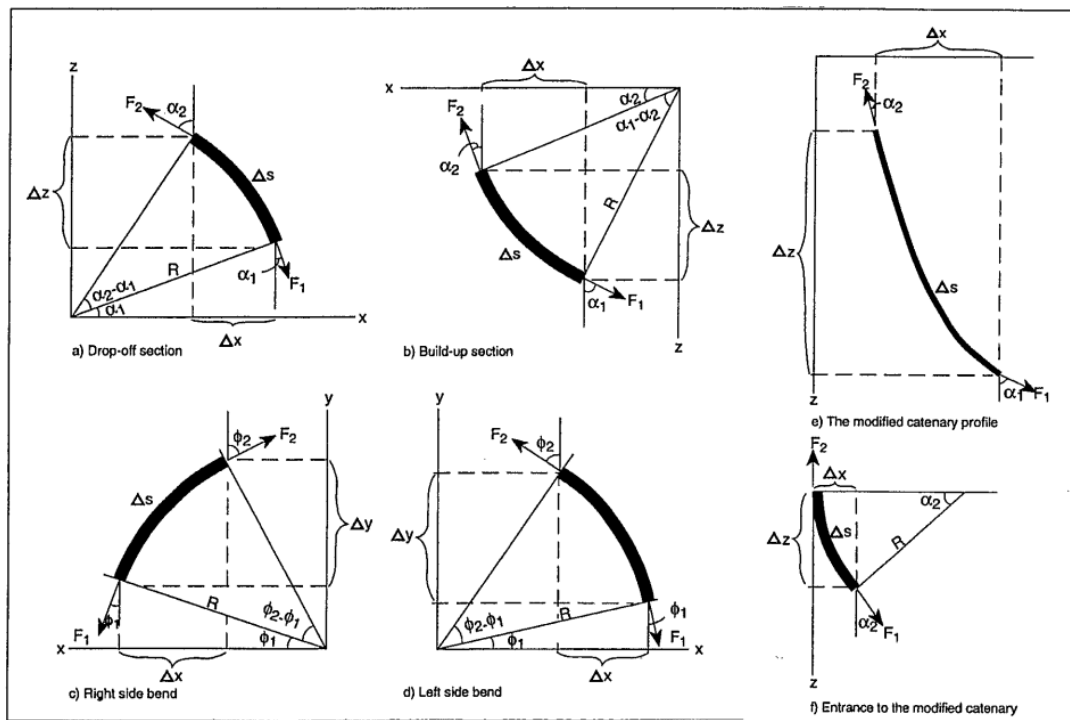


Figure 2.1 Forces and Geometries of Various Curved Hole (Aadnoy, 1998)

This model was also applied to real cases, showing that a proper well path design can reduce torque and drag.

Reiber presented a technique, for evaluating torque and drag effects in real time and interpreting the effectiveness of actions taken (Reiber, 1999). The system determines whole wellbore friction factor and incremental hole section friction factors, using real time downhole measured WOB and bit torque data coupled with surface load measurements (or just surface data without bit torque data), The system also determines buckling modes, minimum yield and fatigue safety factors, enabling field personnel to identify drilling performance problems as early as possible.

Aadnoy et al developed the mathematical models to design a catenary well pathm (Aadnoy, 2006). It shows that the catenary requires well defined forces and a build rate that changes with depth. It has the potential of providing minimum friction in the wellbore if correctly applied. The catenary can minimize friction for one operation only, for example for hoisting, lowering or rotation. They did a case study and verified the theoretical prediction.

Identifying that the symmetry in the torque and drag model solutions, Aadnoy et al. proposed a simplified torque and drag model (Aadnoy, 2008). It was shown that the force analysis for straight section is similar, the difference between these two models will only be the curved section part, as shown in Figure 2.2.

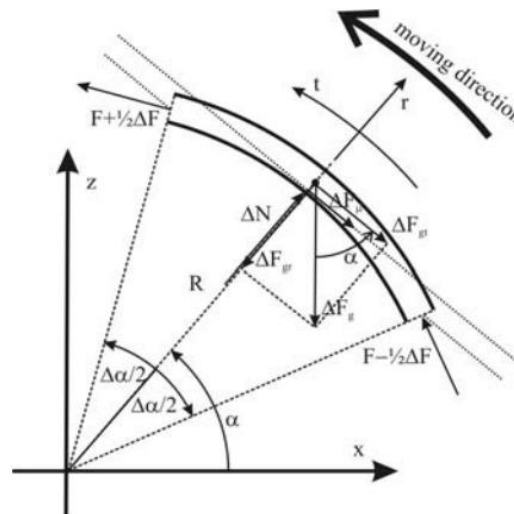


Figure 2.2 Forces and Geometries for Curved Section (Aadnoy, 2008)

The model only consists two equations: one for rotating friction (torque) and one for pulling friction (drag) that is valid for all well geometries. This new model covers vertical sections, build-

up bends, drop-off bends and straight sections. For all these geometries the new model is valid for tubulars both in tension and in compression.

Mitchell R.F. and Samuel R. evaluated the existing torque and drag models and summarized the basic defect of the model (Mitchell, 2009). Based on their evaluation, they concluded that the torque and drag model surprisingly cannot be a “soft string” model and still satisfy the equilibrium equations. Non-zero shear forces must exist, otherwise, friction loads will vanish. Fortunately, no changes to the formulation are necessary, and the shear forces can be evaluated with an easy calculation. An additional factor must be added to the contact force for torque calculations, because the rotating string will tend to “climb” the wellbore wall, reducing the contact force. The real weakness of the torque drag model is the use of constancy curvature wellbore trajectories. These trajectories imply that drillstring bending moment does not vary smoothly at survey points, which means that some contact forces and axial loads are missing from the model. Rough estimates of wellbore torsion and change of curvature with depth, when applied to the example cases, seem to identify wellbores that are not good candidates for torque drag modeling, but further study will be necessary.

After summarizing the established models, researchers Aadnoy established a new 3-D torque and drag model (Aadnoy, 2010). This model is simpler compared with the one they established in 2008. It applies to all wellbore shapes such as straight sections, drop-off bends, build-up bends, side bends or a combination of these. The drillstring is modeled as a soft string. In high tension the string weight is negligible as compared to the tension. This leads to simplified equations where the friction caused by the weight is negligible. In that case the friction in a bend is formulated in terms of the 3D dogleg. The same model therefore applies for 2D and 3D wellbores. The entire well can be modeled by two sets of equations: one for straight sections and another for curved sections. The latter is based on the absolute directional change or the dogleg of the wellbore. Then a case study is carried out, the results derived from this case study verified this new 3-D model.

2.2 FEM

Finite Element Method (FEM) is also known as Finite Element Analysis (FEA). The first application of FEM can be traced back to 1943 by researcher Courant. He used the Ritz Method of numerical analysis and minimization of variational calculus to obtain approximate solutions to vibration systems. Shortly thereafter, a paper published in 1956 by Tumer, Clough, Martin and Topp established a broader definition of numerical analysis. The paper centered on the “Stiffness and Deflection of Complex Structures”.

By the early 70's, FEM was limited to expensive mainframe computers generally owned by the aeronautics, automotive, defense, and nuclear industries. Since the rapid decline in the cost of computers and the increase in computing power, FEM has been developed to become a reliable precision.

FEM consists of a computer model of a material or design that is stressed and analyzed for specific results. It is used in new product design, and existing product refinement. A company is able to verify a proposed design and will be able to perform to the client's specifications prior to manufacturing or construction. Modifying an existing product or structure is utilized to qualify the product or structure for a new service condition. In case of structural failure, FEM may be used to help determine the design modifications to meet the new condition.

There are generally two types of analysis that are used in industry: 2-D modeling, and 3-D modeling. While 2-D modeling conserves simplicity and allows the analysis to be run on a typical desktop, it tends to yield less accurate results. 3-D modeling, however, produces more accurate results while sacrificing the ability to run on all but the fastest computers effectively. Within each of these modeling schemes, the programmer can insert numerous algorithms (functions) which may make the system behave linearly or non-linearly. Linear systems are far less complex and generally do not take into account plastic deformation. Non-linear systems do account for plastic deformation, and many also are capable of testing a material all the way to fracture.

FEM has been used in the Oil and Gas industry for decades using lumped analysis method. The essential idea of this method is that the entire drillstring is consist of many small 3D beam elements. Each element has twelve degrees of freedom (6 displacements and 6 rotations). In

1996, Dykstra stated that the only disadvantage of this method is that it is time-consuming when the element number is big (Dykstra,1996).

Millheim, Jordan and Ritter used finite-element method to analyze four bottom-hole assemblies (Millheim, 1978). One is a moderate building assembly, and the others range from a holding assembly with a slight dropping tendency to a stronger dropping assembly. Using this method, changes in geometry, loading, material properties and boundary conditions for BHAs can be considered. "BHA configurations" is shown in Figure 2.3.

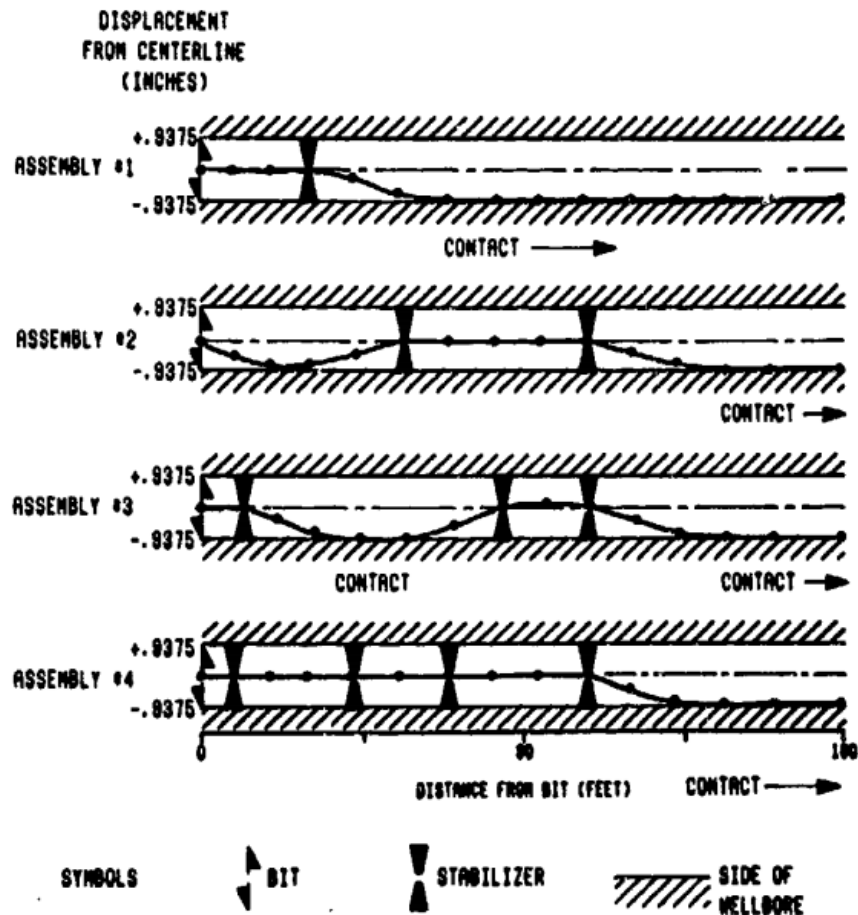


Figure 2.3 Bottom-hole Assembly Configurations (Millheim, 1978)

Bueno used finite element model with a non-linear, 2D, quasi-static approach to estimate the contact forces between the drillstring against the riser/ wellhead / wellbore (Bueno, 1994). In this research, the drillstring is modeled as elastic beams and the beams have a length equals to

the range of the drillpipe assuming that the contact points occurs only at the tool-joints, as shown in Figure 2.4.

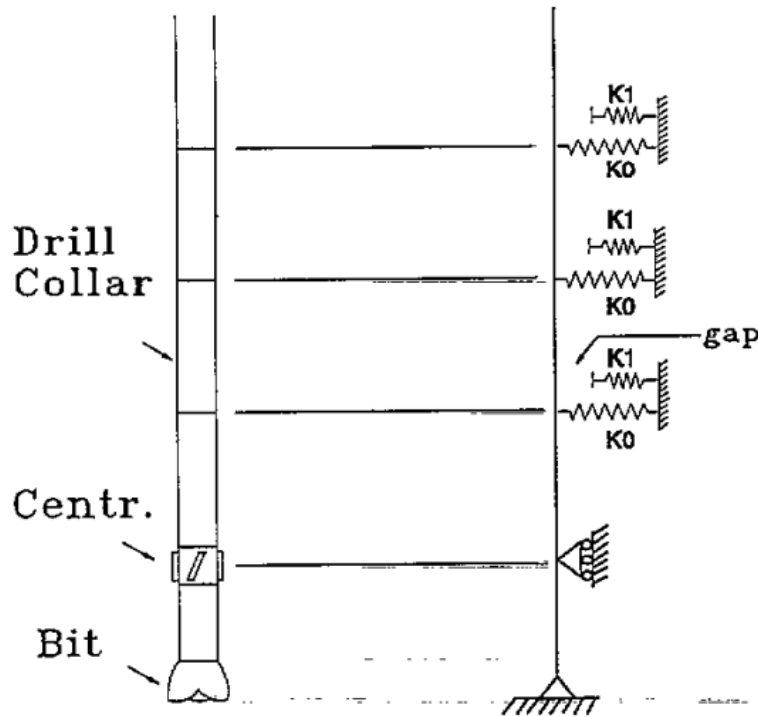


Figure 2.4 Bottom-hole Assembly Configurations (Bueno, 1994)

Newman et al. developed a dynamic FEM calculation engine, and it has been used to solve specialized well intervention problems (Newman, 2006). In his paper, two applications have been carried out: modeling the buckling behavior of pipe being snubbed through a packer, and wireline being run from a boat to a subsea well to perform an intervention.

Yang presented a three dimensional finite difference differential method for bottom hole assembly analysis under static loads (Yang, 2008). This analysis is required to optimize the BHA configurations for drilling directional boreholes. The optimization of BHA configurations ensures the controlled cruising of the drill bit to drill the hole along a planned trajectory. The model incorporates the contact response between drillstring and wellbore wall, the upper tangent point problem, stabilizer configurations, bent sub model and other considerations for numerical solutions.

Ishak used explicit finite element method to model the static and dynamic interactions between the bit, the reamer and the formation of the BHA while in the reaming operation (Ishak, 2012). The results indicate that the explicit FEM is an adequate solution technique for the boundary value problem describing the drillstring structure. Furthermore, the drill-ahead model enabled study of transient interaction between the reamer and the bit. Results also showed the transient history of the side and axial forces on the bit, reamer and stabilizers.

Chapter 3 : ANALYTICAL MODEL

There are many causes for excessive torque and drag, including: sliding friction, tight hole conditions, sloughing hole, keyseats, differential sticking and cuttings buildup caused by poor hole cleaning. These causes are associated with problem conditions in the wellbore. In wells with good hole conditions, sliding friction is the primary source of torque and drag. Therefore, only wells with good hole condition will be considered in this thesis.

In this chapter, a 3-D analytical model will be introduced for torque and drag analysis. A lumped-parameter model provides the basis for the prediction of torque and drag and both torque and drag are assumed to be caused completely by sliding friction forces that result from contact of the drillstring with wellbore. Therefore, other less important sources of torque and drag are not considered in the soft string model.

In this model, the drillstring is considered to be a heavy cable lying along the wellbore. It is also called a “Soft String Model” because the stiffness of the drillstring is not considered. Because the model excludes the stiffness effect, the drillstring will contact the wellbore due to its own gravity in the directional and horizontal sections, and the contact area will be the entire lower side of the drillstring.

The basic idea of this analytical model is to break down the whole drillstring into small elements. Each element has two sides, and the forces between both sides are 100% connected and transferred. See simplified schematic in Figure 3.1. The force is calculated starting at the first element at bottom, sequentially towards the last element at the surface.

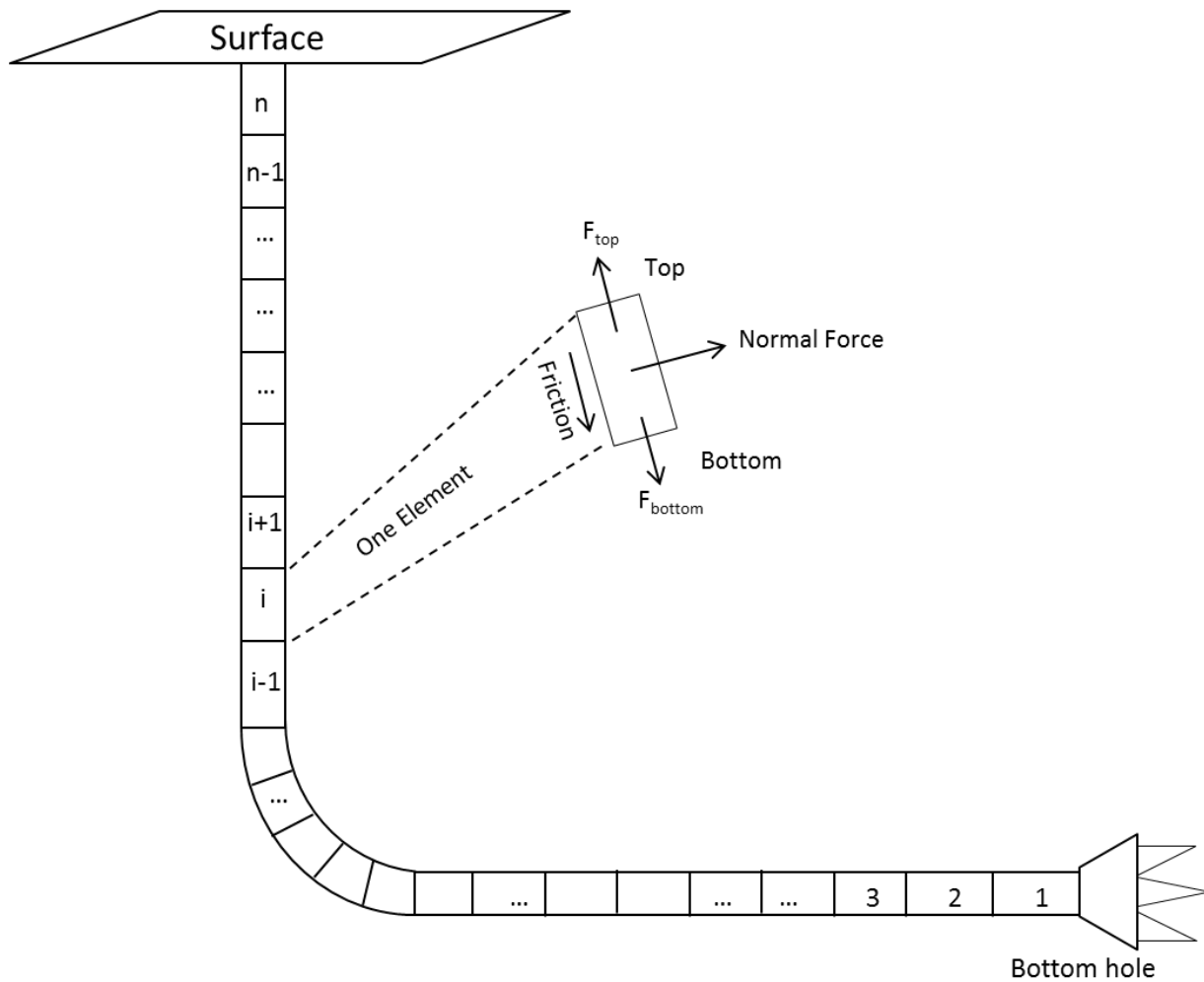


Figure 3.1 Schematic of 3-D Analytical Model

In Figure 3.1, we can assume the operation is tripping out, so the direction of the friction is towards bottom hole. As shown, the elements are not vertical. Because of an existing inclination angle in some of the elements, there will be a normal force on the contact face between the drillstring and wellbore, and a friction caused by tripping in/out. In this figure, forces involved in this model, for instance: gravity, buoyancy force, axial tension, friction force, perpendicular contact force.

3.1 Buoyancy Factor

Buoyancy force is a significant factor in the modeling torque and drag. Figure 3.2 shows the schematic of the buoyancy force. The effective drillstring weight is equal to unit pipe weight multiplied by the buoyancy factor.

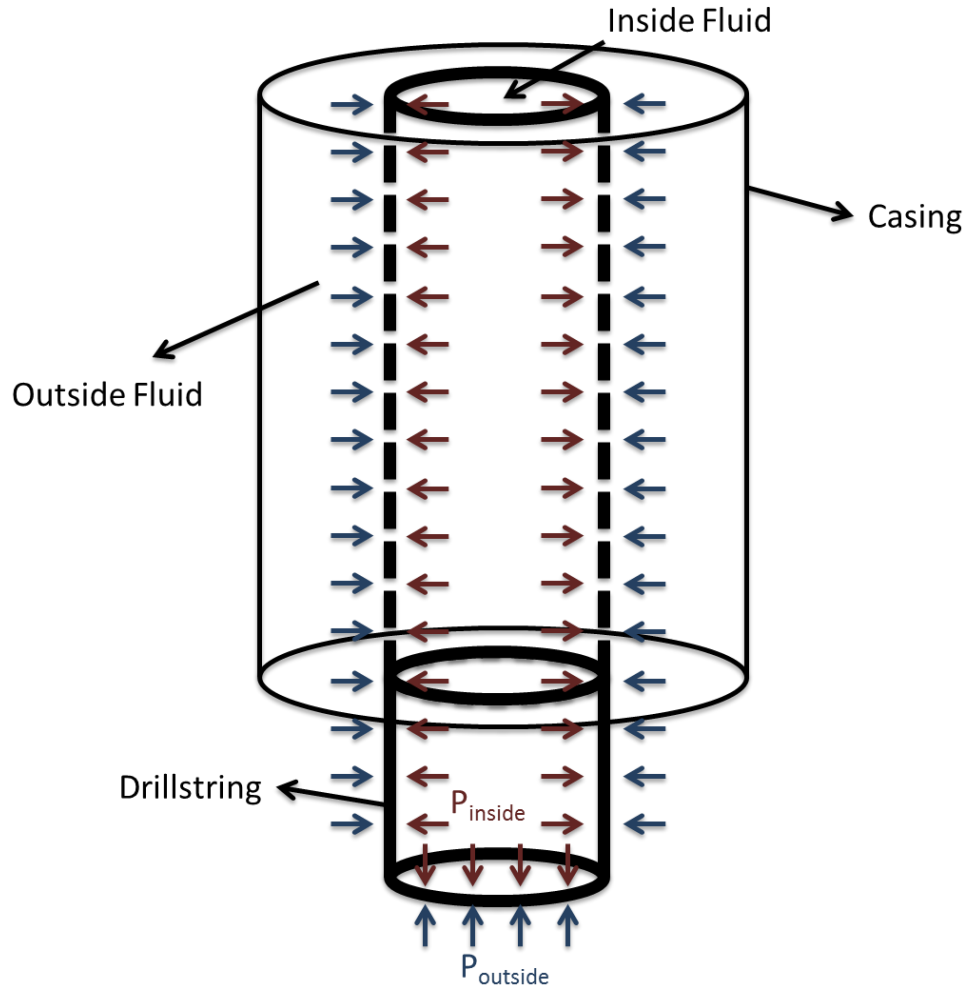


Figure 3.2 Schematic for Buoyancy Force

The buoyancy factor is defined as:

$$\beta = 1 - \frac{\rho_o A_o - \rho_i A_i}{\rho_{pipe} (A_o - A_i)} \quad (3.1)$$

Where:

β : Buoyancy factor

ρ : Length density of drillstring, kg/m³

A : Cross sectional area, m²

In this equation, the subscripts “o” and “i” refer to the outside and inside diameter of the drillstring respectively. If the density of the inside fluid equals the density of outside fluid, then the equation 3.1 can be written as:

$$\beta = 1 - \frac{\rho_o}{\rho_{pipe}} \quad (3.2)$$

Equation (3.2) is used most frequently in the field during operation, whereas (3.1) is used in cases when there is a density difference between the inside fluid and outside fluid. For operations like: cementing, well-killing, well control, connecting drillstring as well as underbalanced drilling operation.

With respect to the buoyancy factor, in this thesis, the situation meets the assumption of equation (3.2) (inside fluid and outside fluid are assumed to have same density). Therefore, we will use this equation to calculate buoyancy factor.

3.2 Straight Section

Two drillstring shapes are considered in this model: straight sections and curved sections. For straight sections, the inclination difference between the top of the element and the bottom of the element must be smaller than a criteria value. Conversely, the sections with inclination change greater than the criteria value will be regarded as curved sections.

The basic force analysis for straight sections is shown in Figure 3.3. Because tension and compression do not contribute to the normal force, they do not affect the friction.

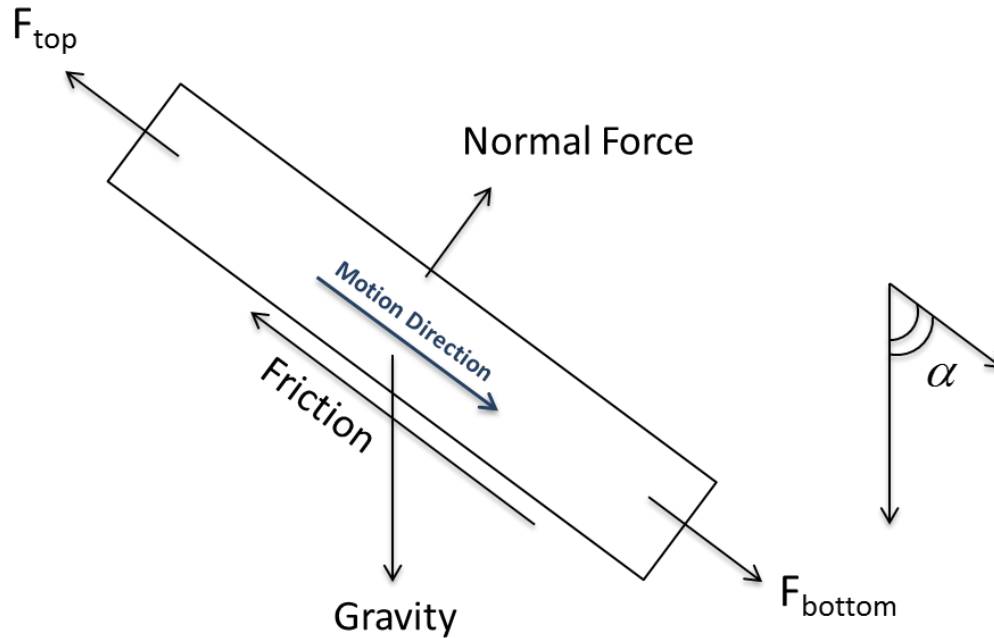


Figure 3.3 Force Analysis for Straight Section

Straight sections are weight-dominated sections, so according to force balance:

$$\text{Axial Force} = \text{Buoyancy} \times \text{Gravity} \times \cos \alpha$$

$$\begin{aligned} \text{Friction} &= \text{Friction Coefficient} \times \text{Normal Force} \\ &= \text{Buoyancy} \times \text{Gravity} \times \text{Friction Coefficient} \times \sin \alpha \end{aligned}$$

And these equations can be written as:

$$F_n = \beta \times \omega_i \times \Delta L_i \times \cos \alpha \quad (3.3)$$

$$F_{friction} = \mu \times \beta \times \omega_i \times \Delta L_i \times \cos \alpha \quad (3.4)$$

Combining the whole forces, we can get:

$$F_{top} = F_{bottom} + \beta \omega \Delta L \cos \alpha \mp \mu \beta \omega \Delta L \sin \alpha \quad (3.5)$$

+ means the operation is tripping out

- means the operation is tripping in

ΔL_i : length of each element, m

ω_i : unit length weight density, N/m

The same principle applies for rotation friction (the torque). The torque is defined as the friction coefficient multiplied by normal force and tool joint radius. Equation (3.6) calculates the torque loss along a straight section.

$$T_{top} = T_{bottom} + \mu \cdot \beta \cdot \omega \cdot \Delta L \cdot \sin \alpha \cdot r \quad (3.6)$$

3.3 Curved Section

Friction analysis for curved sections is shown in Figure 3.4. The direction of gravity is downward vertically, perpendicular to azimuth. The axial force caused by gravity has nothing to do with azimuth, but is associated with inclination.

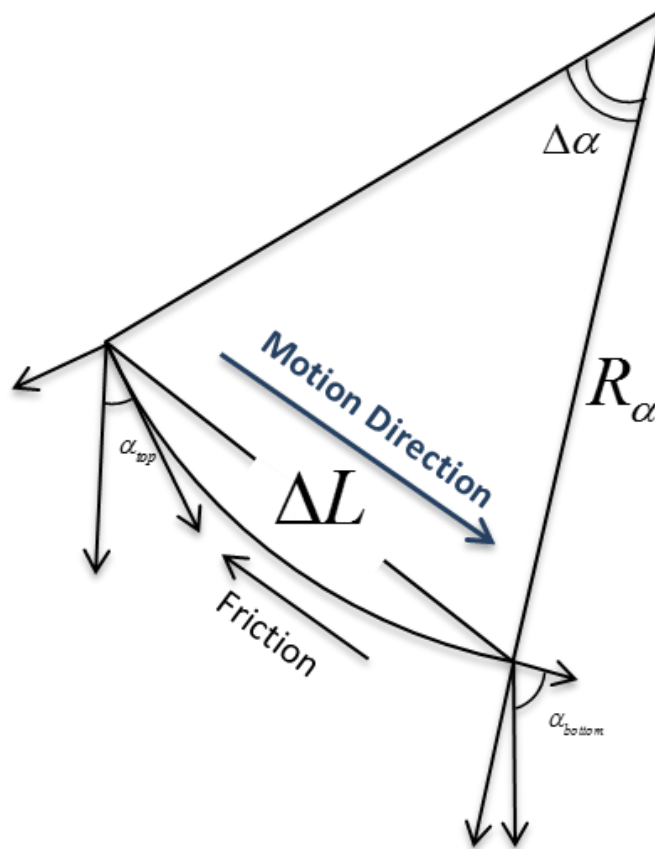


Figure 3.4 Friction Analysis (Part one) for Curved Section

Figure 3.4 shows Gravity-caused axial force and Gravity-caused friction force.

For Gravity-caused axial force:

$$\int_{\Delta L} \omega \cdot \beta \cdot \cos \alpha dL \quad \text{where, } dL = R_{\alpha} \cdot d\alpha$$

$$= \omega \cdot \beta \cdot \Delta L \cdot \left(\frac{\sin \alpha_{top} - \sin \alpha_{bottom}}{\alpha_{top} - \alpha_{bottom}} \right) \quad (3.7)$$

Likewise, for Gravity-caused friction force:

$$\int_{\Delta L} \mu \cdot \omega \cdot \beta \cdot \sin \alpha dL \quad \text{where, } dL = R_{\alpha} \cdot d\alpha$$

$$= -\mu \cdot \omega \cdot \beta \cdot \Delta L \cdot \left(\frac{\cos \alpha_{top} - \cos \alpha_{bottom}}{\alpha_{top} - \alpha_{bottom}} \right) \quad (3.8)$$

Equations (3.7) and (3.8) are the forces caused by gravity. Because the section is curved, the forces at the top and bottom are not applied in the same direction, so they have component forces that can cause an extra normal force, then the extra normal force will generate extra friction, which is a part of the total friction force.

Here, the directions of forces at both top and bottom of the element have intersection angles with both inclination and azimuth. Therefore, the friction here uniquely depends on the dogleg angle. Figure 3.5 shows the friction.

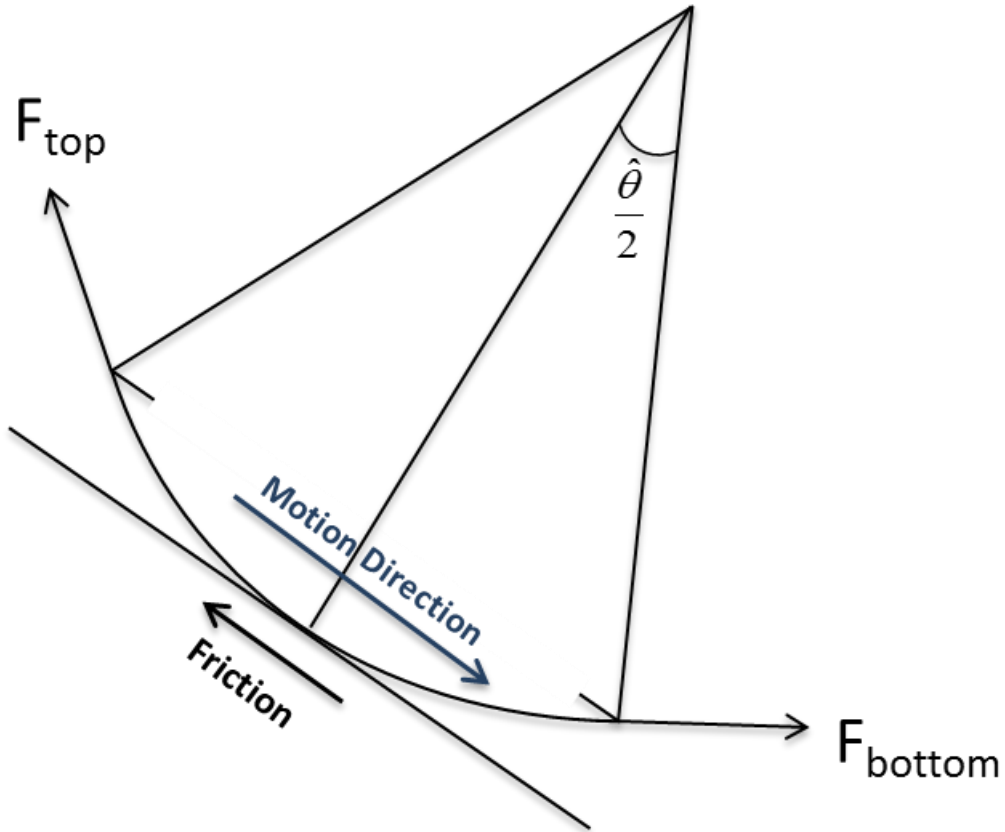


Figure 3.5 Friction Analysis (Part Two) for Curved Section

According to the schematic above, the normal force caused by both F_{top} and F_{bottom} is:

$$F_N = F_{top} \cdot \sin\left(\frac{d\theta}{2}\right) + F_{bottom} \cdot \sin\left(\frac{d\theta}{2}\right)$$

Where $d\theta \rightarrow 0$, which means: $\sin\left(\frac{d\theta}{2}\right) \rightarrow \frac{d\theta}{2}$, $F_{bottom} \approx F_{top}$,

Therefore, the equation can be written as:

$$F_N = F \cdot d\theta$$

And the drag loss is:

$$\Delta F = \mu \cdot F \cdot d\theta \text{ or it can be written as: } \frac{dF}{F} = \mu \cdot d\theta,$$

Integrating F and θ on the both sides of this equation ($\int_{\theta} = \int_{\theta_{bottom}}^{\theta_{top}}$):

$$\ln F_{top} - \ln F_{bottom} = \mu(\theta_{top} - \theta_{bottom}), \text{ where dogleg } \theta = \theta_{top} - \theta_{bottom},$$

Then the equation is:

$$F_{top} = F_{bottom} \cdot e^{\mp \mu |\theta|} \quad (3.9)$$

+ means the operation is tripping out

- means the operation is tripping in

Combining equations (3.7), (3.8) and (3.9) together, the relationship between F_{top} and F_{bottom} is:

$$F_{top} = F_{bottom} \cdot e^{\mp \mu |\theta|} + \omega \cdot \beta \cdot \Delta L \cdot \left(\frac{\sin \alpha_{top} - \sin \alpha_{bottom}}{\alpha_{top} - \alpha_{bottom}} \right) - \mu \cdot \omega \cdot \beta \cdot \Delta L \cdot \left(\frac{\cos \alpha_{top} - \cos \alpha_{bottom}}{\alpha_{top} - \alpha_{bottom}} \right) \quad (3.10)$$

Where dogleg θ is defined as:

$$\theta = \arccos \left(\sin \alpha_{top} \sin \alpha_{bottom} \cos (\phi_{top} - \phi_{bottom}) + \cos \alpha_{top} \cos \alpha_{bottom} \right) \quad (3.11)$$

In this curved section, based on the definition of Torque, the torque is derived with:

$$T_{top} = \mu r F_N + T_{bottom} = T_{bottom} + \mu r F_{bottom} |\theta| \quad (3.12)$$

Equation (3.10) is based on a tension dominated situation and can work only when both F_{top} and F_{bottom} are negative.

When the force is compression, we can use the Johancsik model (Johancsik, 1984). The schematic of this model is as shown in Figure 3.6.

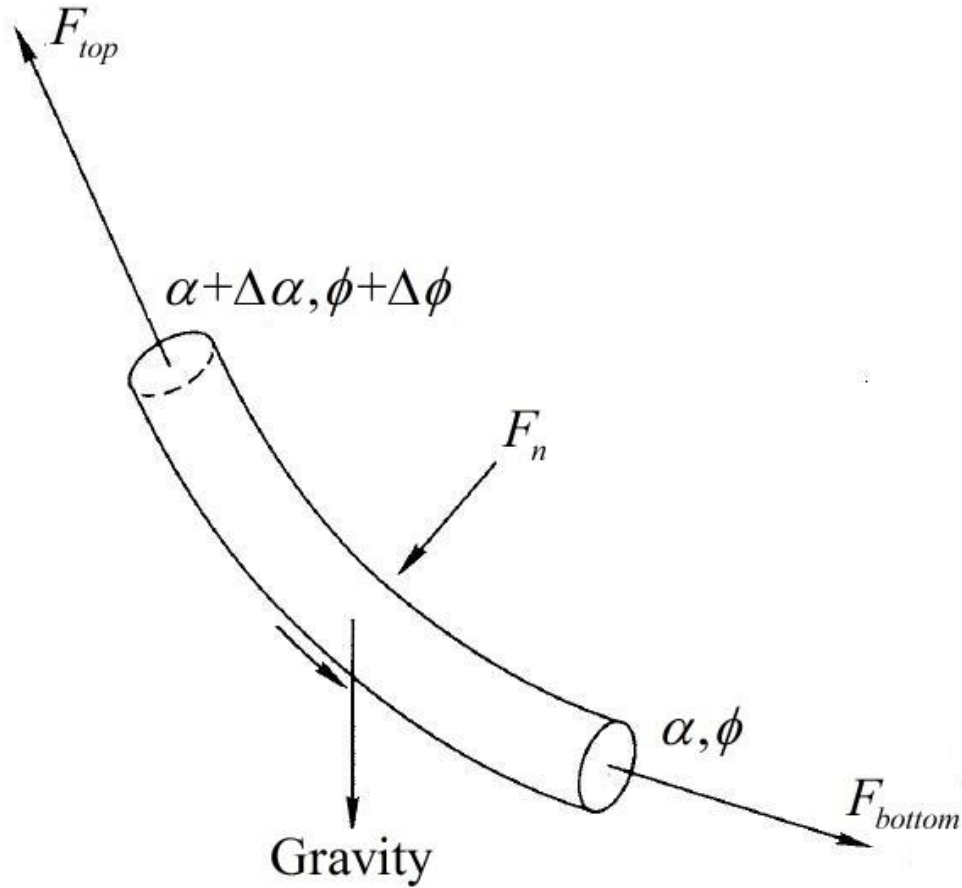


Figure 3.6 Johancsik Model for Compression Calculation (Johancsik, 1984)

The normal force is:

$$F_n = \left[(F_{bottom} \Delta\phi \sin \alpha)^2 + (F_{bottom} \Delta\alpha + \omega \Delta L \sin \alpha)^2 \right]^{1/2} \quad (3.13)$$

And the relationship between F_{top} and F_{bottom} is:

$$F_{top} = F_{bottom} + \omega \Delta L \cos \alpha \mp \mu F_n \quad (3.14)$$

And the torque can be calculated with the equation (3.15):

$$T_{top} = T_{bottom} + \mu r F_n \quad (3.15)$$

3.4 Combined Axial Motion and Rotation

From equations (3.3) to (3.15), we assumed there is no rotation while tripping in and tripping out.

Therefore, the equations in both section 3.2 and section 3.3 must be modified if a combined motion is to be considered. Aadnoy and Andersen showed how the frictional capacity is decomposed into two directions; axial motion and rotation (Aadnoy 2001). The effect of combined motion is commonly used in the field, when rotating a liner for easier running into the hole. A high rotational speed reduces axial drag considerably. During tripping operations, an over-pull may occur due to tight hole conditions. The remedy action is typically to rotate the drill string while pulling or lowering. The considerable difference can be observed between measured hook loads while tripping in/out and the reaming/back reaming operation.

Figure 3.7 shows a drillstring element with a weight of $w\Delta L$. If it is sliding, the drag will be equal to the normal force multiplied by the coefficient of friction, which is $\mu w\Delta L$. If the pipe is rotating instead, the torque ratio, T/r is also equal to $\mu w\Delta L$. Thus, the weight and friction coefficient results in the same frictional resistance regardless of whether the movement is axial or rotational.

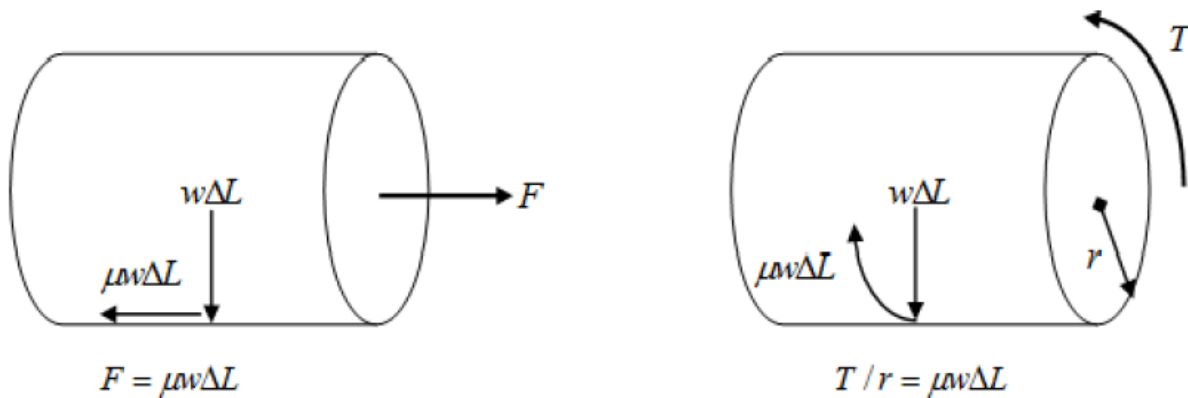


Figure 3.7 Drag and Torque for a Drillstring Element

During combined motion, the axial velocity is V_h , and the tangential pipe speed is V_r . There is a relationship between the two velocities, which is defined in Figure 3.8.

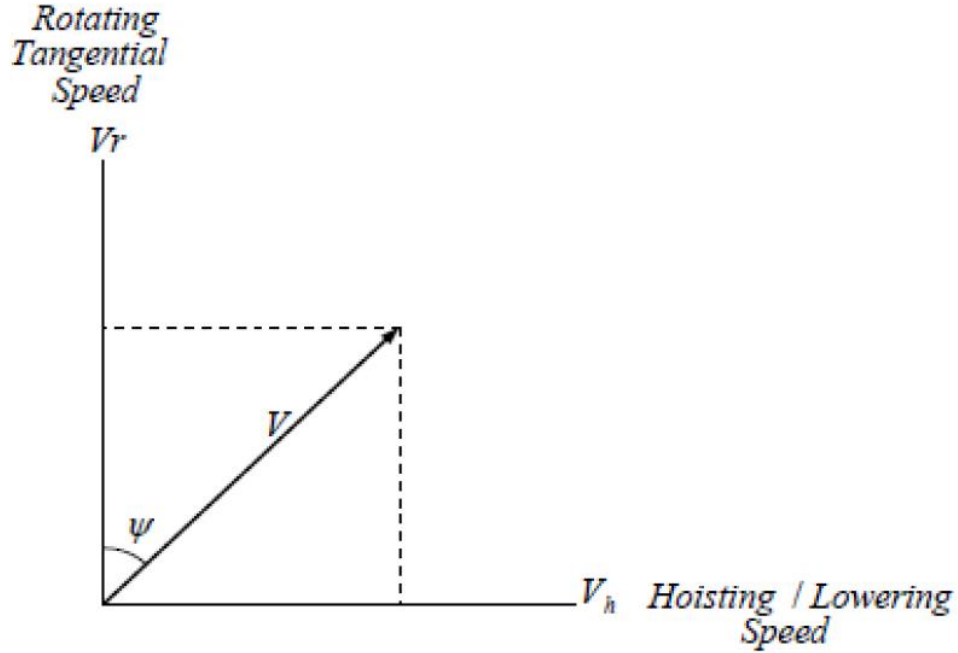


Figure 3.8 Relationship between Hoisting/Lowering and Rotational Speed (Fazaelizadeh, 2010)

The angle between the two velocities is defined as follow:

$$\psi = \tan^{-1} \left(\frac{V_h}{V_r} \right) = \tan^{-1} \left(\frac{60 \cdot V_h}{2\pi N_r \cdot r} \right) \quad (3.16)$$

When the new factor is integrated, the equations in section 3.2 and 3.3 are modified as:

For a straight Section:

$$F_{top} = F_{bottom} + \beta\omega\Delta L \cos \alpha \mp (\mu\beta\omega\Delta L \sin \alpha) \cdot \sin \psi \quad (3.17)$$

$$T_{top} = T_{bottom} + (\mu r \beta \omega \Delta L \sin \alpha) \cdot \cos \psi \quad (3.18)$$

For a curved Section:

The tension part:

$$F_{top} = F_{bottom} \left(e^{\mp \mu |\theta|} - 1 \right) \sin \psi + \omega \beta \Delta L \left(\frac{\sin \alpha_{top} - \sin \alpha_{bottom}}{\alpha_{top} - \alpha_{bottom}} \right) - \mu \omega \beta \Delta L \left(\frac{\cos \alpha_{top} - \cos \alpha_{bottom}}{\alpha_{top} - \alpha_{bottom}} \right) \quad (3.19)$$

$$T_{top} = T_{bottom} + \mu r F_{bottom} |\theta| \cos \psi \quad (3.20)$$

The compression part:

$$F_{top} = F_{bottom} + \omega\Delta L \cos \theta \mp \mu \left[(F_{bottom} \Delta \alpha \sin \theta)^2 + (F_{bottom} \Delta \theta + \omega\Delta L \sin \theta)^2 \right]^{1/2} \cdot \sin \psi \quad (3.21)$$

$$T_{top} = T_{bottom} + \mu r \left[(F_{bottom} \Delta \alpha \sin \theta)^2 + (F_{bottom} \Delta \theta + \omega\Delta L \sin \theta)^2 \right]^{1/2} \cdot \cos \psi \quad (3.22)$$

Equations from (3.17) to (3.22) are the main equations for analytical analysis.

3.5 Other Factors

The hookload measured by the gauge can on surface be greater than the hookload calculated in our model because other factors that could have an effect on the hookload. Therefore, the surface hookload must be calculated considering additional factors: Sheave effect, static hook weight effect and standpipe pressure effect.

The equations that were used for adjusting the surface hookload are:

Sheave effect:

$$HL_{a1} = \frac{HL_f \times (1 - \eta^n)}{n \times (1 - \eta)} \quad (3.23)$$

Static hook effect:

$$HL_{a2} = \frac{HL_s \times (1 - \eta^n)}{n \times (1 - \eta)} \quad (3.24)$$

Standpipe pressure effect:

$$HL_{a3} = 5.095 \times 10^{-5} \times spp \times id^2 \quad (3.25)$$

The final adjusted hookload can be expressed as follows:

$$HL_a = HL_{a1} - HL_{a2} - \chi HL_{a3} \quad (3.26)$$

Chapter 4 : FINITE ELEMENT METHOD

Chapter 3 introduced the Analytical Model, which has beneficial features for use in real-time drilling analysis: it is relatively easy to understand, relatively easy to program in Excel with a Macro Programming Function, and it offers quick calculation speed. However, the assumption of a soft string model makes it ineligible for more complicated wells, involving drillstring transformation. In order to resolve problem in more complicated situations, Finite Element Method (FEM) model is introduced here. With FEM model, stiffness of drillstring is taken into consideration.

4.1 Hamilton's Principle

Hamilton's Principle is William Rowan Hamilton's formulation of stationary action (Hamilton, 1834). It states that the dynamics of a physical system is determined by a variational problem for a functional based on a single function, the Lagrangian, which contains all physical information concerning the system and the forces acting on it. It states the motion of a particle (or system of particles, or a continuous system) is such that the kinetic and potential energies of the particle and the work done by forces. Based on the Hamilton's principle, we can derive the elasticdynamic equation for one 3D beam with deformable body as shown in equation (4.1).

$$\delta \int_{\Delta t} (T - V) + \int_{\Delta t} \delta W = 0 \quad (4.1)$$

In this expression, T is the kinetic energy that has components due to velocities of translation and rotation, V is the potential energy (or strain energy), defined in terms of stress σ_{ij} and strain ε_{ij} (where $i=1,3$), W is the work done by forces including gravity, unbalanced mass, and viscous drag (Dykstra, 1996).

4.2 3-D Beam Element

The basic idea of the Finite Element Method is to use finite discrete elements to represent a continuous objective, and to provide a numerical solution for a complicated massive integrity. In this paper, a 3-Dimensional beam element is chosen because:

- 1) The drilling pipes are in cylinder shape;

- 2) Considering the computing speed, smaller size of elements will make FEM more time-consuming which is not applicable in field. The beam element is small enough for computing but also accurate enough for field application.

There are two nodes at each end of every beam element. Each node has 6 degrees of freedom (DOF), including: three displacements on x,y,z coordinates, and three rotations around x,y,z coordinates. Figure 4.1 shows the 3D elements and two nodes, with six DOF.

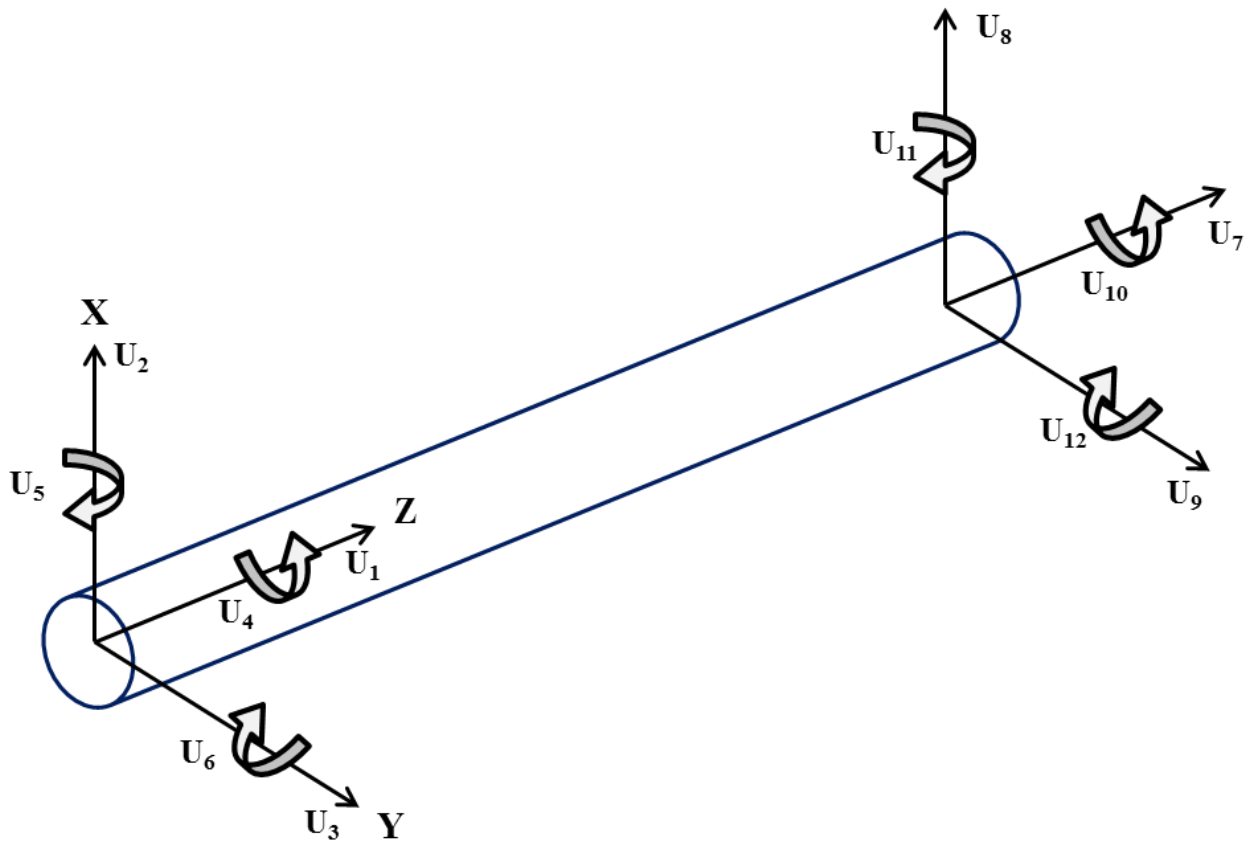


Figure 4.1 Displacements and Rotations for Each Beam Element

Figure 4.1 shows two transverse displacements (U_2 U_3 or U_8 U_9), one axial displacement (U_1 or U_7), two bending rotation (U_5 U_6 or U_{11} U_{12}) and one torsional rotation (U_4 or U_{10}) on each node.

4.3 Discrete System

Based on Hamilton's Principle, the discretized form of equation (4.1), after a series of mathematical manipulation, extended Hamilton's principle can be written as equation (4.2).

$$[M]^e \{\ddot{U}\}^e + [C]^e \{\dot{U}\}^e + [K]^e \{U\}^e = \{F\}^e \quad (4.2)$$

The vectors $\{U\}^e$, $\{\dot{U}\}^e$, $\{\ddot{U}\}^e$ and $\{F\}^e$ represent generalized displacement, velocity, acceleration and force vectors in local coordinate system respectively, each vector has 12 DOF as shown in equations (4.3) (4.4) (4.5) and (4.6). And the matrices $[M]^e$, $[C]^e$ and $[K]^e$ represent element mass, damping and stiffness matrix respectively. If matrices $[M]^e$, $[C]^e$ and $[K]^e$ remain unchanged at each time step, equation (4.2) will be linear. But since the truth is the deformation is not linear, some of the matrices are not linear that vary with time. Details are provided later in this chapter.

$$\{U\}^e = \{U_1 \ U_2 \ U_3 \ U_4 \ U_5 \ U_6 \ U_7 \ U_8 \ U_9 \ U_{10} \ U_{11} \ U_{12}\}^T \quad (4.3)$$

$$\{\dot{U}\}^e = \{\dot{U}_1 \ \dot{U}_2 \ \dot{U}_3 \ \dot{U}_4 \ \dot{U}_5 \ \dot{U}_6 \ \dot{U}_7 \ \dot{U}_8 \ \dot{U}_9 \ \dot{U}_{10} \ \dot{U}_{11} \ \dot{U}_{12}\}^T \quad (4.4)$$

$$\{\ddot{U}\}^e = \{\ddot{U}_1 \ \ddot{U}_2 \ \ddot{U}_3 \ \ddot{U}_4 \ \ddot{U}_5 \ \ddot{U}_6 \ \ddot{U}_7 \ \ddot{U}_8 \ \ddot{U}_9 \ \ddot{U}_{10} \ \ddot{U}_{11} \ \ddot{U}_{12}\}^T \quad (4.5)$$

$$\{F\}^e = \{F_1 \ F_2 \ F_3 \ F_4 \ F_5 \ F_6 \ F_7 \ F_8 \ F_9 \ F_{10} \ F_{11} \ F_{12}\}^T \quad (4.6)$$

In equations (4.3) (4.4) (4.5) and (4.6), those 12 DOF represent generalized displacements, velocity, acceleration and forces respectively. For instance, in vector $\{U\}^e$, displacements and rotations are all regarded as generalized displacements.

4.4 The Mass Matrix

Mass matrix is related to the concept of center of mass. Generally, lumped mass assumes that all mass is concentrated at the center of one rigid object. This means only the center of the object has mass while other parts of the object are massless. To achieve a more accurate analysis, we must equally distribute the mass to different parts of the object (Reddy, 1984 and Lalanne, 1998).

This equation has been expressed for a 3D beam element in equation (4.2). The mass matrix $[M]^e$ consists of two components: $[M_1]^e$, which represents all three translational contributions and axial rotation, and $[M_2]^e$, which indicates contributions from the third and fourth rotation components and thus provides a correction for rotatory inertia.

$$[M]^e = [M_1]^e + [M_2]^e \quad (4.7)$$

$$[M_1]^e = \rho AL \begin{bmatrix} \frac{1}{3} & 0 & 0 & 0 & 0 & 0 & \frac{1}{6} & 0 & 0 & 0 & 0 & 0 \\ 0 & \frac{13}{35} & 0 & 0 & 0 & \frac{11L}{210} & 0 & \frac{9}{70} & 0 & 0 & 0 & \frac{13L}{420} \\ 0 & 0 & \frac{13}{35} & 0 & \frac{11L}{210} & 0 & 0 & 0 & \frac{9}{70} & 0 & \frac{13L}{420} & 0 \\ 0 & 0 & 0 & \frac{I_x}{3A} & 0 & 0 & 0 & 0 & 0 & \frac{I_x}{6A} & 0 & 0 \\ 0 & 0 & \frac{11L}{210} & 0 & \frac{L^2}{105} & 0 & 0 & 0 & \frac{13L}{420} & 0 & \frac{L^2}{140} & 0 \\ 0 & \frac{11L}{210} & 0 & 0 & 0 & \frac{L^2}{105} & 0 & \frac{13L}{420} & 0 & 0 & 0 & \frac{L^2}{140} \\ \frac{1}{6} & 0 & 0 & 0 & 0 & 0 & \frac{1}{3} & 0 & 0 & 0 & 0 & 0 \\ 0 & \frac{9}{70} & 0 & 0 & 0 & \frac{13L}{420} & 0 & \frac{13}{35} & 0 & 0 & 0 & \frac{11L}{210} \\ 0 & 0 & \frac{9}{70} & 0 & \frac{13L}{420} & 0 & 0 & 0 & \frac{13}{35} & 0 & \frac{11L}{210} & 0 \\ 0 & 0 & 0 & \frac{I_x}{6A} & 0 & 0 & 0 & 0 & 0 & \frac{I_x}{3A} & 0 & 0 \\ 0 & 0 & \frac{13L}{420} & 0 & \frac{L^2}{140} & 0 & 0 & 0 & \frac{11L}{210} & 0 & \frac{L^2}{105} & 0 \\ 0 & \frac{13L}{420} & 0 & 0 & 0 & \frac{L^2}{140} & 0 & \frac{11L}{210} & 0 & 0 & 0 & \frac{L^2}{105} \end{bmatrix} \quad (4.8)$$

And,

$$[M_2]^e = \rho \frac{I_{xy}}{L} \begin{bmatrix} 0 & 0 & 0 & 0 & 0 & 0 & 0 & 0 & 0 & 0 & 0 & 0 \\ 0 & \frac{6}{5} & 0 & 0 & 0 & \frac{L}{10} & 0 & \frac{6}{5} & 0 & 0 & 0 & \frac{L}{10} \\ 0 & 0 & \frac{6}{5} & 0 & \frac{L}{10} & 0 & 0 & 0 & \frac{6}{5} & 0 & \frac{L}{10} & 0 \\ 0 & 0 & 0 & 0 & 0 & 0 & 0 & 0 & 0 & 0 & 0 & 0 \\ 0 & 0 & \frac{L}{10} & 0 & \frac{2L^2}{15} & 0 & 0 & 0 & \frac{L}{10} & 0 & \frac{L^2}{30} & 0 \\ 0 & \frac{L}{10} & 0 & 0 & 0 & \frac{2L^2}{15} & 0 & \frac{L}{10} & 0 & 0 & 0 & \frac{L^2}{30} \\ 0 & 0 & 0 & 0 & 0 & 0 & 0 & 0 & 0 & 0 & 0 & 0 \\ 0 & \frac{6}{5} & 0 & 0 & 0 & \frac{L}{10} & 0 & \frac{6}{5} & 0 & 0 & 0 & \frac{L}{10} \\ 0 & 0 & \frac{6}{5} & 0 & \frac{L}{10} & 0 & 0 & 0 & \frac{6}{5} & 0 & \frac{L}{10} & 0 \\ 0 & 0 & 0 & 0 & 0 & 0 & 0 & 0 & 0 & 0 & 0 & 0 \\ 0 & 0 & \frac{L}{10} & 0 & \frac{L^2}{30} & 0 & 0 & 0 & \frac{L}{10} & 0 & \frac{2L^2}{15} & 0 \\ 0 & \frac{L}{10} & 0 & 0 & 0 & \frac{L^2}{30} & 0 & \frac{L}{10} & 0 & 0 & 0 & \frac{2L^2}{15} \end{bmatrix} \quad (4.9)$$

4.5 The Stiffness Matrix

In the finite element method for the numerical solution of elliptic partial differential equations, the stiffness matrix represents the system of linear equations that must be solved in order to achieve an approximate solution to the differential equation. Usually, it defines the geometric and material properties of the element in the system. Stiffness matrices are a fundamental part of FEM. These matrices always define inherent properties of the system being studied.

In this model, the stiffness matrix $[K]$ comprises two parts: $[K_L]$ which indicates the linear stiffness components, resulting from strain energy; and $[K_N]$ which indicates the non-linear stiffness, caused by some terms in the strain-displacement relation.

$$[K]^e = [K_L]^e + [K_N]^e \quad (4.10)$$

$$\begin{aligned}
[K_L]^e = \rho \frac{I_{xy}}{L} & \left[\begin{array}{cccccccccccc}
\frac{EA}{L} & 0 & 0 & 0 & 0 & 0 & \frac{-EA}{L} & 0 & 0 & 0 & 0 & 0 \\
0 & \frac{12EI_{xy}}{L^3} & 0 & 0 & 0 & \frac{6EI_{xy}}{L^2} & 0 & \frac{-12EI_{xy}}{L^3} & 0 & 0 & 0 & \frac{6EI_{xy}}{L^2} \\
0 & 0 & \frac{12EI_{xy}}{L^3} & 0 & \frac{-6EI_{xy}}{L^2} & 0 & 0 & 0 & \frac{-12EI_{xy}}{L^3} & 0 & \frac{-6EI_{xy}}{L^2} & 0 \\
0 & 0 & 0 & \frac{GI_z}{L} & 0 & 0 & 0 & 0 & 0 & \frac{-GI_z}{L} & 0 & 0 \\
0 & 0 & \frac{-6EI_{xy}}{L^2} & 0 & \frac{4EI_{xy}}{L} & 0 & 0 & 0 & \frac{6EI_{xy}}{L^2} & 0 & \frac{2EI_{xy}}{L} & 0 \\
0 & \frac{6EI_{xy}}{L^2} & 0 & 0 & 0 & \frac{4EI_{xy}}{L} & 0 & \frac{-6EI_{xy}}{L^2} & 0 & 0 & 0 & \frac{2EI_{xy}}{L} \\
\frac{-EA}{L} & 0 & 0 & 0 & 0 & 0 & \frac{EA}{L} & 0 & 0 & 0 & 0 & 0 \\
0 & \frac{-12EI_{xy}}{L^3} & 0 & 0 & 0 & \frac{-6EI_{xy}}{L^2} & 0 & \frac{12EI_{xy}}{L^3} & 0 & 0 & 0 & \frac{-6EI_{xy}}{L^2} \\
0 & 0 & \frac{-12EI_{xy}}{L^3} & 0 & \frac{6EI_{xy}}{L^2} & 0 & 0 & 0 & \frac{12EI_{xy}}{L^3} & 0 & \frac{6EI_{xy}}{L^2} & 0 \\
0 & 0 & 0 & \frac{GI_z}{L} & 0 & 0 & 0 & 0 & 0 & \frac{GI_z}{L} & 0 & 0 \\
0 & 0 & \frac{-6EI_{xy}}{L^2} & 0 & \frac{2EI_{xy}}{L} & 0 & 0 & 0 & \frac{6EI_{xy}}{L^2} & 0 & \frac{4EI_{xy}}{L} & 0 \\
0 & \frac{6EI_{xy}}{L^2} & 0 & 0 & 0 & \frac{2EI_{xy}}{L} & 0 & \frac{-6EI_{xy}}{L^2} & 0 & 0 & 0 & \frac{4EI_{xy}}{L}
\end{array} \right] \quad (4.11)
\end{aligned}$$

$[K_N]^e$, it includes three parts: $[K_{NA1}]^e$ $[K_{NA2}]^e$, which represent coupling between axial force and flexure from different terms of strain energy respectively. In equations (4.13) and (4.14), both matrixes vary with time as the changes of U_1 and U_7 for every time step.

$$[K_N]^e = [K_{NA1}]^e + [K_{NA2}]^e + [K_{NT}]^e \quad (4.12)$$

$$\left[K_{NA_1} \right]^e = \frac{EA(U_7 - U_1)}{L^2} \begin{bmatrix} \frac{3}{2} & 0 & 0 & 0 & 0 & 0 & \frac{-3}{2} & 0 & 0 & 0 & 0 & 0 \\ 0 & \frac{6}{5} & 0 & 0 & 0 & \frac{L}{10} & 0 & \frac{-6}{5} & 0 & 0 & 0 & \frac{L}{10} \\ 0 & 0 & \frac{6}{5} & 0 & \frac{-L}{10} & 0 & 0 & 0 & \frac{-6}{5} & 0 & \frac{-L}{10} & 0 \\ 0 & 0 & 0 & \frac{I_z}{A} & 0 & 0 & 0 & 0 & 0 & \frac{-I_z}{A} & 0 & 0 \\ 0 & 0 & \frac{-L}{10} & 0 & \frac{2L^2}{15} & 0 & 0 & 0 & \frac{L}{10} & 0 & \frac{-L^2}{30} & 0 \\ 0 & \frac{L}{10} & 0 & 0 & 0 & \frac{2L^2}{15} & 0 & \frac{-L}{10} & 0 & 0 & 0 & \frac{-L^2}{30} \\ \frac{-3}{2} & 0 & 0 & 0 & 0 & 0 & \frac{3}{2} & 0 & 0 & 0 & 0 & 0 \\ 0 & \frac{-6}{5} & 0 & 0 & 0 & \frac{-L}{10} & 0 & \frac{6}{5} & 0 & 0 & 0 & \frac{-L}{10} \\ 0 & 0 & \frac{-6}{5} & 0 & \frac{L}{10} & 0 & 0 & 0 & \frac{6}{5} & 0 & \frac{L}{10} & 0 \\ 0 & 0 & 0 & \frac{-I_z}{A} & 0 & 0 & 0 & 0 & 0 & \frac{I_z}{A} & 0 & 0 \\ 0 & 0 & \frac{-L}{10} & 0 & \frac{-L^2}{30} & 0 & 0 & 0 & \frac{L}{10} & 0 & \frac{2L^2}{15} & 0 \\ 0 & \frac{L}{10} & 0 & 0 & 0 & \frac{-L^2}{30} & 0 & \frac{-L}{10} & 0 & 0 & 0 & \frac{2L^2}{15} \end{bmatrix} \quad (4.13)$$

And,

$$\left[K_{NA_2} \right]^e = \frac{EI_{xy}(U_7 - U_1)}{L^4} \begin{bmatrix} 0 & 0 & 0 & 0 & 0 & 0 & 0 & 0 & 0 & 0 & 0 & 0 \\ 0 & 6L^2 & 0 & 0 & 0 & 3L^3 & 0 & -6L^2 & 0 & 0 & 0 & 3L^3 \\ 0 & 0 & 6L^2 & 0 & -3L^3 & 0 & 0 & 0 & -6L^2 & 0 & -3L^3 & 0 \\ 0 & 0 & 0 & 0 & 0 & 0 & 0 & 0 & 0 & 0 & 0 & 0 \\ 0 & 0 & -3L^3 & 0 & 2L^4 & 0 & 0 & 0 & 3L^3 & 0 & L^4 & 0 \\ 0 & 3L^3 & 0 & 0 & 0 & 2L^4 & 0 & -3L^3 & 0 & 0 & 0 & L^4 \\ 0 & 0 & 0 & 0 & 0 & 0 & 0 & 0 & 0 & 0 & 0 & 0 \\ 0 & -6L^2 & 0 & 0 & 0 & -3L^3 & 0 & 6L^2 & 0 & 0 & 0 & -3L^3 \\ 0 & 0 & -6L^2 & 0 & 3L^3 & 0 & 0 & 0 & 6L^2 & 0 & 3L^3 & 0 \\ 0 & 0 & 0 & 0 & 0 & 0 & 0 & 0 & 0 & 0 & 0 & 0 \\ 0 & 0 & -3L^3 & 0 & L^4 & 0 & 0 & 0 & 3L^3 & 0 & 2L^4 & 0 \\ 0 & 3L^3 & 0 & 0 & 0 & L^4 & 0 & -3L^3 & 0 & 0 & 0 & 2L^4 \end{bmatrix} \quad (4.14)$$

$[K_{NT}]^e$, which represents coupling between torsion and flexure is known as a contribution of geometric stiffness. Equation (4.15), shows it is also varied with time while it mainly depends on rotational displacements U_4 and U_{10} instead of U_1 and U_7 which dominates matrixes $[K_{NA1}]^e$ and $[K_{NA2}]^e$.

$$[K_{NT}]^e = (1+2\nu) \frac{GI_z (U_{10} - U_4)}{L^2} \begin{bmatrix} 0 & 0 & 0 & \frac{1+\nu}{2(1+2\nu)} & 0 & 0 & 0 & 0 & 0 & -\frac{1+\nu}{2(1+2\nu)} & 0 & 0 \\ 0 & 0 & 0 & 0 & -1 & 0 & 0 & 0 & 0 & 0 & 1 & 0 \\ 0 & 0 & 0 & 0 & 0 & -1 & 0 & 0 & 0 & 0 & 0 & 1 \\ 0 & 0 & 0 & 0 & 0 & 0 & 0 & 0 & 0 & 0 & 0 & 0 \\ 0 & -1 & 0 & 0 & 0 & 0 & 0 & 1 & 0 & 0 & 0 & \frac{-L}{2} \\ 0 & 0 & -1 & 0 & 0 & 0 & 0 & 0 & 1 & 0 & \frac{L}{2} & 0 \\ 0 & 0 & 0 & -\frac{1+\nu}{2(1+2\nu)} & 0 & 0 & 0 & 0 & 0 & \frac{1+\nu}{2(1+2\nu)} & 0 & 0 \\ 0 & 0 & 0 & 0 & 1 & 0 & 0 & 0 & 0 & 0 & -1 & 0 \\ 0 & 0 & 0 & 0 & 0 & 1 & 0 & 0 & 0 & 0 & 0 & -1 \\ 0 & 0 & 0 & 0 & 0 & 0 & 0 & 0 & 0 & 0 & 0 & 0 \\ 0 & 1 & 0 & 0 & 0 & \frac{L}{2} & 0 & -1 & 0 & 0 & 0 & 0 \\ 0 & 0 & 1 & 0 & -\frac{L}{2} & 0 & 0 & 0 & -1 & 0 & 0 & 0 \end{bmatrix} \quad (4.15)$$

4.6 The Damping Matrix

The characterization of damping is important in making accurate predictions of both the true response and the frequency response of any device or structure dominated by energy dissipation. The process of modeling damping matrixes and experimental verification is challenging because damping cannot be determined via static tests, in the same way as mass and stiffness.

Furthermore, damping is more difficult to determine from dynamic measurements than natural frequency.

The damping matrix includes two parts: $[C_D]^e$ and $[C_N]^e$, which represents dissipative damping matrix and non-dissipative damping matrix respectively. As shown in equation (4.16).

$$[C]^e = [C_D]^e + [C_N]^e \quad (4.16)$$

$$[C_N]^e = \frac{\Omega J_z}{L} \begin{bmatrix} 0 & 0 & 0 & 0 & 0 & 0 & 0 & 0 & 0 & 0 & 0 & 0 \\ 0 & 0 & \frac{6}{5} & 0 & \frac{-L}{10} & 0 & 0 & 0 & \frac{-6}{5} & 0 & \frac{-L}{10} & 0 \\ 0 & \frac{-6}{5} & 0 & 0 & 0 & \frac{-L}{10} & 0 & \frac{6}{5} & 0 & 0 & 0 & \frac{-L}{10} \\ 0 & 0 & 0 & 0 & 0 & 0 & 0 & 0 & 0 & 0 & 0 & 0 \\ 0 & \frac{L}{10} & 0 & 0 & 0 & \frac{2L^2}{15} & 0 & \frac{-L}{10} & 0 & 0 & 0 & \frac{-L^2}{30} \\ 0 & 0 & \frac{L}{10} & 0 & \frac{-2L^2}{15} & 0 & 0 & 0 & \frac{-L}{10} & 0 & \frac{L^2}{30} & 0 \\ 0 & 0 & 0 & 0 & 0 & 0 & 0 & 0 & 0 & 0 & 0 & 0 \\ 0 & 0 & \frac{-6}{5} & 0 & \frac{L}{10} & 0 & 0 & 0 & \frac{6}{5} & 0 & \frac{L}{10} & 0 \\ 0 & \frac{6}{5} & 0 & 0 & 0 & \frac{L}{10} & 0 & \frac{-6}{5} & 0 & 0 & 0 & \frac{L}{10} \\ 0 & 0 & 0 & 0 & 0 & 0 & 0 & 0 & 0 & 0 & 0 & 0 \\ 0 & \frac{L}{10} & 0 & 0 & 0 & \frac{-L^2}{30} & 0 & \frac{-L}{10} & 0 & 0 & 0 & \frac{2L^2}{15} \\ 0 & 0 & \frac{L}{10} & 0 & \frac{L^2}{30} & 0 & 0 & 0 & \frac{-L}{10} & 0 & \frac{-2L^2}{15} & 0 \end{bmatrix} \quad (4.17)$$

Where,

$$[C_D]^e = \alpha[M]^e + \beta[K]^e \quad (4.18)$$

Equation (4.18) shows that $[C_D]^e$ is a function of $[M]^e$ and $[K]^e$, which means this part of damping matrix relates to mass and stiffness of drilling pipes. There are two coefficients α and β , which are weighting parameters that allow system damping to be adjusted.

In equations (4.8) to (4.18), E , ν and G represent elastic modulus, Poisson's ratio and shear modulus respectively. Those are physical parameters for the drillstring. I_x , I_y and I_z are axial moment of inertia for each beam element, Ω is rotation speed of the drillstring, J_z is mass moment of inertia for each beam element around z-axis. ρ , A and L are density, transverse sectional area and the length of beam element, respectively.

4.7 Gravity Force Vector

Although the gravity is evenly distributed on the beam element, during the simulation, equivalent force is used on both nodes of one element to replace distributed gravity.

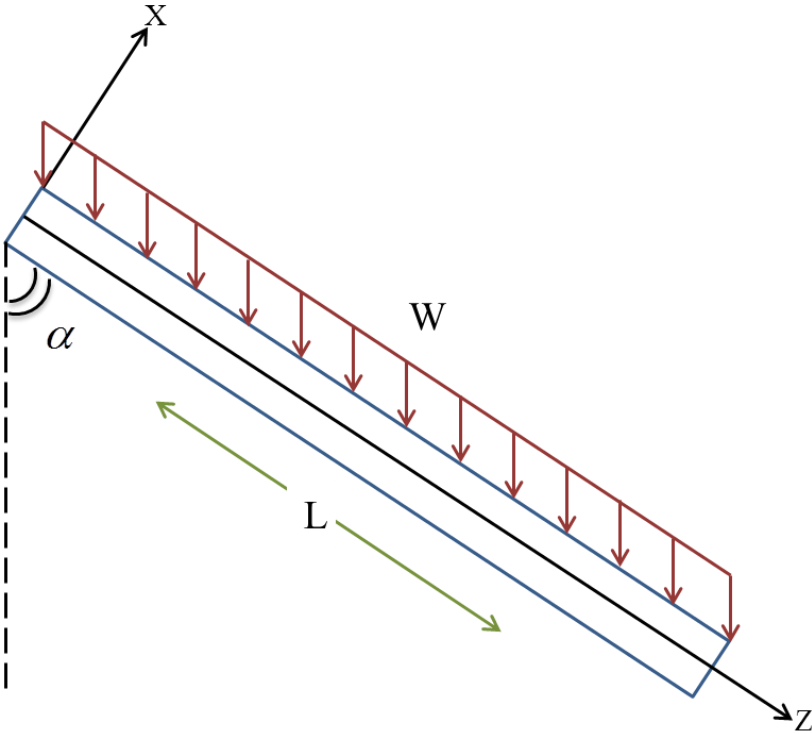


Figure 4.2 Gravity Distributions for One Beam Element

Based on mathematical analysis, we get equation (4.19).

$$[F_{grav}]^e = \left[\begin{array}{cccccccccccc} \frac{q_z L}{2} & -\frac{q_x L}{2} & 0 & 0 & 0 & \frac{q_x L^2}{2} & \frac{q_z L}{2} & \frac{q_x L}{2} & 0 & 0 & 0 & -\frac{q_x L^2}{2} \end{array} \right]^T \quad (4.19)$$

4.8 Horizontal Model

To make it easier to establish the mathematic model, all mechanical analysis is local-coordinate based. Since in vertical coordinate system, all nodes are using the same directions of the X axis and Y axis, elements can be assembled nose to tail vertically and directly. However, in horizontal system, the directions of X axis and Y axis for different node can be different (inclination change and azimuth change), in that situation, we can't assemble elements together directly like the way in vertical system.

Figure 4.3 shows the difference between global coordinate system and local coordinate system.

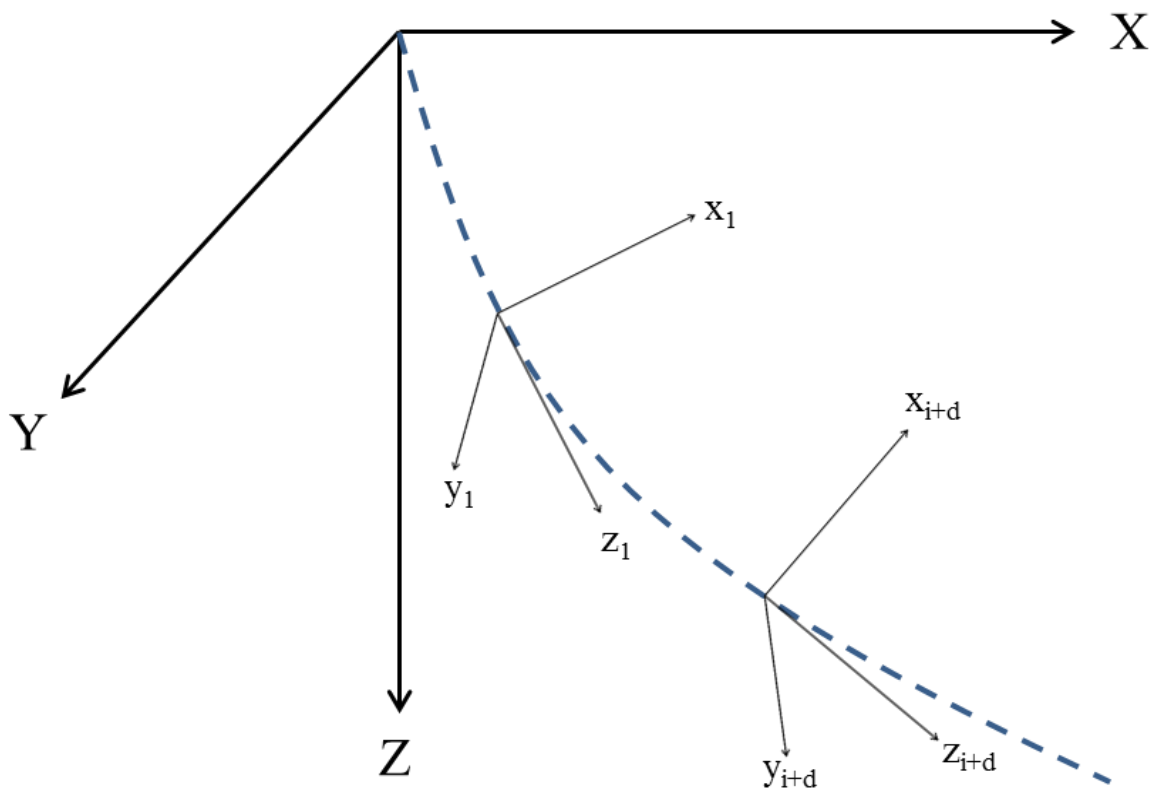


Figure 4.3 Local and Global Coordinate systems for Horizontal Well

In order to solve this problem, we introduce the "Transformation Matrix". The transformation Matrix is the matrix that serves for transformation between a global coordinate system and a

local coordinate system. This matrix is used to transform mass matrix, stiffness matrix, damping matrix, force vectors, displacement vectors, velocity vectors and acceleration vectors from local coordinate to global coordinates.

This concept can be understood as a “virtual-vertical” well. In a vertical well, the Z-axis is a straight line from surface to bottomhole. While in a horizontal well (virtual-vertical well), the Z-axis is assumed along the trajectory line. In that case, we can assemble the matrix together, nose to tail.

To transform the coordinate system from local to global, specific rotations must be done in a specific order. As shown in Figure 4.4, only two parameters are related to coordinate system change: inclination and azimuth.

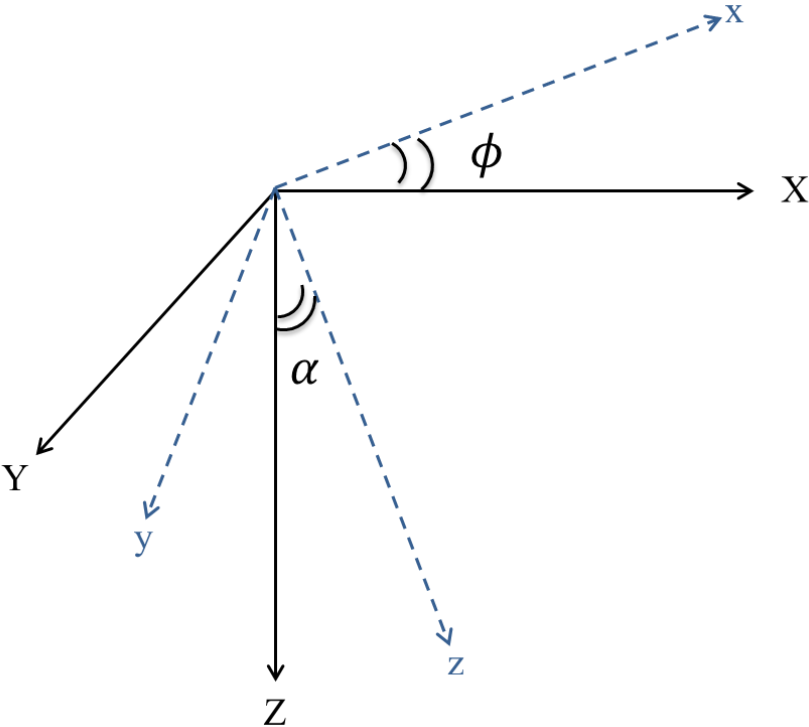


Figure 4.4 Global Coordinate and Local Coordinate system

In Fig 4.4, α is inclination and ϕ is azimuth. Two steps must be followed to rotate the coordinate system from local to global, there are.

Step One: rotate local coordinate system around the Z-axis to offset azimuth changes. Inclination remains unchanged. As Figure 4.5 shows.

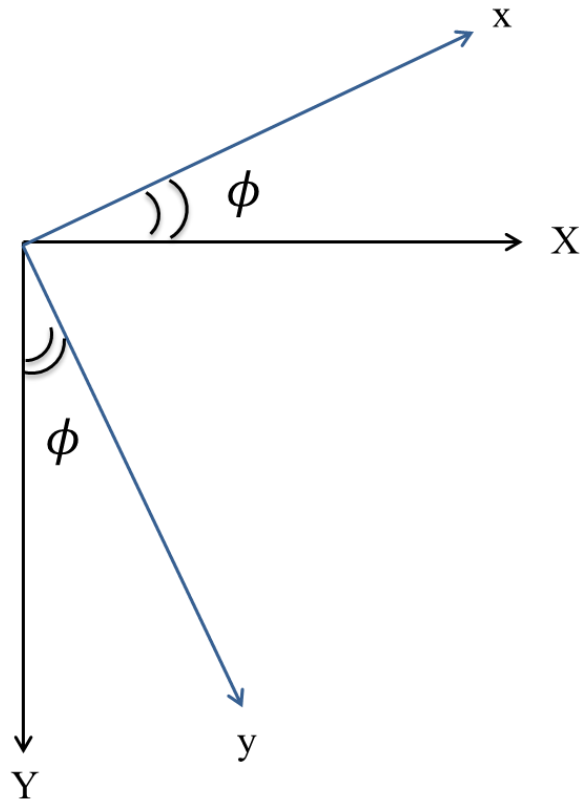


Figure 4.5 Rotate around Z-axis

Based on the relationship in Fig 4.5, we can get equation set (4.20):

$$\begin{bmatrix} z = Z \\ \cos \phi \cdot x - \sin \phi \cdot y = X \\ \sin \phi \cdot x + \cos \phi \cdot y = Y \end{bmatrix} \quad (4.20)$$

Based on 4.20, we can get the first part of Transformation Matrix (4.21):

$$\begin{bmatrix} 1 & 0 & 0 & & & \\ 0 & \cos \phi & -\sin \phi & & & 0 \\ 0 & \sin \phi & \cos \phi & & & \\ & & & 1 & 0 & 0 \\ & & & 0 & \cos \phi & -\sin \phi \\ & & & 0 & \sin \phi & \cos \phi \end{bmatrix} \quad (4.21)$$

Step Two: rotate local coordinate system around the Y-axis to offset inclination changes. Azimuth remains unchanged. As Figure 4.6 shows.

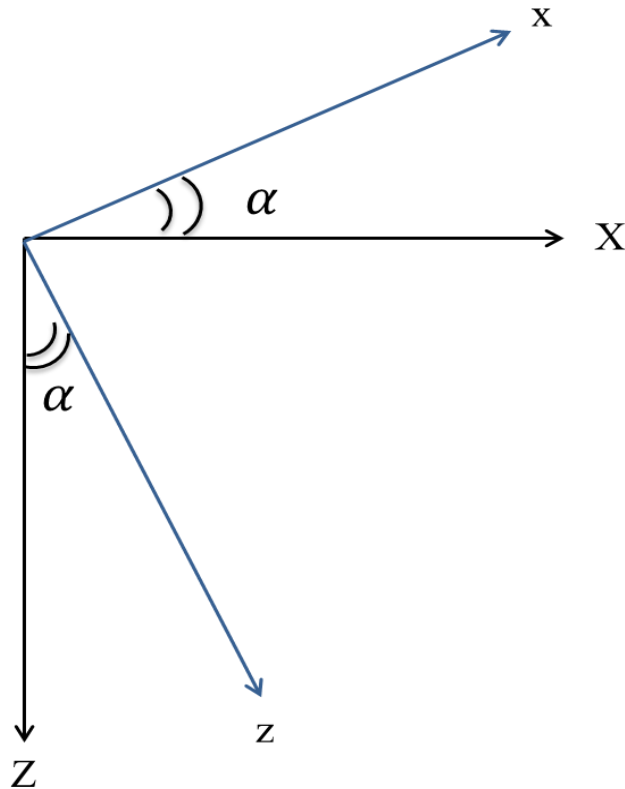


Figure 4.6 Rotate around Y-axis

Based on the relationship in Fig 4.6, we can get equation set (4.22):

$$\begin{cases} \cos \alpha \cdot z - \sin \alpha \cdot x = Z \\ \sin \alpha \cdot z + \cos \alpha \cdot x = X \\ y = Y \end{cases} \quad (4.22)$$

Based on 4.22, we can get the second part of Transformation Matrix (4.23):

$$\begin{bmatrix} \cos \alpha & -\sin \alpha & 0 & & & \\ \sin \alpha & \cos \alpha & 0 & & & \\ 0 & 0 & 1 & & & \\ & & & \cos \alpha & -\sin \alpha & 0 \\ & 0 & & \sin \alpha & \cos \alpha & 0 \\ & & & 0 & 0 & 1 \end{bmatrix} \quad (4.23)$$

$$[U_{Global}]^e = T^T \cdot [u_{Local}]^e \quad (4.26)$$

Where the T^T is the reversed-transformation matrix. Matrix T is an orthogonal matrix, therefore, $T^T = T^{-1}$ and $T^T \cdot T = E$. For $[\dot{U}]^e$ and $[\ddot{U}]^e$ vectors, we have the same format. Based on the relationship between the local coordinate and the global coordinate, we can get the following equations:

$$[\dot{U}_{Global}]^e = T^T \cdot [\dot{u}_{Local}]^e \quad (4.27)$$

$$[\ddot{U}_{Global}]^e = T^T \cdot [\ddot{u}_{Local}]^e \quad (4.28)$$

$$[M_{Global}]^e = T^T \cdot [M_{Local}]^e \cdot T \quad (4.29)$$

$$[K_{Global}]^e = T^T \cdot [K_{Local}]^e \cdot T \quad (4.30)$$

$$[C_{Global}]^e = T^T \cdot [C_{Local}]^e \cdot T \quad (4.31)$$

$$[F_{Global}]^e = T^T \cdot [F_{Local}]^e \quad (4.32)$$

4.9 Global Matrixes

After converting all vectors and matrixes from local coordinates to global coordinates, we can start to assemble mass matrixes, stiffness matrixes, damping matrixes, force vectors, displacement vectors, velocity vectors and accelerating vectors.

All matrixes, contain components for two nodes, so we can write any matrix in a simplified format, for example:

$$[M]^i = \begin{bmatrix} [M_{11}^i]_{6 \times 6} & [M_{12}^i]_{6 \times 6} \\ [M_{21}^i]_{6 \times 6} & [M_{22}^i]_{6 \times 6} \end{bmatrix} \quad (4.33)$$

The next step is to assemble the mass matrixes for each element, using the principle of nose to tail, which is shown as matrix (4.34):

During drilling operation, the drilling pipes are suspended by a hook on the surface, which will give a feedback force as hookload. With different BHA (Bottom Hole Assembly), different sub tools are required, for the purpose of steering, including several stabilizers. Generally, these tools can be a part of boundary conditions.

In this paper, the main boundaries are: rotary table, drilling bit and stabilizers, which as shown in Figure 4.7. On the surface, the suspension system will be simplified as a spring, the stiffness coefficient of which is KH. The hookload on the surface can be calculated using equation (4.39):

$$F_{hookload} = KH \cdot U_z^1 \tag{4.39}$$

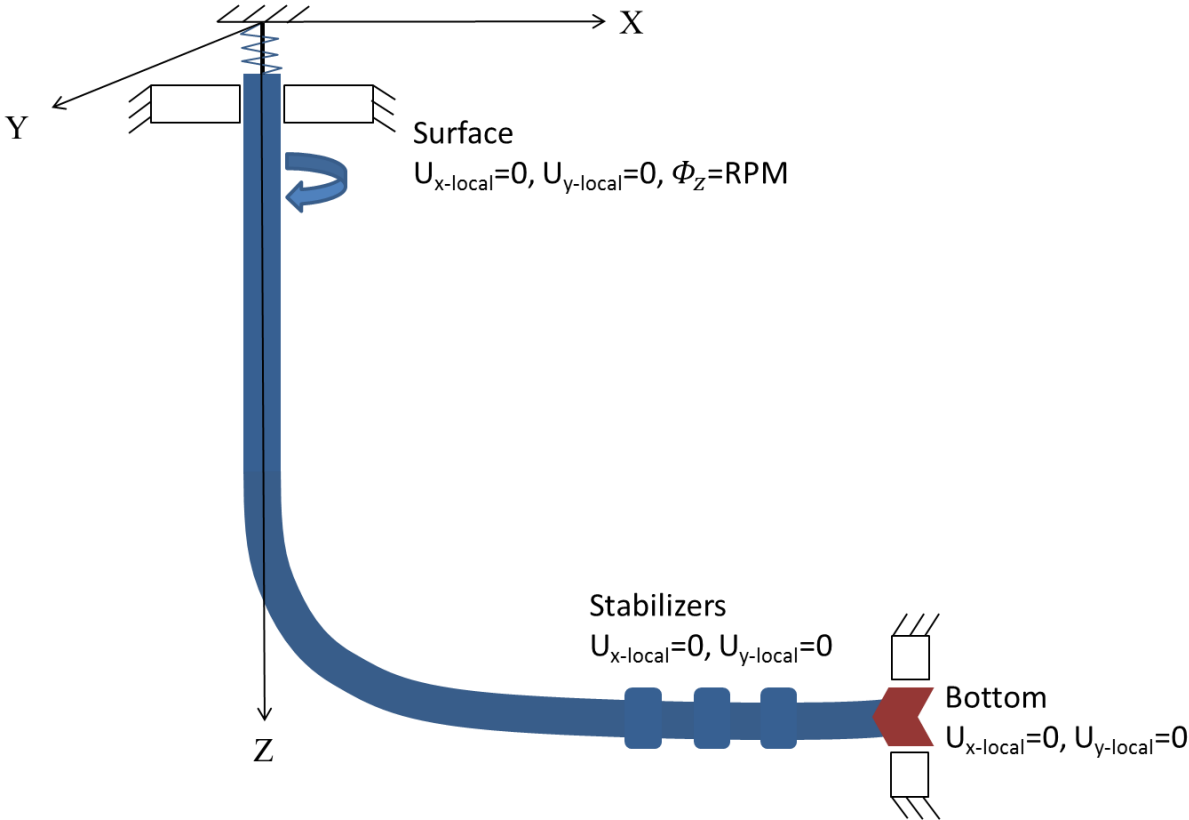


Figure 4.7 Main Boundaries for Whole Well

Figure 4.7 shows how the boundary conditions on the surface are mainly constraining the displacement on x-axis and y-axis (Local coordinate system based), while the drillstring can still move on axial direction. The stabilizers mainly constrain the displacement on x-axis and y-axis

(Local coordinate system based). For the case of bottom boundary conditions, the constraint mainly affects the x-axis and y-axis.

Conditions from two drilling operations and one general constraint will be input into the model, only considering the constraint on surface and bottom (the constraint from Stabilizers will be detailed discussed later on). Two drilling operations and one general constraint condition are considered:

(1). Rotating Drilling

$$U_x^1 = 0$$

$$U_y^1 = 0$$

$$\Phi_z^1 = 2 \times \pi \times RPM$$

$$T_z^1 = Torque_{surface}$$

$$U_x^n = 0$$

$$U_y^n = 0$$

$$F_z^n = WOB_{bottom}$$

$$T_z^n = Torque_{bottom}$$

Where,

RPM: rotary speed of rotary table

$Torque_{surface}$: torque on rotary table

1: the 1st element

WOB: the force load on bit at bottom

$Torque_{bottom}$: torque on the bit

n: the last drillstring element

(2). Sliding Drilling, tripping in/out

$$U_x^1 = 0$$

$$U_y^1 = 0$$

$$F_z^1 = 0$$

$$U_x^n = 0$$

$$U_y^n = 0$$

$$F_z^n = 0$$

$$T_z^n = 0$$

At bottom hole, the radial displacement is constrained because bit size is equal to or slightly less than the hole size. The axial displacement and rotation there is released and capable of moving in any direction. The subscripts and superscripts have the same meaning as introduced in rotating drilling operation.

(3). Hole Size constraint

Drillstrings can move in any direction if there are no other special constraints. Hole size is a natural physical constraint / limitation to the drillstring (not considering reaming caused by radical movement of drillstrings), which means the radial displacement is restrained in the clearance between drillstring and wellbore wall.

Figure 4.8 shows the hole size constraint.

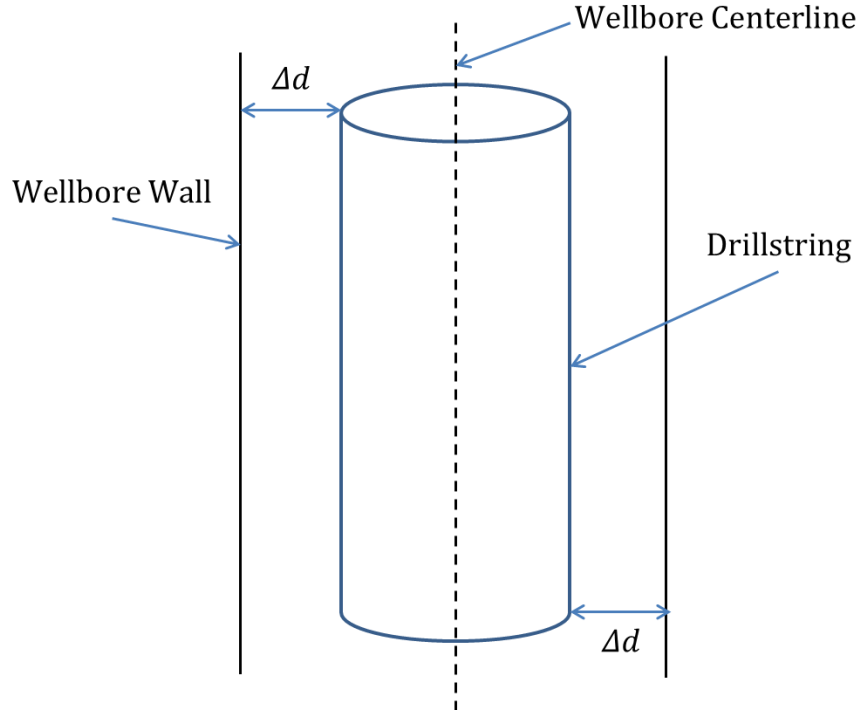


Figure 4.8 Hole Size Constraint

Equation (4.40) shows the relationship between radical displacement and the gap, we can have got this:

$$\sqrt{u_x^2 + u_y^2} < \Delta d \quad (4.40)$$

Where, $\Delta d = \frac{D - d}{2}$ is the clearance between drillstring/BHA and wellbore wall, D is the diameter of the wellbore and d is the diameter of drillstring/BHA. If the condition of equation (4.40) is not met, for example: $\sqrt{u_x^2 + u_y^2} \geq \Delta d$, then there will be a criteria condition for calculating torque and drag, which will greatly influence real DWOB.

4.11 Solution – Wilson Theta Method

Numerical methods for the nonlinear analysis of structures are massively used in Finite Element Method. In order to solve those equations with step-by-step time based methods, many scholars have spent lots of time for finding the solution. For now, there are many methods aiming at analyzing dynamic vibration equations. In this paper, Wilson Theta Method is used as solution method.

The time-based equation that we are using in FEM is:

$$[M]^e \{\ddot{U}\}^e + [C]^e \{\dot{U}\}^e + [K]^e \{U\}^e = \{F\}^e \quad (4.41)$$

The Wilson Theta Method assumes a linear change of acceleration within a time interval $[t \ t + \theta\Delta t]$ with time variable τ , where $\theta > 1$, as shown in Figure 4.9.

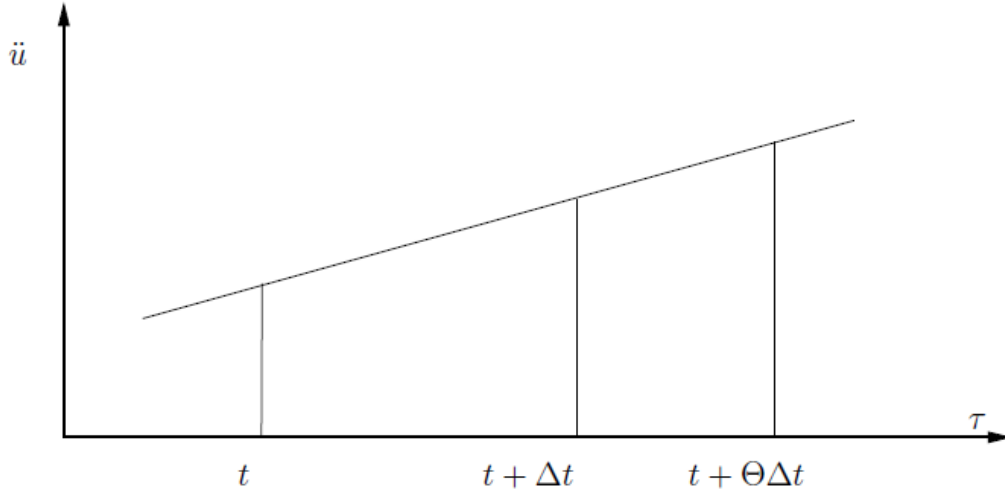


Figure 4.9 Linear Change of Acceleration for a Dynamic Vibration System (Wilson, 1973)

To use this method for FEM analysis, equation (4.41) is written as:

$$[\tilde{M}] \{\ddot{U}_{t+\theta\Delta t}\} = \{FF_{t+\theta\Delta t}\} \quad (4.42)$$

Where,

$$[\tilde{M}] = [M] + \frac{\theta\Delta t}{2} [C] + \frac{(\theta\Delta t)^2}{6} [K] \quad (4.43)$$

And,

$$\{FF_{t+\theta\Delta t}\} = \{F_{t+\theta\Delta t}\} - [C] \left(\{\dot{U}_t\} + \frac{\theta\Delta t}{2} \{\ddot{U}_t\} \right) - [K] \left(\{U_t\} + \theta\Delta t \{\dot{U}_t\} + \frac{(\theta\Delta t)^2}{3} \{\ddot{U}_t\} \right) \quad (4.44)$$

In equation (4.42), $[\tilde{M}]$ is the equivalent mass matrix, which is a function of mass matrix, stiffness matrix and damping matrix. In equation (4.44), $\{FF_{t+\theta\Delta t}\}$ is the equivalent force vector related to damping matrix and stiffness matrix.

The solution of equation (4.42) gives acceleration $\ddot{U}_{t+\theta\Delta t}$ for the first time step, based on the relationship between acceleration, velocity and displacement can be retrieved, shown in Figure 4.9:

$$\{\ddot{U}_{t+\Delta t}\} = \frac{1}{\theta}\{\ddot{U}_{t+\theta\Delta t}\} + \left(1 - \frac{1}{\theta}\right)\{\ddot{U}_t\} \quad (4.45)$$

$$\{\dot{U}_{t+\Delta t}\} = \{\dot{U}_t\} + \frac{\Delta t}{2\theta}\{\ddot{U}_{t+\theta\Delta t}\} + (2\theta - 1)\frac{\Delta t}{6\theta}\{\ddot{U}_t\} \quad (4.46)$$

$$\{U_{t+\Delta t}\} = \{U_t\} + \Delta t\{\dot{U}_t\} + \frac{\Delta t^2}{6\theta}\{\ddot{U}_{t+\theta\Delta t}\} + (3\theta - 1)\frac{\Delta t^2}{6\theta}\{\ddot{U}_t\} \quad (4.47)$$

The value of θ must be carefully chosen. A bad choice will make it difficult to get a convergent result. Usually when $\theta \geq 1.37$, the method is unconditionally stable and convergent for a linear dynamic system. A value of 1.4 is often used for nonlinear dynamic system, which is exactly the value used in this thesis for FEM analysis.

4.12 Stabilizer

A drilling stabilizer is a piece of downhole equipment used on the bottom hole assembly (BHA) of a drill string. Its purpose is to mechanically stabilize the BHA in the borehole, to avoid unintentional sidetracking, and vibrations, and to ensure the quality of the hole being drilled. It is composed of a hollow cylindrical body and stabilizing blades, both made of high-strength steel. The blades can be either straight or spiraled, and are hard-faced for wear resistance. Figure 4.9 shows three typical stabilizers.

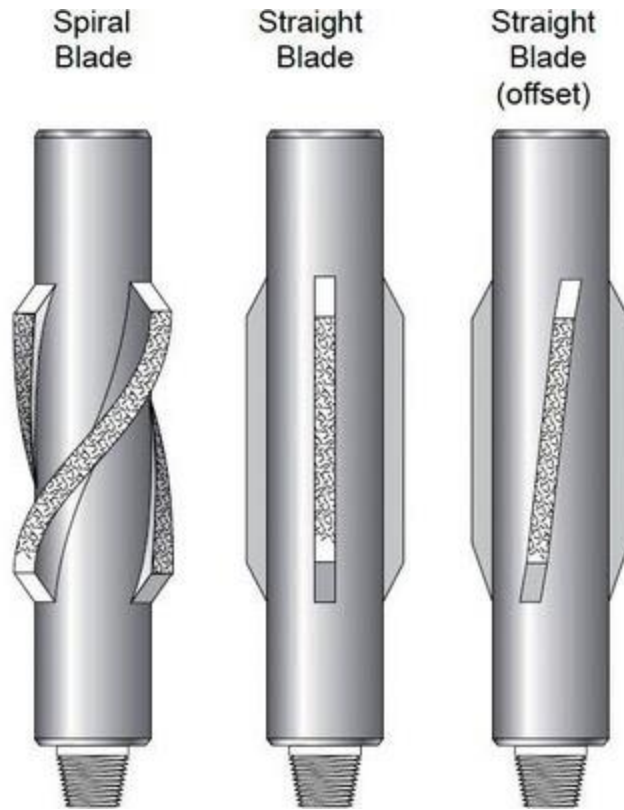


Figure 4.10 Stabilizers with three different blades (Deepak, 2014)

Inside our model, for the section or element where stabilizers are placed, we need to modify the stiffness matrix, input acceleration and output acceleration to meet the physical feature of stabilizers.

Instead of modifying stiffness matrix, equivalent mass matrix is the matrix needs to be modified.

The principle of modifying matrix is to setup zero for all non-diagonal components but setup 1 for diagonal component. Since the stabilizer will only be placed at one node, it will only affect 6 DOF (degrees of freedom). However, for stabilizer, it only restrains the displacement in radical directions, and two bending rotations, which means only 4 DOF will be modified.

After modification, $[\tilde{M}]$ will be expressed as:

$$[\tilde{M}]^i = \begin{bmatrix} \tilde{M}_{11}^i & 0 & 0 & 0 & 0 & 0 \\ 0 & -1 & 0 & 0 & 0 & 0 \\ 0 & 0 & -1 & 0 & 0 & 0 \\ 0 & 0 & 0 & \tilde{M}_{33}^i & 0 & 0 \\ 0 & 0 & 0 & 0 & -1 & 0 \\ 0 & 0 & 0 & 0 & 0 & -1 \end{bmatrix} \quad (4.48)$$

Acceleration, for both inputting and outputting must also be modified, for each acceleration

vector $[\ddot{U}]^i = [\ddot{U}_1^i \quad \ddot{U}_2^i \quad \ddot{U}_3^i \quad \ddot{U}_4^i \quad \ddot{U}_5^i \quad \ddot{U}_6^i]$:

$$\ddot{U}_2^i = 0$$

$$\ddot{U}_3^i = 0$$

$$\ddot{U}_5^i = 0$$

$$\ddot{U}_6^i = 0$$

These modifications must be made after every iteration until the end of the calculation.

4.13 Computational Logic

Figure 4.11 is a flowchart showing the logic order of FEM:

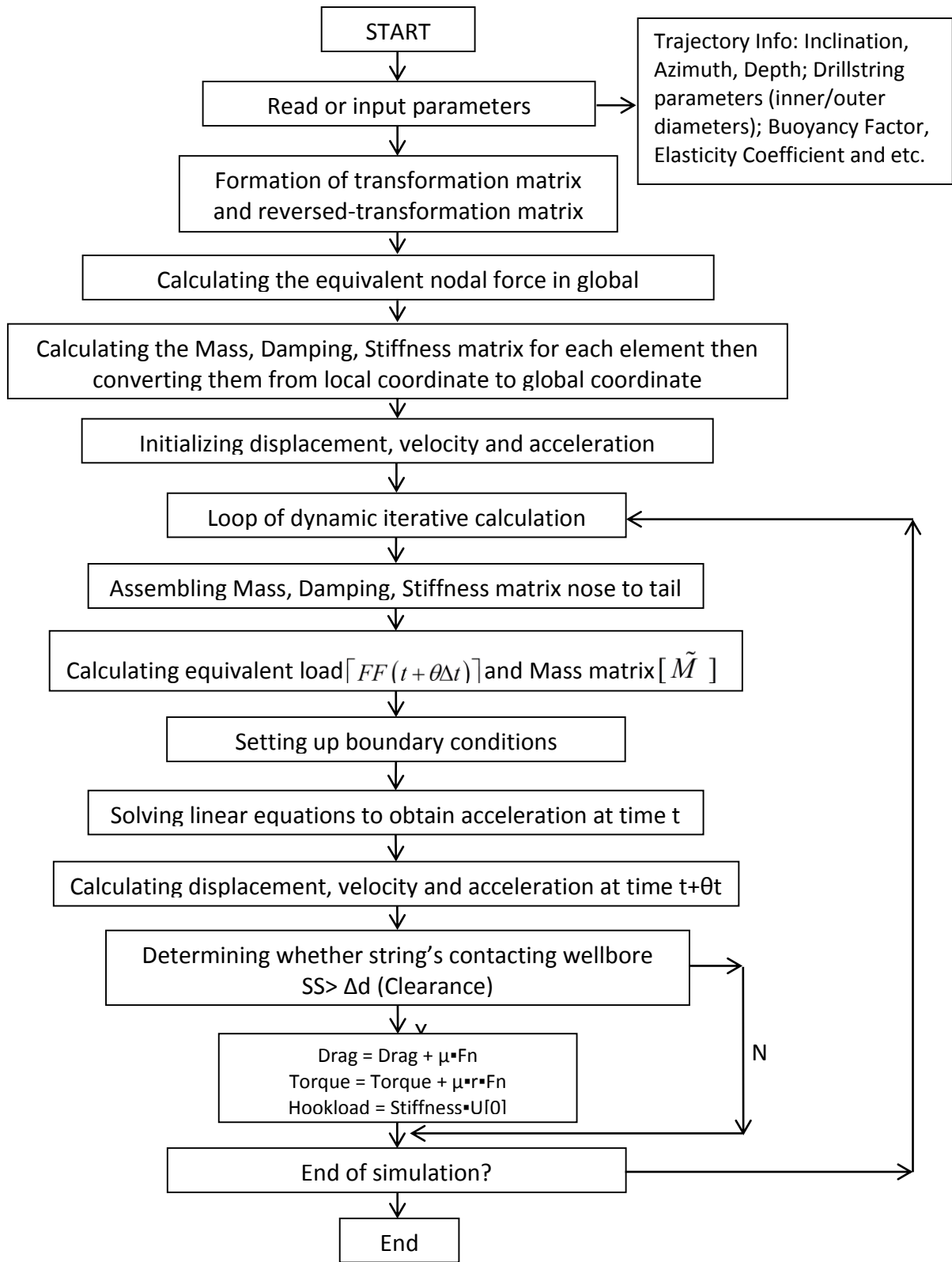


Figure 4.11 Flowchart of FEM Program

4.14 Programming Language

After completing the work from section 4.1 to section 4.12, one last step remains before the simulation experiments can begin: computer programming.

C++ is the chosen programming language for this research and Visual Studio 2012 is the programming platform. C++ is a general purpose programming language that is free-form and compiled. It is widely regarded as an intermediate-level language, as it comprises both high-level and low-level language features. C++ provides imperative, object-oriented and generic programming features.

A few advantages of C++:

- 1.) Vendor-neutral: C++ standard is a commonly used, standard language that is the same in any platform or compiler;
- 2). Multi-platforms: C++ can be used in Windows or Linux operation systems;
- 3). Multi-paradigm: C++ allows the use and penalty-free mixing of procedural, generic functional programming.

Chapter 5 : SIMULATION EXPERIMENTS

This chapter includes three main parts: data calculation process, results and discussion. Both the analytical method and Finite Element Method will be used to calculate friction factor and DWOB, using field data. The simulation data will then be compared with measured data from an actual well.

The experiment requires the following information and equipment:

1. 10-second based real-time drilling data, measured DWOB by CoPilot
2. Survey Data
3. Macro-Enabled Excel spreadsheet with imbedded analytical model programming code
4. New project in Visual Studio 2012 with FEM programming code
5. Quad-core processor computer

The 10s based real-time drilling data used in this experiment was collected from the Pason Systems data hub. This well utilized in this analysis was already completed in 2012.

The Excel code and Visual Studio code were programmed, debugged, and input before running the field data.

5.1 Field Data

Because this research was partly funded by Talisman Energy and Pason Systems Corporation, an Akita Rig where Talisman was the operator was chosen for analysis. The analysis performed and conclusions drawn are based on comparisons of DWOB measured by Baker Hughes CoPilot on this single well.

5.1.1 Survey Data

This is a horizontal well comprising several sections, at the following measured depths:

1. Vertical section down to 1705.2m until Kick off point (KOP);
2. Build and turn section from 1705.2m to 2351.7m until landing at the heel point;
3. Horizontal section from 2351.7m to 3844m until reaching the toe.

The survey data was entered into the Landmark software, to create a schematic of this well. Figure 5.1 is a 3D diagram of the well trajectory. Figure 5.2 is the transversal projection and Figure 5.3 is the top view.

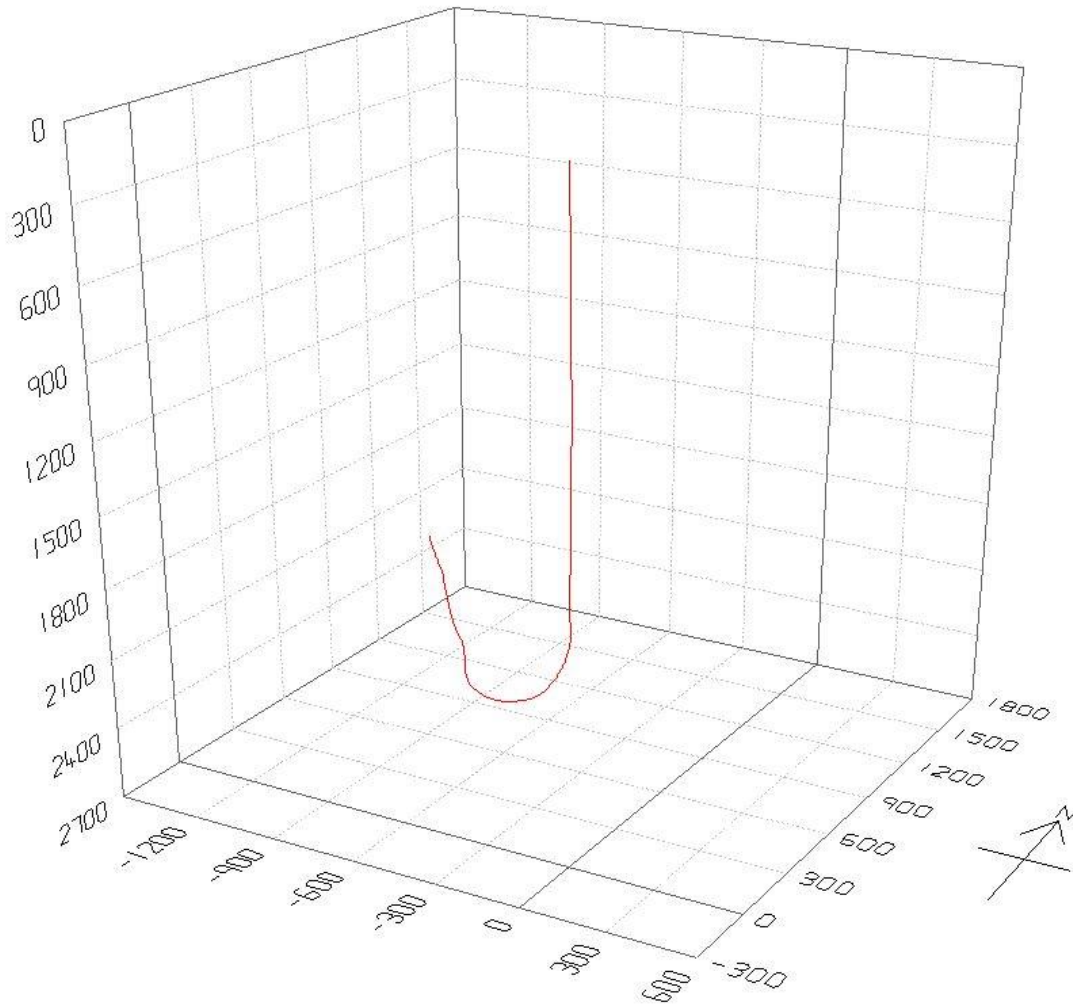


Figure 5.1 Well Trajectory 3D Diagram

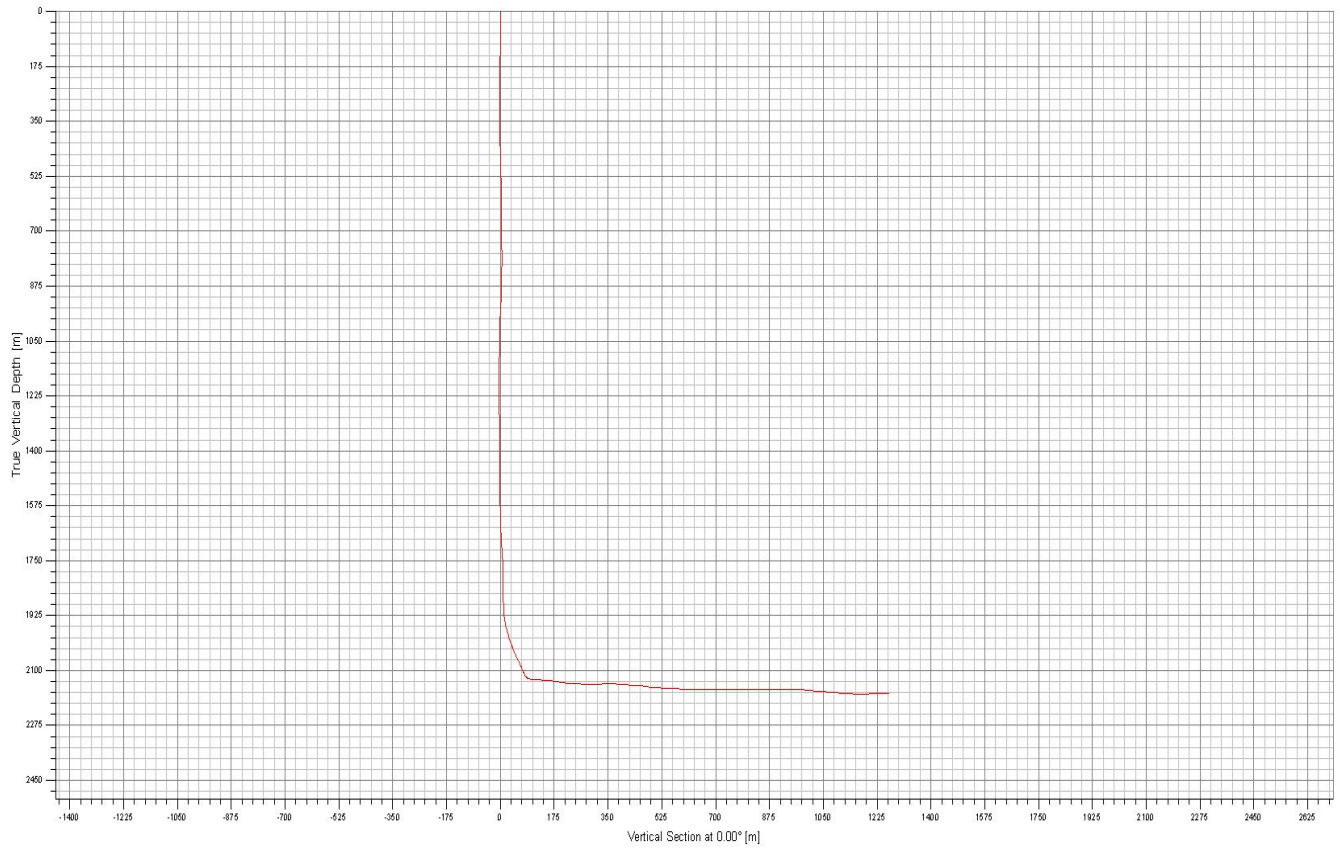


Figure 5.2 Well Trajectory Transversal Projection

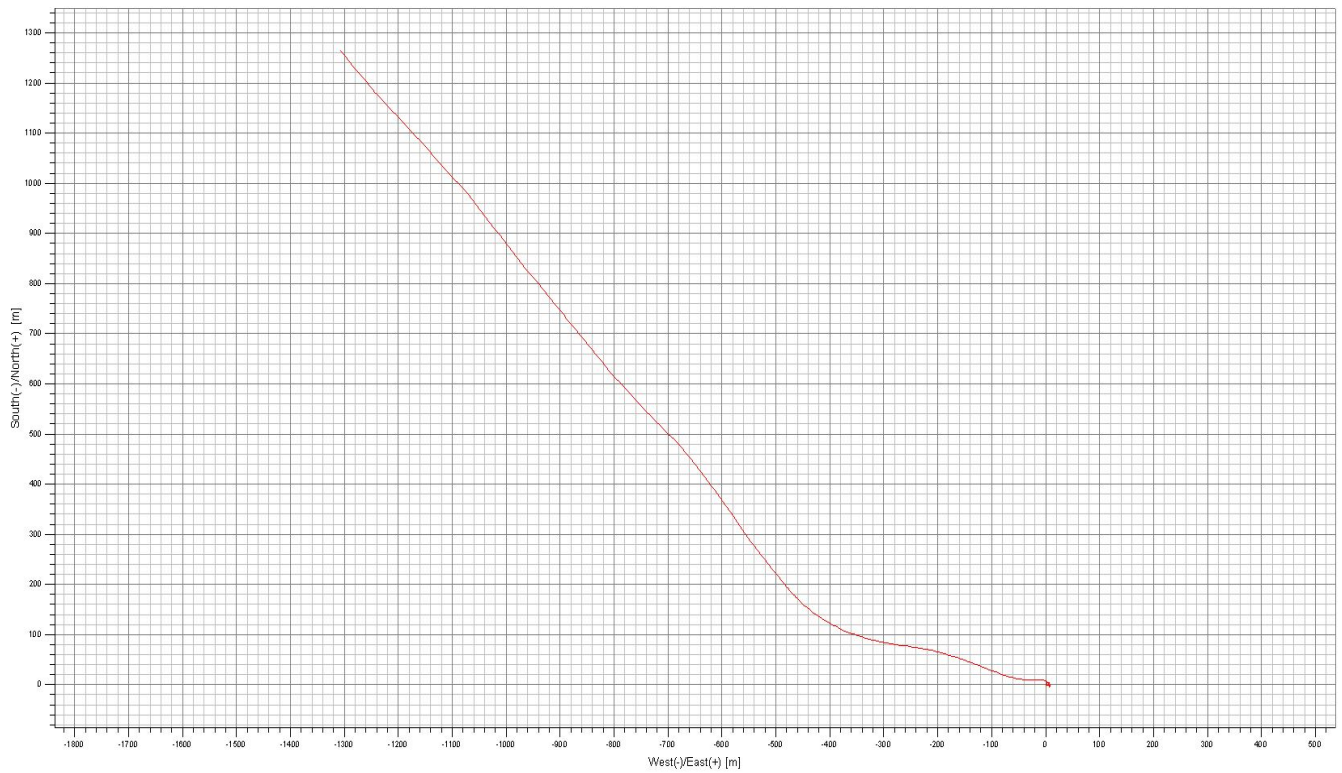


Figure 5.3 Well Trajectory Top View

The location of this well was not available for this research so the pad site location data was not entered into the system.

5.1.2 Real-time Drilling Data

Real-time drilling data collected includes: time, Bit Depth, Hole Depth, on Bottom Rate of Penetration, hookload, Weight on Bit (referred to as SWOB here, since it is collected at the surface panel), revolution per minute (RPM), standpipe pressure and CoPilot downhole weight on bit (DWOB).

Based on the survey data, at 2500m, the inclination is around 90 degrees, and the inclination is maintained until drill bit reaches target. In this verification project, 10-second based drilling data was downloaded from Pason datahub.

Table 5.1 shows the detailed drillstring component information, gathered from the drilling operation electronic datasheet:

Table 5.1 Drillstring Components (Akita Rig, Talisman)

Component	Length (m)	Unit Weight (kdaN/m)	OD(m)	ID(m)
Bit & BHA	50.89	0.07073	0.126	0.06456
HWDP	168.97	0.03684	0.1016	0.065
Drillpipe	1717.32	0.02174	0.1016	0.082
HWDP	197.05	0.03684	0.1016	0.065
Drillpipe		0.02174	0.1016	0.082

5.1.3 Data Choosing Principle

Both the Analytical Model and the FEM require a friction factor before DWOB can be calculated, therefore, the friction factor is calculated first.

When calculating the friction factor, off-bottom data is used. Off-bottom is when we are circulating and rotation above the bit lowering the drillstring. This means there is no contact (WOB) with the formation which happens between connections. In both methods, the procedure to calculate the friction factor between connections is to increase the friction factor (at increasing step of 0.002) for each iteration until the “calculated hookload” equals to the field measured hookload. When the calculation stops, the applied value is the friction factor for that depth.

After calculating the friction factor, the on-bottom drilling data collected at surface will be used to calculate DWOB. On-bottom is the situation when the bit is in contact with the formation which means there is contacting force (WOB). In this process, the friction factor will be a constant value derived from the above described step, and an increasing DWOB will be applied until the “calculated hookload” equals to the real field measured hookload.

Both off-bottom and on-bottom scenarios are shown in Figure 5.4.

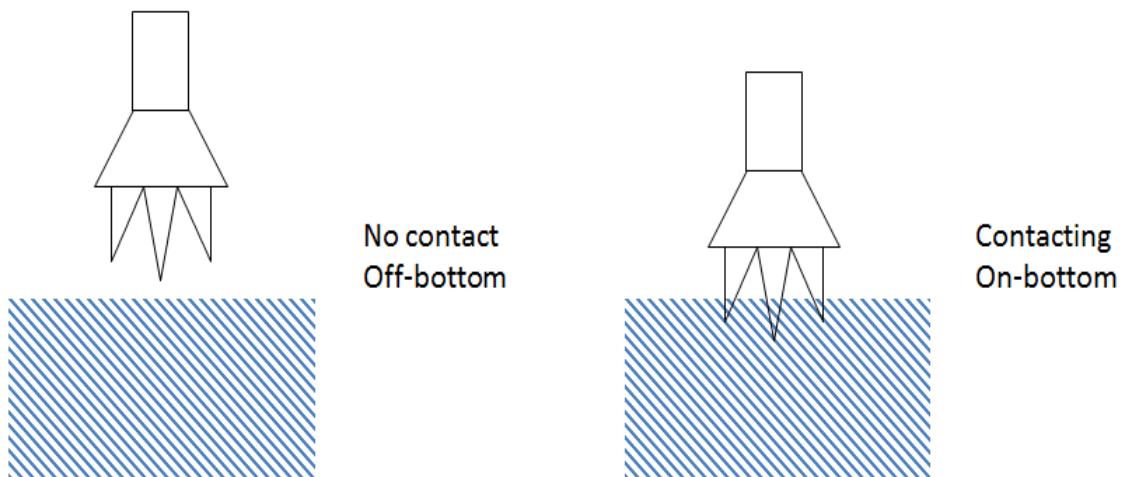


Figure 5.4 Off-bottom and On-bottom Scenarios

Real-time drilling depth data offers an indicator to distinguish the off-bottom data from on-bottom data: when the bit depth is less than the hole depth, the bit is off-bottom, and when the bit depth equals to the hole depth, the bit is on-bottom.

Table 5.2 shows the principle about how we choose calculating point.

Table 5.2 Real-time Drilling Data from 2505.3m to 2505.99m (Akita, Talisman)

Bit Depth (m)	Hole Depth (m)	On Bottom ROP (m/hr)	Hook Load (ton)	WOB (ton)	Rotary RPM (RPM)	Rotary Torque (N.m)	Standpipe Pressure (psi)
2505.3	2505.65	0	60.9	1.2	61	4101.71	22087
2505.62	2505.65	0	58.8	7.2	61	5869.57	22611
2505.65	2505.65	0	55	6	61	5464.29	22886
2505.71	2505.71	5.74	54.7	6.6	61	5736.8	22886
2505.76	2505.76	5.74	54.2	6.9	61	5967.39	22972
2505.83	2505.83	19.75	53.7	7.3	61	6204.97	23166
2505.88	2505.88	19.75	53.4	7.4	61	6135.1	23205
2505.93	2505.93	19.98	53.4	7.6	61	6372.67	23304
2505.99	2505.99	19.98	53.1	7.7	61	6400.62	23278

In Table 5.2, the bit depth equals to the hole depth at 2505.65m, it's the depth at which the drilling status changed from off-bottom to on-bottom, the first on-bottom depth point is 2505.71m.

The data point at 2505.65m, and the points beyond this depth, can be used to calculate the friction factor. Depth 2505.71m or greater can be used to calculate DWOB.

Because the data are 10-second based, the depths for both on-bottom and off-bottom are close. To make the comparison diagrams easier to read, it is assumed that the friction factor remains

the same within each 10m section, until we make a new connection, even though we know there could be slightly different friction factors for every meter drilled.

Following this data choosing principle, 43 depth points are chosen from 2500m to 3844m. The original SWOB at different depths are shown in Table 5.3 and Figure 5.5.

Table 5.3 Depth versus SWOB (Akita, Talisman)

Depth (m)	SWOB (ton)	Depth (m)	SWOB (ton)	Depth (m)	SWOB (ton)	Depth (m)	SWOB (ton)
2520.21	12.3	2825.27	14.6	3139.01	14.9	3495.25	13
2556.28	11.6	2854.26	14.1	3197.42	14.7	3529.68	15
2585.03	12.3	2891.37	15.1	3226.82	13.7	3555.98	14.8
2605.02	12.1	2926.17	13.1	3283.24	13.6	3591.18	15.1
2636.75	14.7	2945.05	14.3	3313.4	14	3616.63	13.3
2669.42	15.2	2983.37	14.8	3340.63	13.8	3643.74	13.9
2685.15	12.5	3002.92	15	3384.49	13.9	3666.28	15.5
2706.6	14.2	3028.61	15.1	3403.4	14.4	3701.11	15.3
2730.19	14.7	3060.01	14.4	3428.19	14	3727.24	14.7
2766.07	14.8	3097.97	14.9	3446.03	14.1	3746.35	15.3
2805.07	14.8	3116.92	15.3	3465.36	14.9		

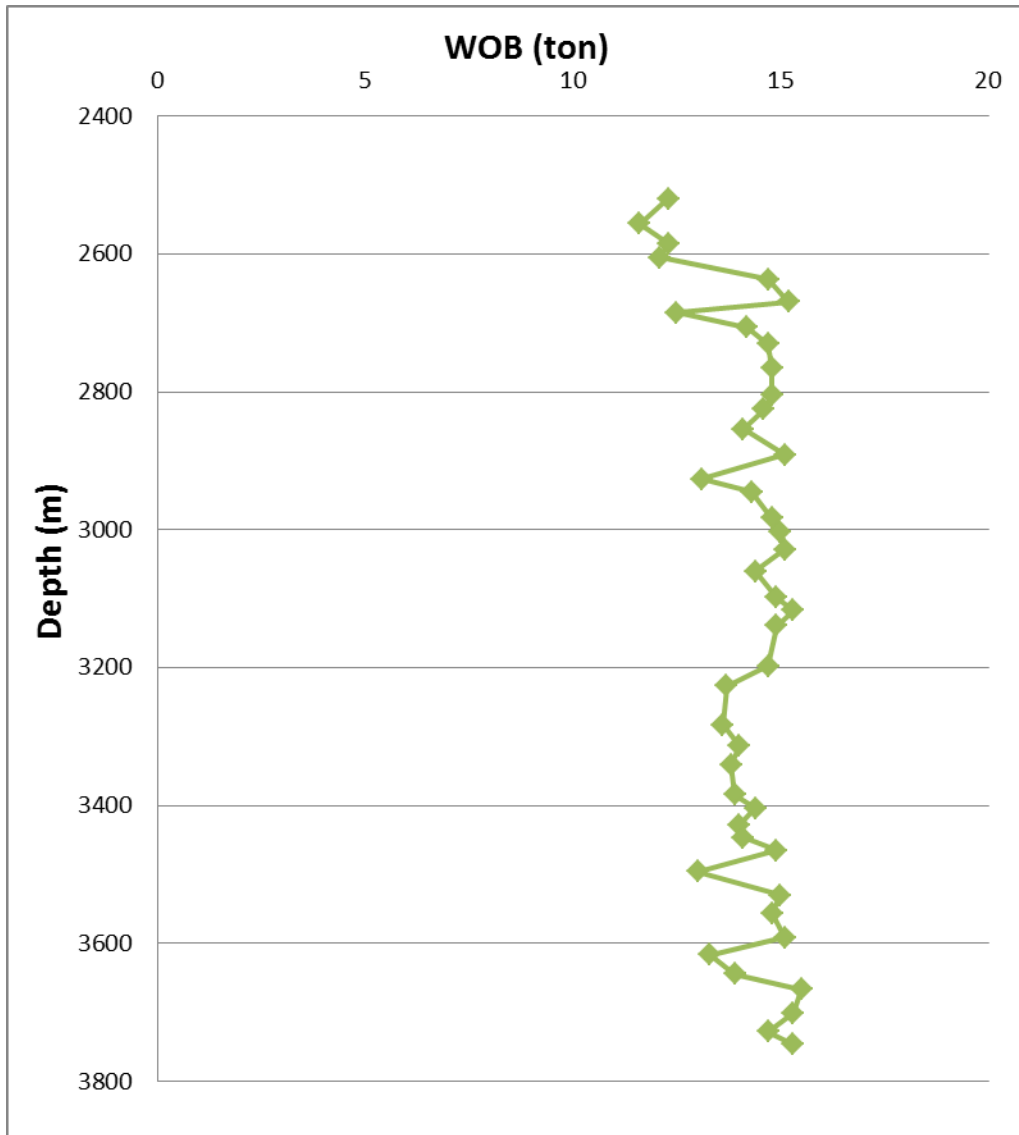


Figure 5.5 SWOB at Different Depth

Figure 5.5 shows the data that can be gathered from the field without using the CoPilot downhole measurement tool. Based on the CoPilot data we found the DWOB is different than the SWOB. Using the data collected with CoPilot measurement tool. The difference between downhole measured data and surface data is compared in Table 5.4 and Figure 5.6:

Table 5.4 Depth Versus SWOB (Akita, Talisman)

Depth (m)	SWOB (ton)	CoPilot DWOB (ton)	Depth (m)	SWOB (ton)	CoPilot DWOB (ton)
2520.21	12.3	10.42	3139.01	14.9	11.57
2556.28	11.6	9.4	3197.42	14.7	11.65
2585.03	12.3	9.6	3226.82	13.7	9.501
2605.02	12.1	8.73	3283.24	13.6	10.33
2636.75	14.7	11.23	3313.4	14	10.5
2669.42	15.2	11.1	3340.63	13.8	10.59
2685.15	12.5	10.1	3384.49	13.9	11.27
2706.6	14.2	11.23	3403.4	14.4	11.3
2730.19	14.7	11.8	3428.19	14	10.48
2766.07	14.8	11.4	3446.03	14.1	10.55
2805.07	14.8	11.92	3465.36	14.9	11.14
2825.27	14.6	11.76	3495.25	13	9.79
2854.26	14.1	11.63	3529.68	15	11.71
2891.37	15.1	11.53	3555.98	14.8	11.54
2926.17	13.1	10.4	3591.18	15.1	11.26
2945.05	14.3	11.98	3616.63	13.3	10.41
2983.37	14.8	12.15	3643.74	13.9	10.77
3002.92	15	12.52	3666.28	15.5	11.62
3028.61	15.1	12	3701.11	15.3	12.51
3060.01	14.4	11.69	3727.24	14.7	11.79
3097.97	14.9	12.17	3746.35	15.3	11.52
3116.92	15.3	12.4			

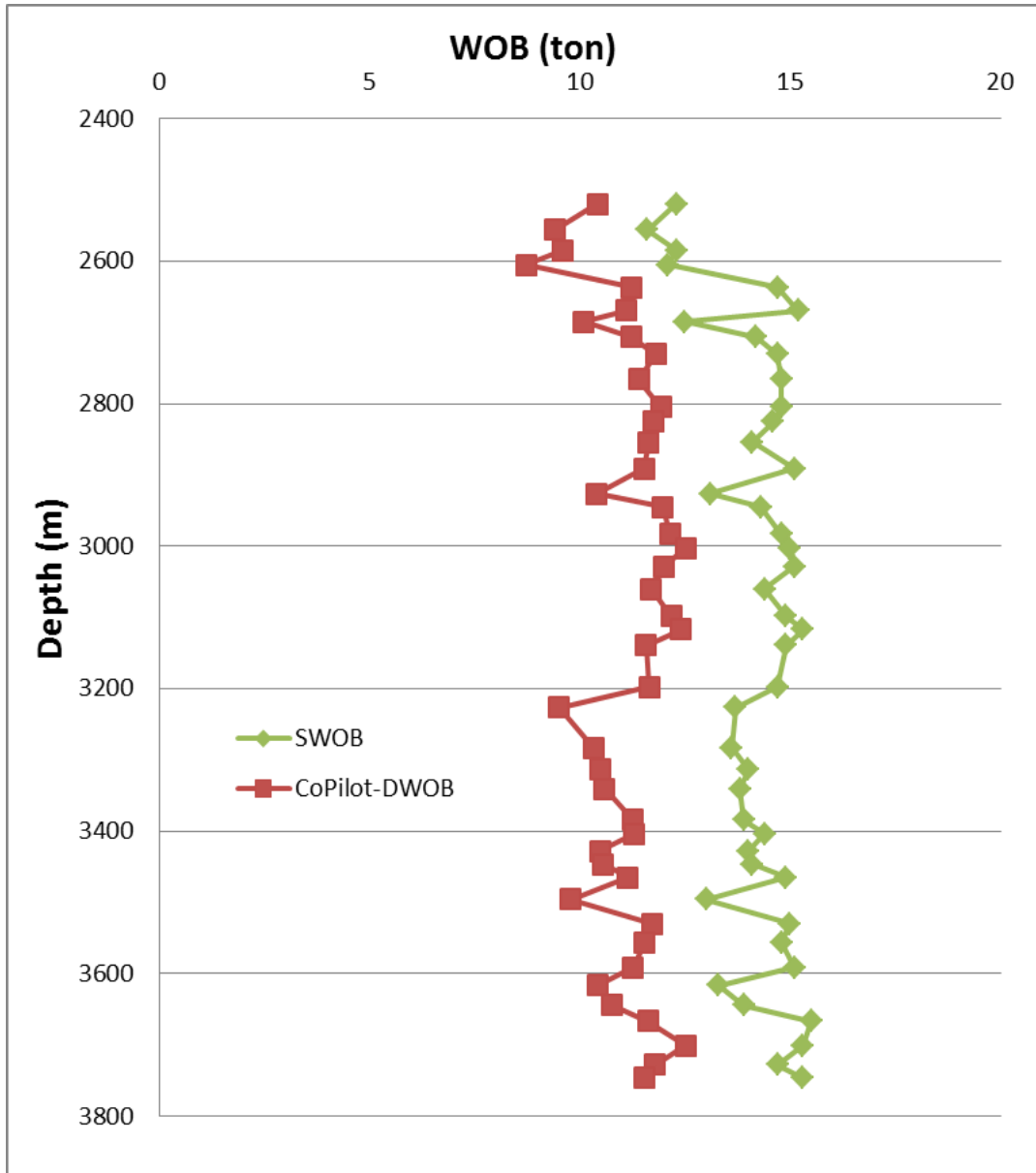


Figure 5.6 Comparison between CoPilot-DWOB and SWOB

Figure 5.6 shows a gap between CoPilot-DWOB and SWOB, with the gap values varying from 1.88 to 4.199 ton.

The WOB cannot be calibrated simply by adding or reducing a fixed value from SWOB. Therefore, Analytical Model and FEM are used to calculate WOB, and compared to determine which method produces the most precise results.

5.2 Calculation with Analytical Model

As introduced in Chapter Three, the Analytical Model offers the fastest DWOB calculation and Torque and Drag analysis, with a normal calculation time of 2 seconds for each point. This fast-computing feature makes it possible to be eventually applied in the field for real-time drilling analysis and real-time drilling monitoring.

For the depth points from 2500m to 2800m:

Firstly, we calculate the friction factors using off-bottom data producing the friction factors in Table 5.5:

Table 5.5 Friction Factor from 2500m to 2800m

Depth (m)	mu-Analytical
2520.21	0.141
2556.28	0.116
2585.03	0.133
2605.02	0.145
2636.75	0.118
2669.42	0.132
2685.15	0.125
2706.6	0.1221
2730.19	0.138
2766.07	0.131

To better outline the distribution of friction factors, their relationships are plotted in Figure 5.7.

It shows the friction factors are all between 0.1 and 0.15. The average value of the friction factors is 0.13.

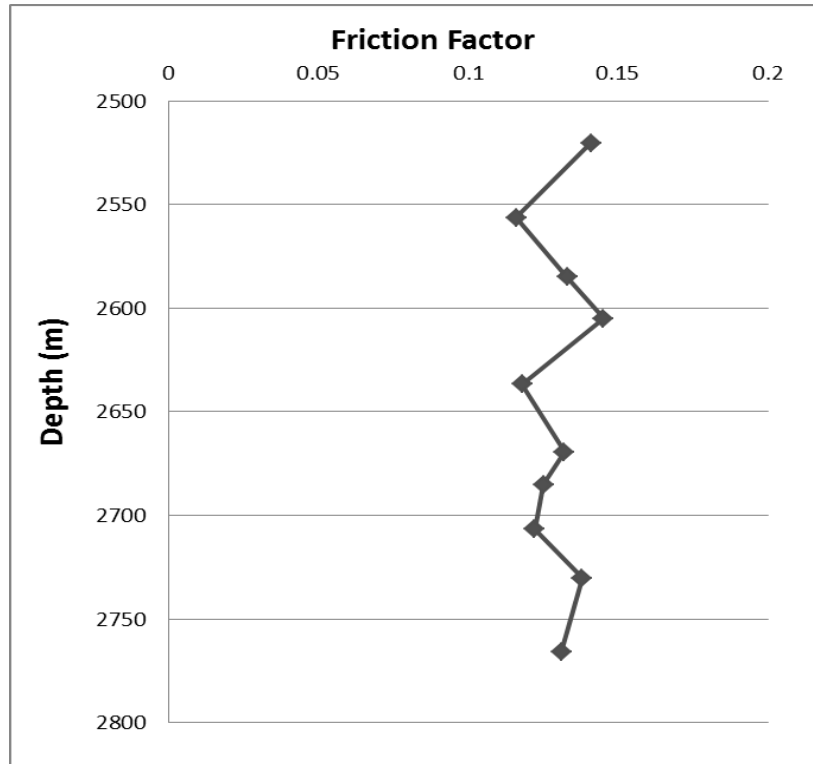


Figure 5.7 Friction Factor from 2500m to 2800m

After calculating the friction factors, they can be carried used to calculate DWOB, the comparison between Analytical-DWOB and CoPilot-DWOB are shown in Table 5.6 and Figure 5.8:

Table 5.6 CoPilot-DWOB and Analytical-DWOB from 2500m to 2800m

Depth (m)	CoPilot-DWOB (ton)	Analytical-DWOB (ton)
2520.21	10.42	9.8
2556.28	9.4	9.58
2585.03	9.6	9.46
2605.02	8.73	8.98
2636.75	11.23	10.82
2669.42	11.1	10.74
2685.15	10.1	9.7
2706.6	11.23	11.1
2730.19	11.8	11.02
2766.07	11.4	10.96

Figure 5.8 shows the Analytical-DWOB is a close match with CoPilot-DWOB from 2500m to 2800m.

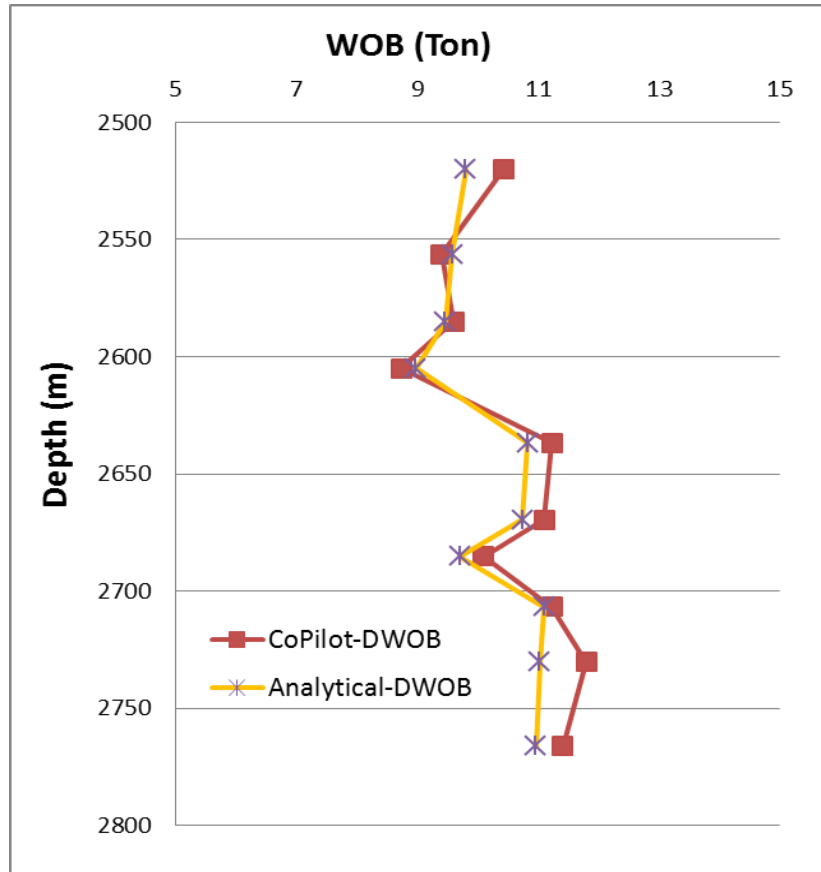


Figure 5.8 Comparison between CoPilot-DWOB and Analytical-DWOB from 2500m to 2800m

For the depth points from 2800m to 3100m:

With Off-bottom data, friction factors can be calculated, as shown in Table 5.7 and Figure 5.9:

Table 5.7 Friction Factor from 2800m to 3100m

Depth (m)	mu-Analytical (ton)
2805.07	0.106
2825.27	0.117
2854.26	0.136
2891.37	0.12
2926.17	0.113
2945.05	0.108
2983.37	0.117
3002.92	0.092
3028.61	0.092
3060.01	0.08
3097.97	0.09

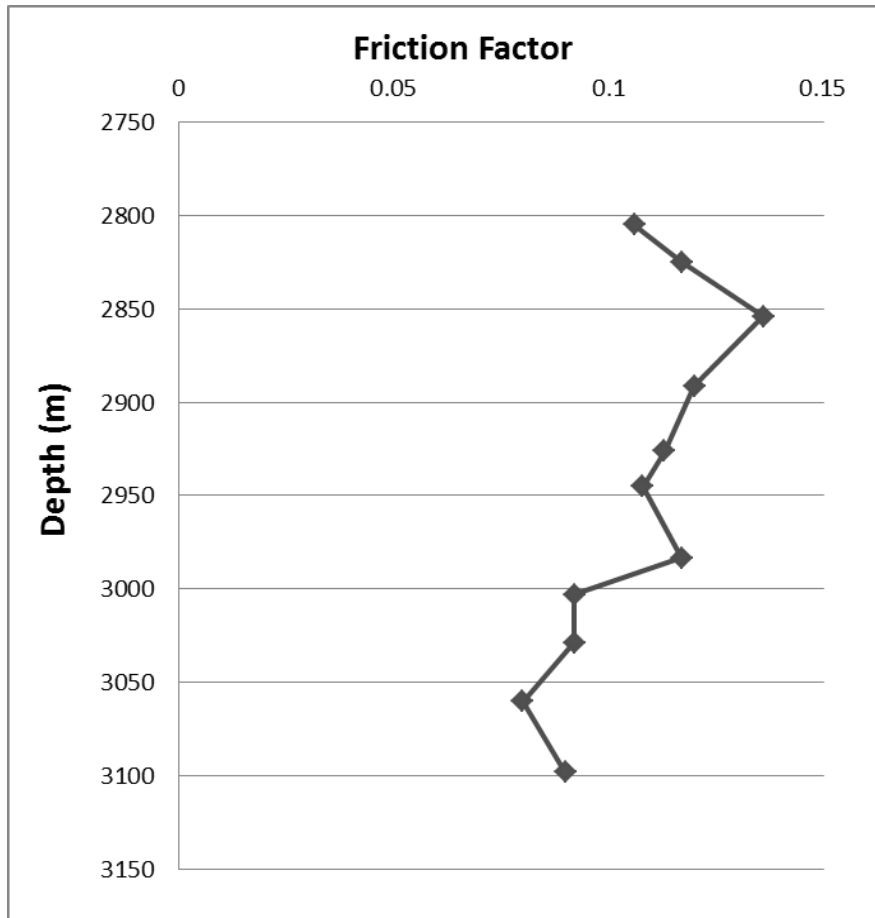


Figure 5.9 Friction Factor from 2800m to 3100m

DWOB can be calculated based on the friction factors in Table 5.7. The results are shown in Table 5.8. The relationship between them is plotted in Figure 5.10.

Table 5.8 CoPilot-DWOB and Analytical-DWOB from 2800m to 3100m

Depth (m)	CoPilot-DWOB (ton)	Analytical-DWOB (ton)
2805.07	11.92	11.68
2825.27	11.76	11.04
2854.26	11.63	10.64
2891.37	11.53	11.2
2926.17	10.4	9.98
2945.05	11.98	11.24
2983.37	12.15	11.32
3002.92	12.52	11.54
3028.61	12	11.68
3060.01	11.69	11.08
3097.97	12.17	11.68

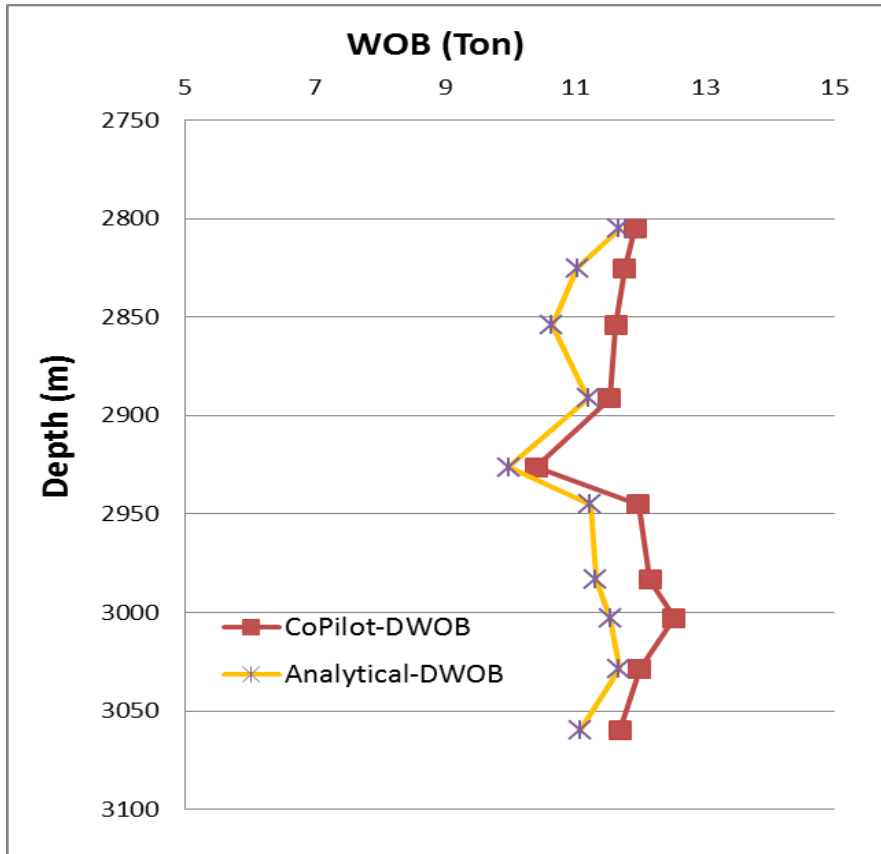


Figure 5.10 Comparison between CoPilot-DWOB and Analytical-DWOB from 2800m to 3100m

For the depth points from 3100m to 3450m:

With Off-bottom data, friction factors can be calculated, as shown in Table 5.9 and Figure 5.11:

Table 5.9 Friction Factor from 3100m to 3450m

Depth (m)	mu-Analytical
3116.92	0.09
3139.01	0.106
3197.42	0.114
3226.82	0.125
3283.24	0.118
3313.4	0.122
3340.63	0.12
3384.49	0.117
3403.4	0.113
3428.19	0.115
3446.03	0.105

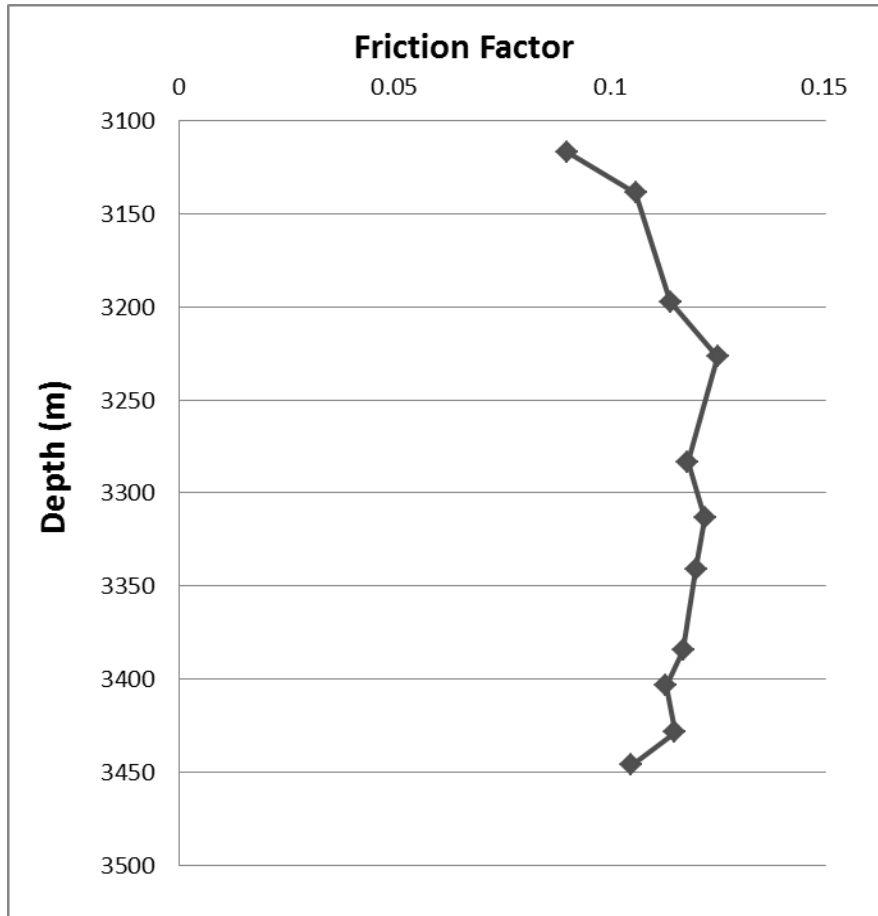


Figure 5.11 Friction Factor from 3100m to 3450m

DWOB can be calculated based on the friction factors in Table 5.9. The results are shown in Table 5.10. The relationship between them is plotted in Figure 5.12.

Table 5.10 CoPilot-DWOB and Analytical-DWOB from 3100m to 3450m

Depth (m)	CoPilot-DWOB (ton)	Analytical-DWOB (ton)
3116.92	12.4	11.76
3139.01	11.57	11.02
3197.42	11.65	10.64
3226.82	9.501	9.54
3283.24	10.33	9.86
3313.4	10.5	10.13
3340.63	10.59	10.06
3384.49	11.27	10.64
3403.4	11.3	11.02
3428.19	10.48	10.52
3446.03	10.55	10.34

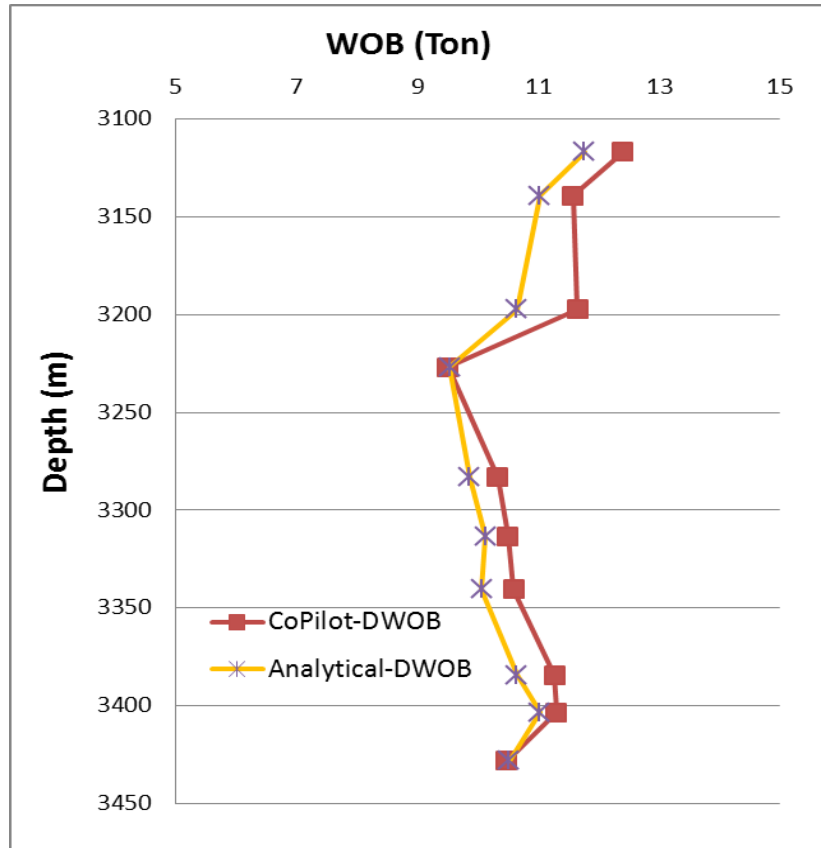


Figure 5.12 Comparison between CoPilot-DWOB and Analytical-DWOB from 3100m to 3450m

For the depth points from 3450m to 3750m:

With Off-bottom data, friction factors can be calculated, as shown in Table 5.11 and Figure 5.13:

Table 5.11 Friction Factor from 3450m to 3750m

Depth (m)	mu-Analytical
3465.36	0.108
3495.25	0.115
3529.68	0.099
3555.98	0.095
3591.18	0.109
3616.63	0.112
3643.74	0.106
3666.28	0.119
3701.11	0.101
3727.24	0.115
3746.35	0.114

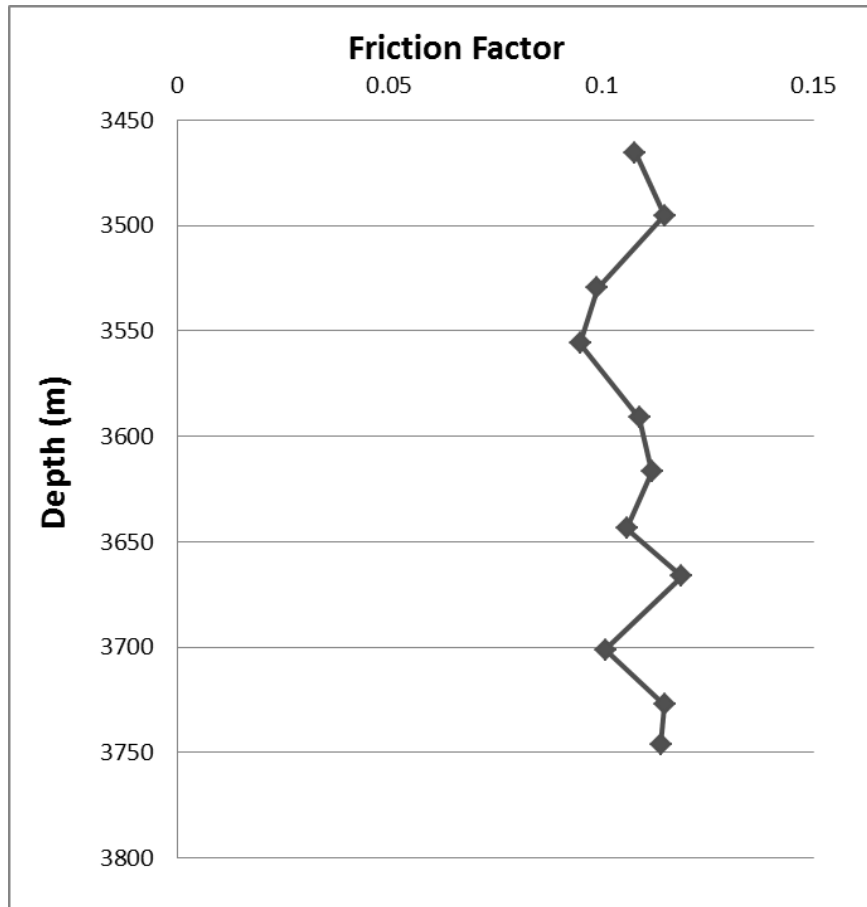


Figure 5.13 Friction Factor from 3450m to 3750m

DWOB can be calculated based on the friction factors in Table 5.11. The results are shown in Table 5.12. The relationship between them is plotted in Figure 5.14.

Table 5.12 CoPilot-DWOB and Analytical-DWOB from 3450m to 3750m

Depth (m)	CoPilot-DWOB (ton)	Analytical-DWOB (ton)
3465.36	11.14	10.88
3495.25	9.79	9.05
3529.68	11.71	10.94
3555.98	11.54	11.22
3591.18	11.26	10.92
3616.63	10.41	9.68
3643.74	10.77	10.18
3666.28	11.62	10.68
3701.11	12.51	11.74
3727.24	11.79	10.78
3746.35	11.52	11.02

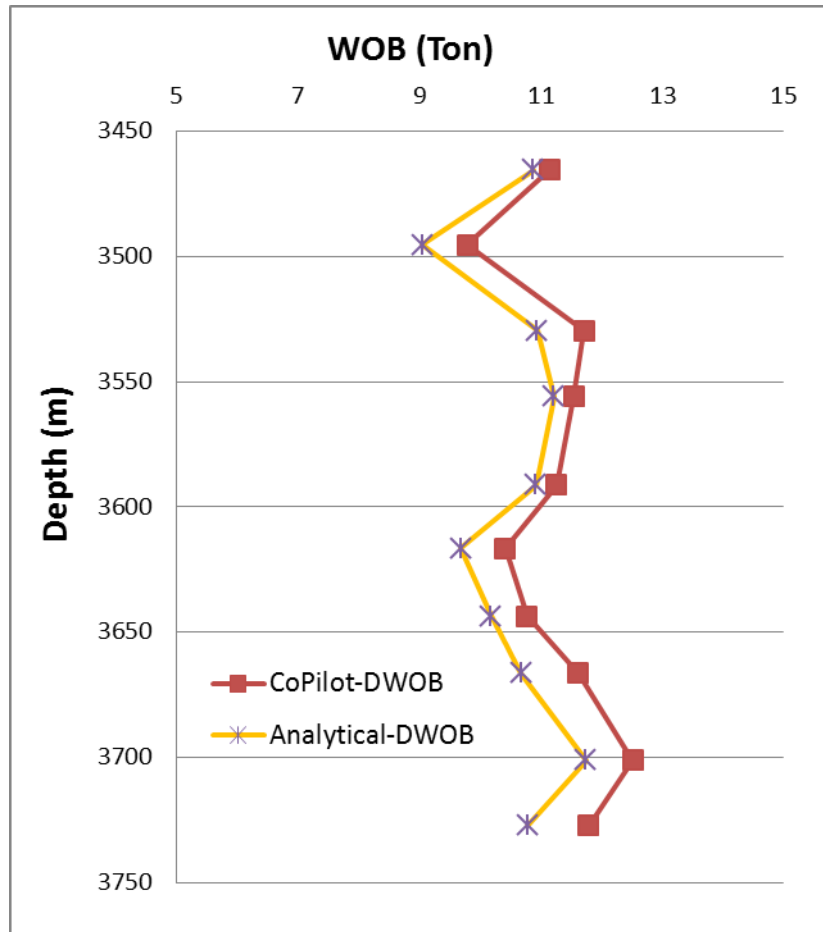


Figure 5.14 Comparison between CoPilot-DWOB and Analytical-DWOB from 3450m to 3750m

All experimental results based on the Analytical Model have now been calculated. Details will be further examined in the discussion section.

5.3 Calculation with FEM

To compare the results retrieved from both Analytical Model and FEM, the same structure will now be used to analyze data with FEM.

Theoretically, FEM can provide more precise results than the Analytical Model, since the stiffness of the string is taken into consideration. However, FEM is time-consuming because the results will not be stable until 2000 iterations (this calculation contains the information for the entire well path, not just for one specific depth point). For a given friction factor, it takes approximately 4 minutes to return a calculated hookload (with a quad-core Macbook laptop), however, in this

simulation, we have to increase the friction factor from 0 to one value when the “calculated hookload” equals to the measured hookload on surface. In that situation, the process takes hours to calculate DWOB.

Even with a “Speedup Algorithm”, the calculation must be done at least 15 times to get the friction factor for one depth point, which totals 60 minutes for each depth point. The same concept is applied for the DWOB calculation.

The calculating procedure is shown as Figure 5.15 (for instance, at depth 2705.86m):

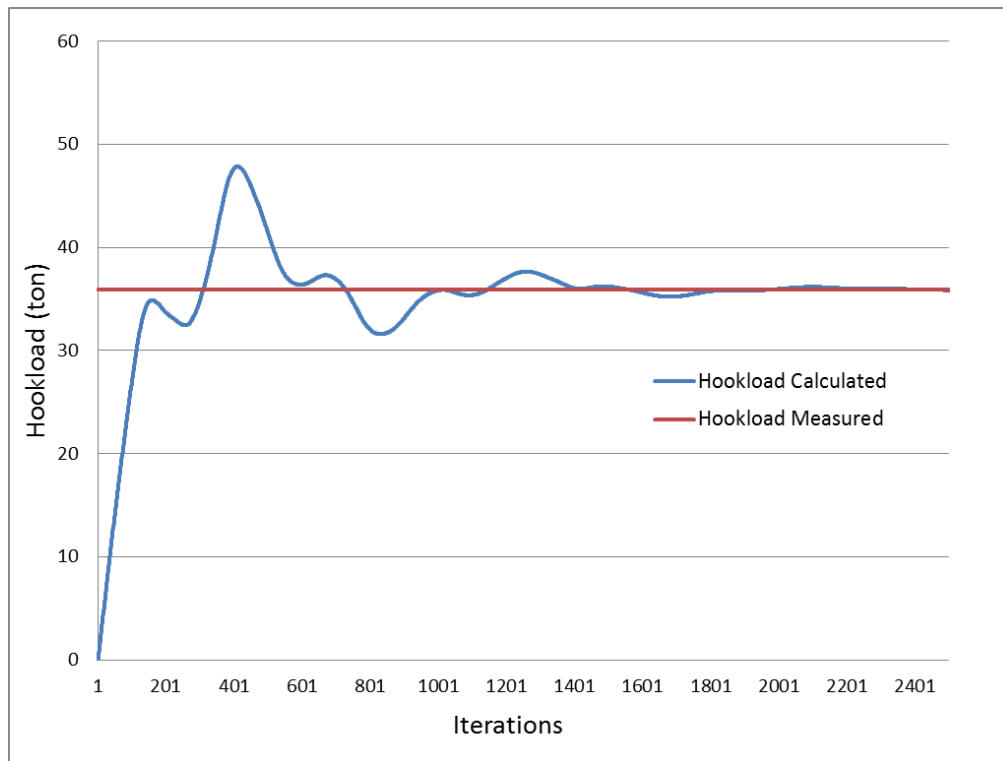


Figure 5.15 Iteration Procedures for Friction Factor Calculation

For the depth points from 2500m to 2800m:

Using Off-bottom data, friction factors can be calculated, as shown in Table 5.13 and Figure 5.16.

Table 5.13 Friction Factor from 2500m to 2800m

Depth (m)	mu-FEM
2520.21	0.253
2556.28	0.254
2585.03	0.253
2605.02	0.28
2636.75	0.272
2669.42	0.258
2685.15	0.25
2706.6	0.26
2730.19	0.265
2766.07	0.248

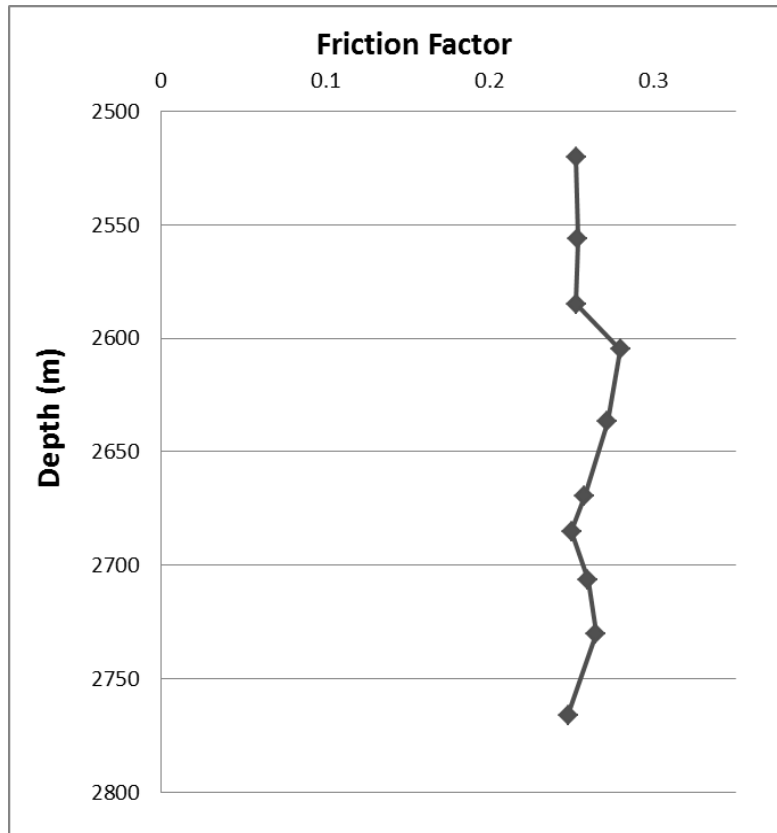


Figure 5.16 Friction Factor from 2500m to 2800m

Table 5.13 and Figure 5.16 show the friction factors are generally greater than the results from the Analytical Model. Details will be discussed in the following section.

Using these friction factors, the DWOB can be calculated with FEM. The results are shown in Table 5.14 and Figure 5.17.

Table 5.14 CoPilot-DWOB and FEM-DWOB from 2500m to 2800m

Depth (m)	CoPilot-DWOB (ton)	FEM-DWOB (ton)
2520.21	10.42	10.75
2556.28	9.4	9.91
2585.03	9.6	9.90
2605.02	8.73	9.22
2636.75	11.23	11.47
2669.42	11.1	11.57
2685.15	10.1	10.21
2706.6	11.23	11.48
2730.19	11.8	11.62
2766.07	11.4	11.42

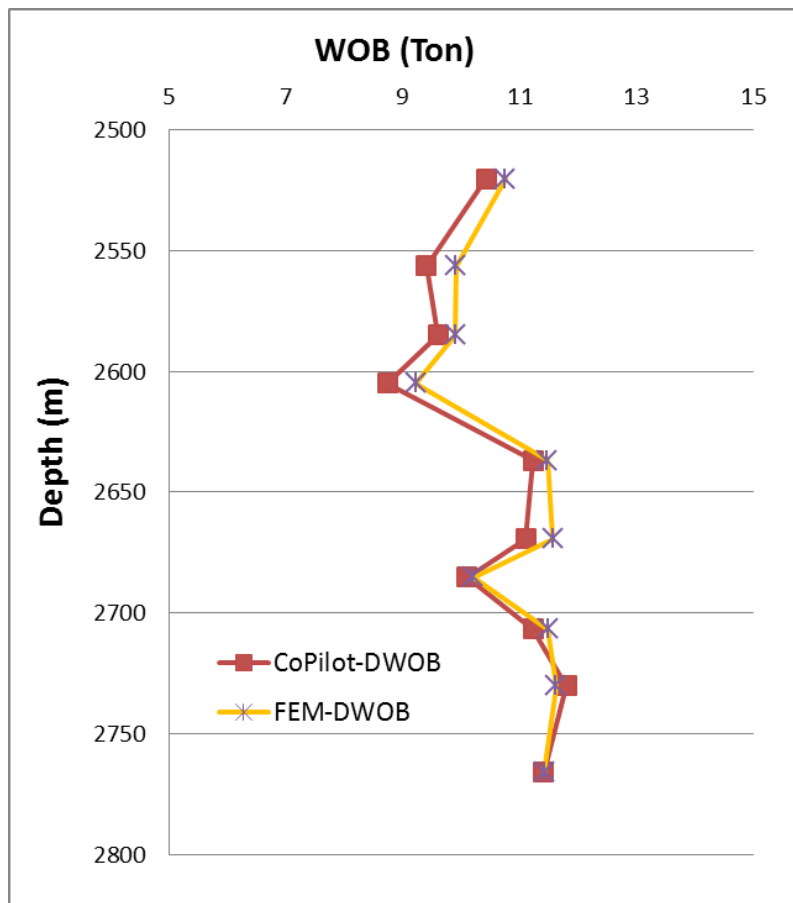


Figure 5.17 Comparison between CoPilot-DWOB and FEM-DWOB from 2500m to 2800m

For the depth points from 2800m to 3100m:

Using Off-bottom data, friction factors can be calculated, as shown in Table 5.15 and Figure 5.18.

Table 5.15 Friction Factor from 2800m to 3100m

Depth (m)	mu-FEM
2805.07	0.225
2825.27	0.222
2854.26	0.216
2891.37	0.231
2926.17	0.29
2945.05	0.19
2983.37	0.2
3002.92	0.152
3028.61	0.171
3060.01	0.17
3097.97	0.166

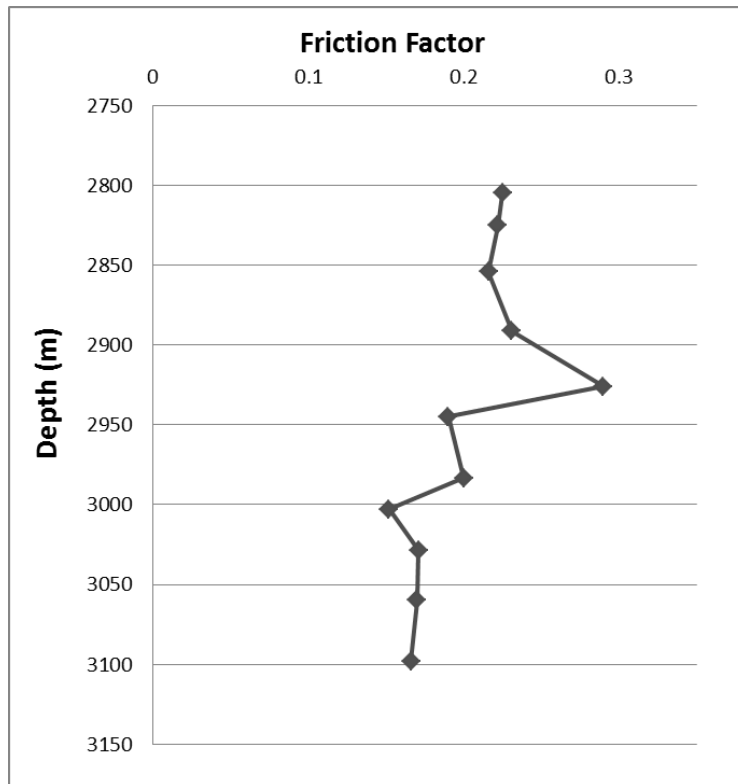


Figure 5.18 Friction Factor from 2800m to 3100m

Using these friction factors, the DWOB can be calculated with FEM. The results are shown in Table 5.16 and Figure 5.19.

Table 5.16 CoPilot-DWOB and FEM-DWOB from 2800m to 3100m

Depth (m)	CoPilot-DWOB (ton)	FEM-DWOB (ton)
2805.07	11.92	11.69
2825.27	11.76	11.30
2854.26	11.63	11.06
2891.37	11.53	11.31
2926.17	10.4	10.97
2945.05	11.98	11.16
2983.37	12.15	12.65
3002.92	12.52	11.81
3028.61	12	11.96
3060.01	11.69	11.40
3097.97	12.17	11.98

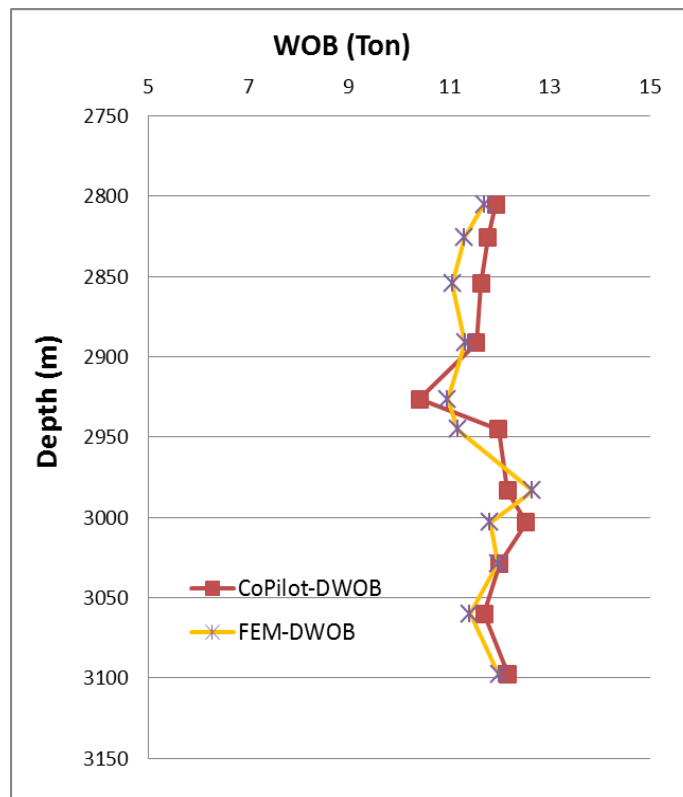


Figure 5.19 Comparison between CoPilot-DWOB and FEM-DWOB from 2800m to 3100m

For the depth points from 3100m to 3450m:

Using Off-bottom data, friction factors can be calculated, as shown in Table 5.17 and Figure 5.20.

Table 5.17 Friction Factor from 3100m to 3450m

Depth (m)	mu-FEM
3116.92	0.164
3139.01	0.18
3197.42	0.213
3226.82	0.18
3283.24	0.201
3313.4	0.198
3340.63	0.192
3384.49	0.2
3403.4	0.195
3428.19	0.2
3446.03	0.193

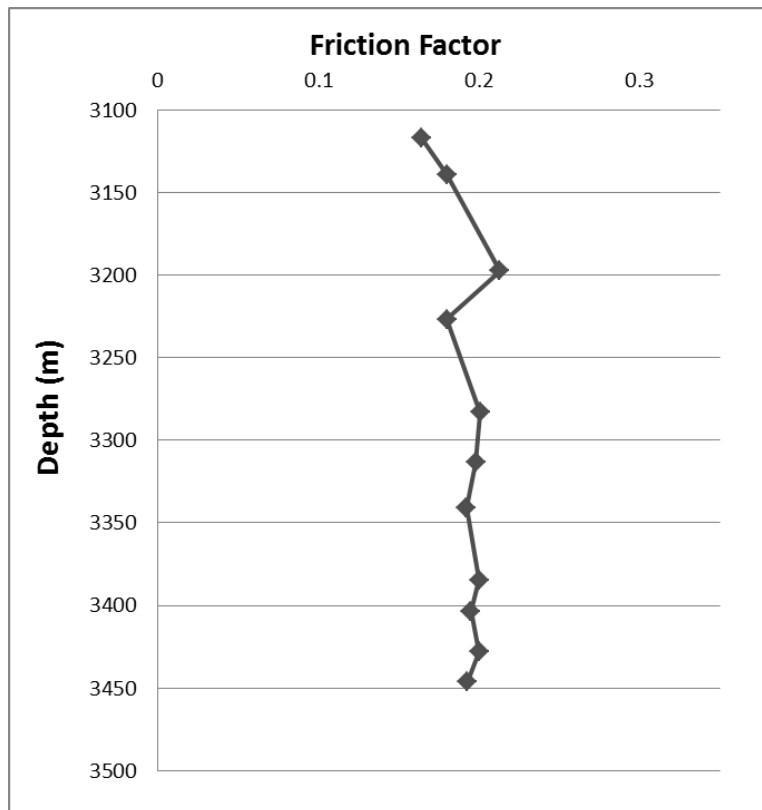


Figure 5.20 Friction Factor from 3100m to 3450m

Using these friction factors, the DWOB can be calculated with FEM. The results are shown in Table 5.18 and Figure 5.21.

Table 5.18 CoPilot-DWOB and FEM-DWOB from 3100m to 3450m

Depth (m)	CoPilot-DWOB (ton)	FEM-DWOB (ton)
3116.92	12.4	11.77
3139.01	11.57	11.04
3197.42	11.65	11.11
3226.82	9.501	9.50
3283.24	10.33	10.14
3313.4	10.5	10.24
3340.63	10.59	10.35
3384.49	11.27	10.76
3403.4	11.3	11.28
3428.19	10.48	10.55
3446.03	10.55	10.45

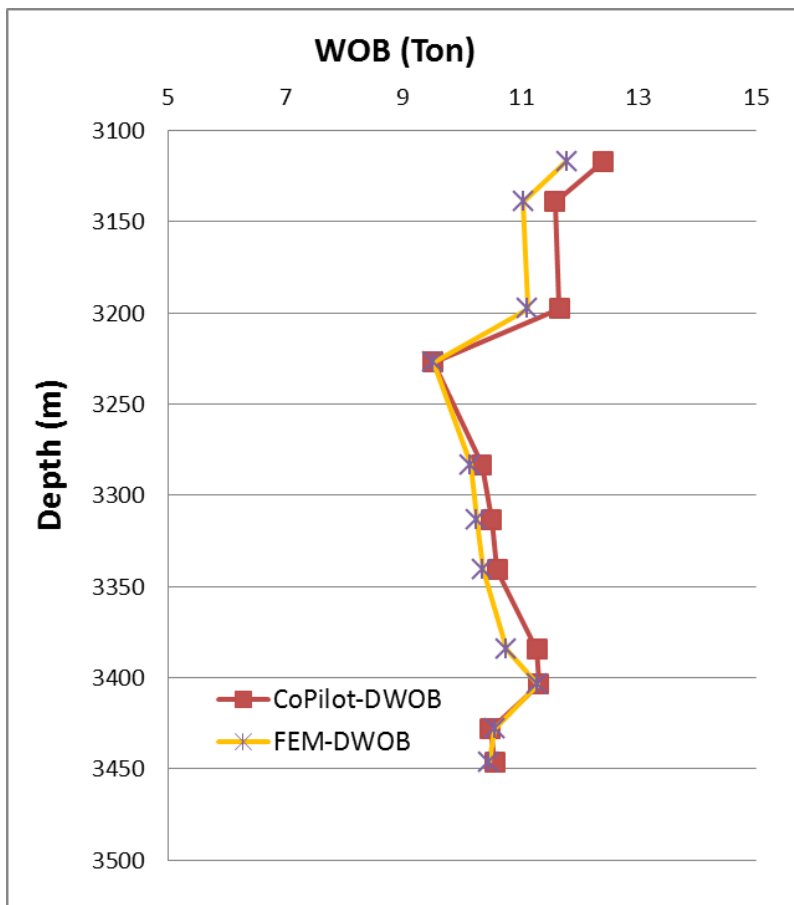


Figure 5.21 Comparison between CoPilot-DWOB and FEM-DWOB from 3100m to 3450m

For the depth points from 3450m to 3750m:

Using Off-bottom data, friction factors can be calculated, as shown in Table 5.19 and Figure 5.22.

Table 5.19 Friction Factor from 3450m to 3750m

Depth (m)	mu-FEM
3465.36	0.192
3495.25	0.18
3529.68	0.136
3555.98	0.152
3591.18	0.16
3616.63	0.159
3643.74	0.15
3666.28	0.168
3701.11	0.157
3727.24	0.175
3746.35	0.177

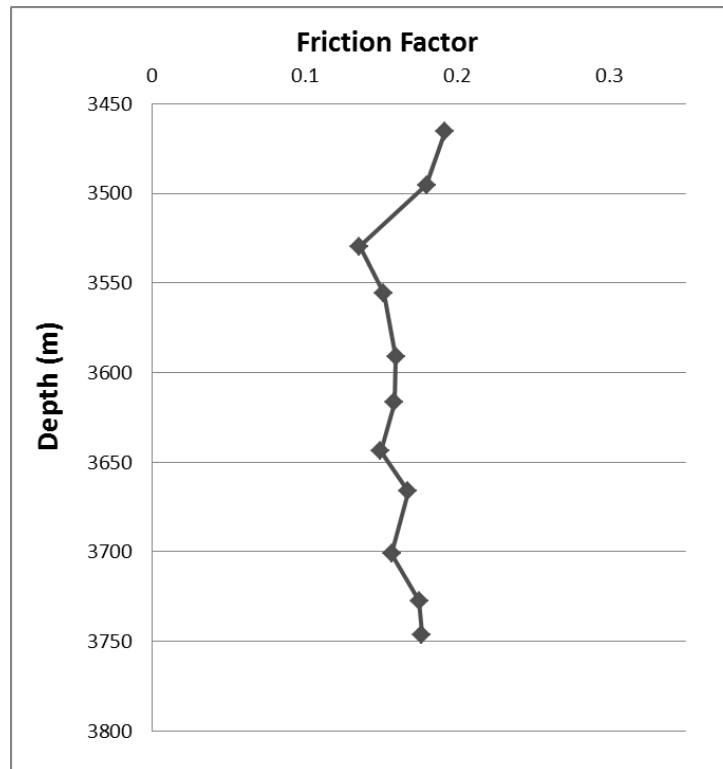


Figure 5.22 Friction Factor from 3450m to 3750m

Using these friction factors, the DWOB can be calculated with FEM. The results are shown in Table 5.20 and Figure 5.23.

Table 5.20 CoPilot-DWOB and FEM-DWOB from 3450m to 3750m

Depth (m)	CoPilot-DWOB (ton)	FEM-DWOB (ton)
3465.36	11.14	11.33
3495.25	9.79	9.56
3529.68	11.71	11.06
3555.98	11.54	11.81
3591.18	11.26	10.75
3616.63	10.41	10.11
3643.74	10.77	10.15
3666.28	11.62	11.89
3701.11	12.51	11.94
3727.24	11.79	12.38
3746.35	11.52	11.86

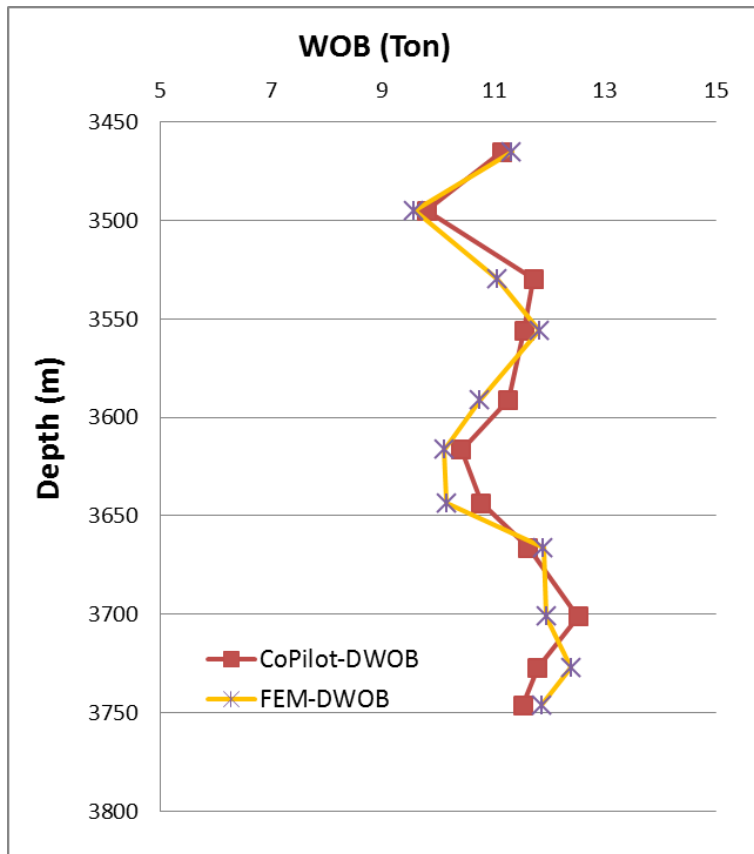


Figure 5.23 Comparison between CoPilot-DWOB and FEM-DWOB from 3450m to 3750m

5.3 Discussion

In section 5.1 and 5.2, the DWOB was calculated based on the Analytical Model and FEM. In this section, the efficacy of the methods will be compared and the meaning of the results will be explored.

5.3.1 Friction Factors

Friction factors are different from each method because both methods are based on different assumptions.

The friction factor used in this thesis does not represent the friction coefficient. The friction coefficient is defined as the force resisting the relative motion of solid surface for the case of drilling mechanics. However in this research, the friction factors includes things more than just friction. Some forces that cannot be calculated or considered are counted as contributions to the friction factor. For example, in Analytical Model, the stiffness of drillstrings are not considered, therefore, the force caused by stiffness will be regarded as a part of the friction factor.

The friction factors for both methods are plotted in Figure 5.24.

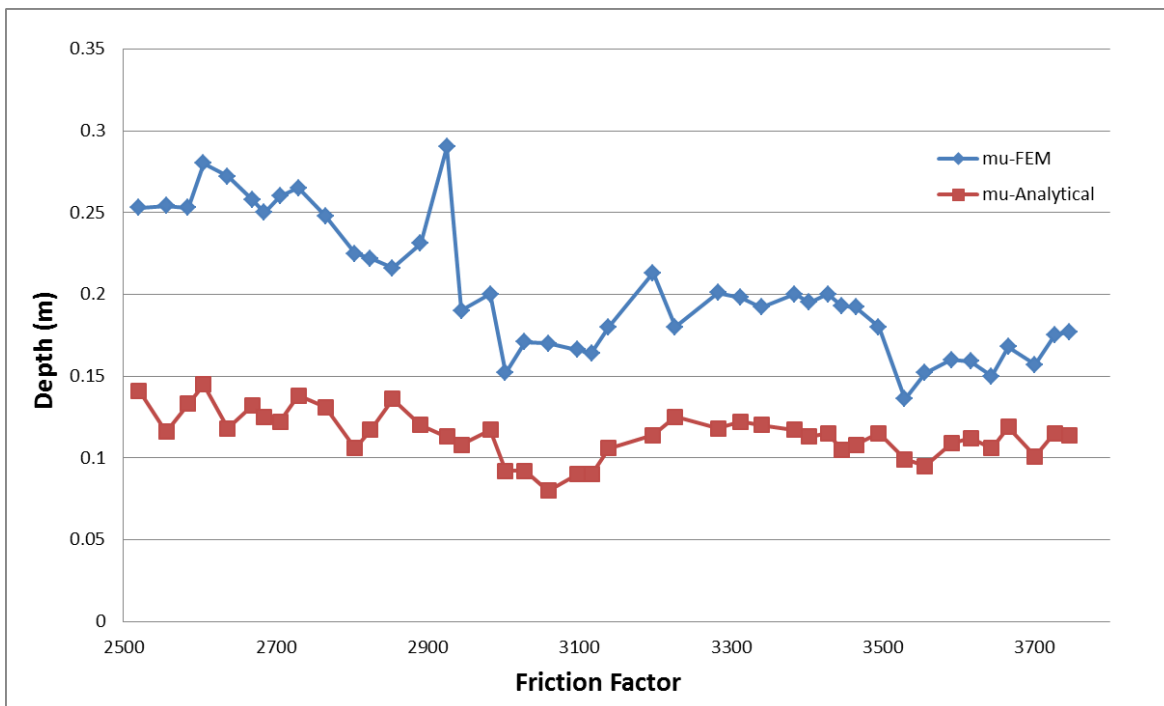


Figure 5.24 Comparison of Friction Factor for Analytical Model and FEM

The friction factors for both methods are plotted in Figure 5.24, which shows comparatively inconsistent friction factors.

Meanwhile, the friction factors from FEM are greater than values from the Analytical Model. As introduced that in the Analytical Model, the entire drillstring is assumed as a soft string meaning the entire horizontal drillstring is contacting the wellbore, called “line contact”, and the stiffness is not considered. Anything that caused extra force will be regarded as cause by the friction factor, therefore, a small friction factor can cause a big drag force; while in FEM, the contact is “point contact”. In the FEM the deformation of sting, stiffness and damping are considered separate from the friction factor, therefore, in order to generate the same extra force, a higher friction factor needs to be applied.

5.3.2 Weight on Bit

Figure 5.25 compares the DWOB calculated by both methods from 2500m to 2800m:

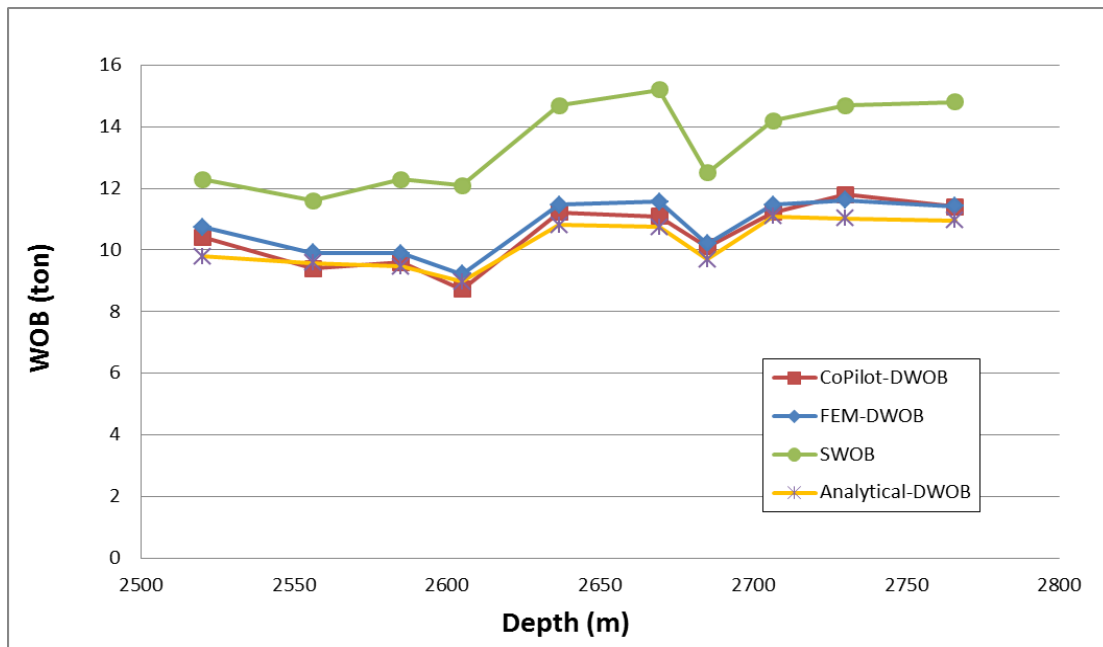


Figure 5.25 WOB Comparison from 2500m to 2800m

From 2500m to 2800m, both methods closely match the measured data.

A comparison from 2800m to 3100m is shown in Figure 5.26:

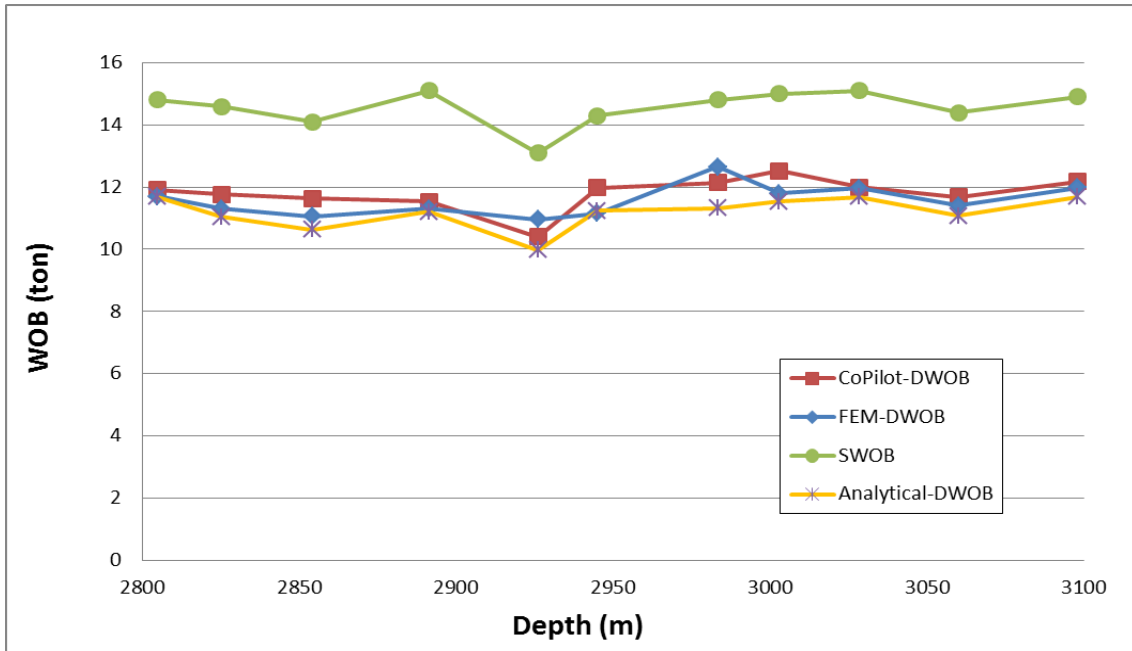


Figure 5.26 WOB Comparison from 2800m to 3100m

In this section, the Analytical Model shows a good match with measured data, but the FEM shows a better match.

From 3100m to 3450m, the comparison is shown in Figure 5.27:

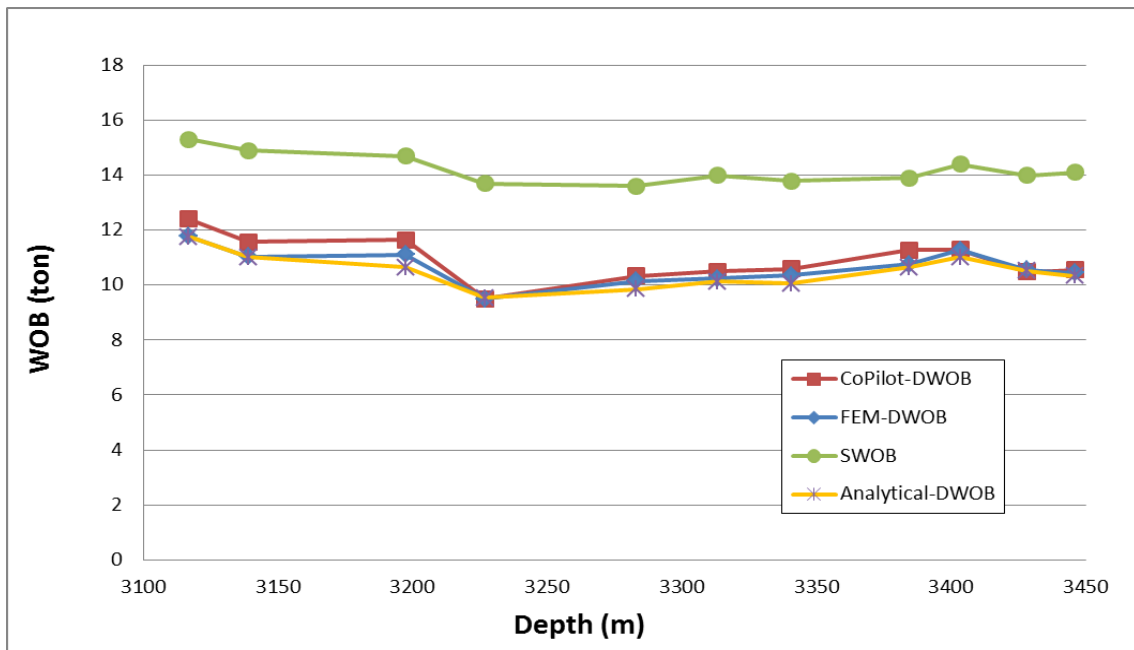


Figure 5.27 WOB Comparison from 3100m to 3450m

In this section, both the Analytical Model and FEM show slightly lower WOB than measured data. The gap between CoPilot-DWOB and Analytical-DWOB is larger compared to the gap between CoPilot-DWOB and FEM-DWOB, which means FEM provides a better match.

From 3450m to 3800m, the comparison is shown in Figure 5.28:

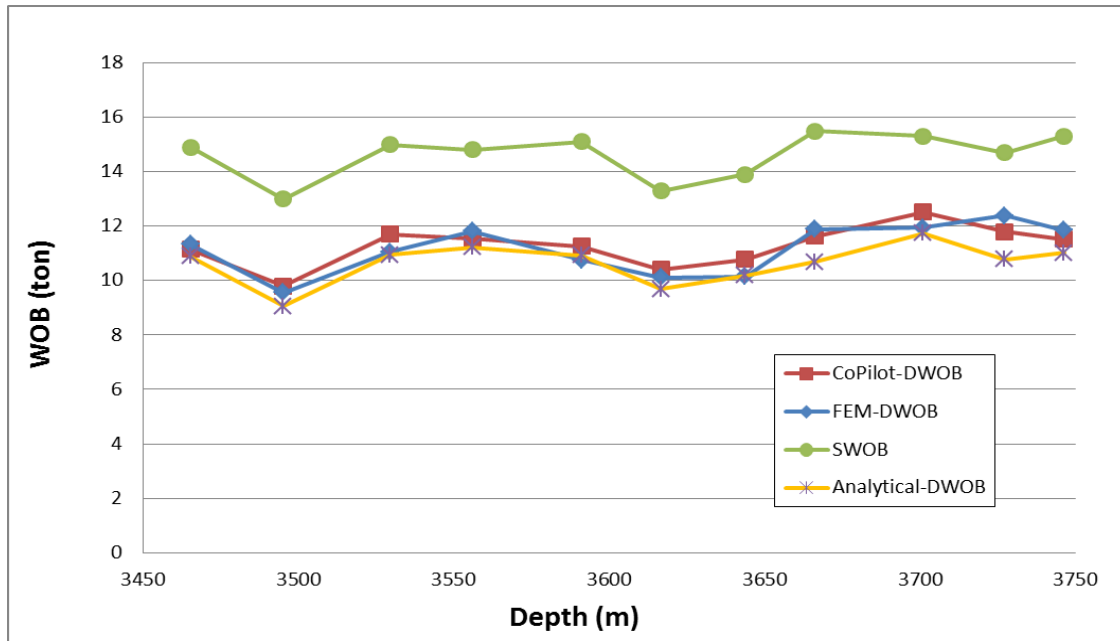


Figure 5.28 WOB Comparison from 3450m to 3800m

In this section, Analytical-DWOB shows a good match with CoPilot-DWOB and FEM-DWOB shows a better match with CoPilot-DWOB.

FEM-DWOB shows a better match with CoPilot-DWOB for all four sections making it a more accurate method to predict real DWOB. It's time consuming process using common computer hardware, but using industrial-grade processing equipment and improved computing algorithms will help to reduce the computing time. Eventually, one hour of computing time can be reduced to 1 min or even 3 seconds.

The Analytical Model is a much faster way to predict DWOB, with the response time being short enough for real-time calculation. However, because stiffness is not considered, the Analytical Model may not provide a precise enough prediction for more complicated well trajectories.

Figure 5.29 shows a complete WOB comparison from 2500m to 3800m.

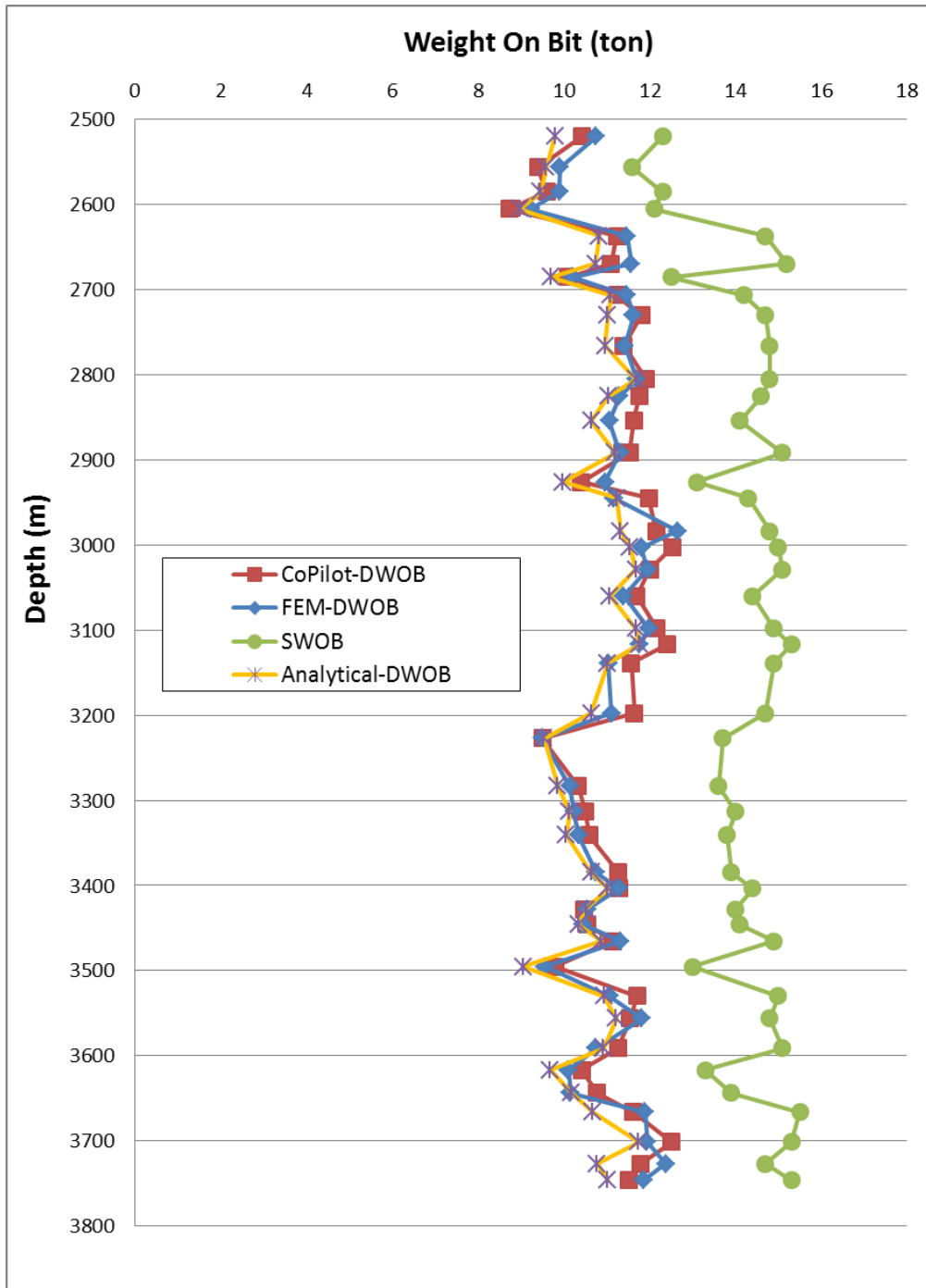


Figure 5.29 WOB Comparison for Entire Well Path

The average variation ratio for both methods were calculated using the following formulas:

$$\text{Variation Ratio} = 1 - \frac{|\text{Analytical-DWOB} - \text{CoPilot-DWOB}|}{|\text{SWOB} - \text{CoPilot-DWOB}|}$$

$$\text{Variation Ratio} = 1 - \frac{|\text{FEM-DWOB} - \text{CoPilot-DWOB}|}{|\text{SWOB} - \text{CoPilot-DWOB}|}$$

The variation ratio shows how much the original gap between real DWOB and SWOB has been reduced.

From 2500m to 2800m,

Analytical Model Average Variation Ratio = 86%

FEM Average Variation Ratio = 90%

From 2800m to 3100m,

Analytical Model Average Variation Ratio = 77%

FEM Average Variation Ratio = 84%

From 3100m to 3450m,

Analytical Model Average Variation Ratio = 86%

FEM Average Variation Ratio = 91%

From 3450m to 3750m,

Analytical Model Average Variation Ratio = 80%

FEM Average Variation Ratio = 87%

The same results as the results through physical observation of Figure 5.25 5.26 5.27 and 5.28 are obtained. FEM-DWOB shows better match with CoPilot-DWOB. We can also see that for the sections from 2500m to 2800m, 3100m to 3450m and 3450m to 3750m, the average variation ratio (VR) for both methods is above 80%, the Analytical Model VR is up to 86% and the VR for FEM is up to 91%. From 2800m to 3100m, both methods show lower variation ratio: 77% and 84%. For the entire well path, the total variation ratio for analytical model and FEM are: 82% and 88% respectively.

Chapter 6 : CONCLUSIONS AND RECOMMENDATIONS

The conclusions and recommendations in this thesis can be summarized as:

- Horizontal well drilling technology can greatly benefits the exploitation and recovery of unconventional resources in North America.
- DWOB is a critical parameter for horizontal well drilling monitoring, prediction of drilling bit life and rate of penetration (ROP) control.
- A 3D analytical drillstring model is programmed and in this model the entire drillstring is regarded as a soft string without considering stiffness. In this method, two scenarios including both straight section and curved section are considered.
- A Finite Element Method (FEM) is introduced and the model for drillstring mechanics analysis is programmed. A 3D beam structure is chosen as the basic element and stiffness of each beam element is considered.
- It takes approximately one hour for FEM to calculate the friction factor and DWOB respectively, which makes FEM a time-consuming method. It cannot be used for real-time drilling monitoring, but in the future with faster industrial-grade computer, it could replace Analytical Model for field application.
- It takes approximately 5 seconds for the Analytical Model to calculate friction factor and 1 second to calculate DWOB, totaling 6 seconds in total for each depth point. This fast-computing feature can be used in an Auto-Driller system for real-time drilling monitoring.
- The DWOB calculated by both analytical model and FEM closely matches with measured DWOB. In the four sections, the average variation ratio for analytical model can be up to 86%, and for FEM it can be up to 91%. The average variation ratio for entire well path is 82% (Analytical Model) and 88% (FEM).
- In future research, analysis with more field drilling data is required, and further improvement/calibration for both analytical model and FEM is necessary. For instance, hookload data from TTS (torque and tension sub) should be collected, which can exclude the effect of the sheave efficiency.

References

Aarrestad T.V., Blikra H., "Torque and Drag - Two Factors in Extended-Reach Drilling", *Journal of Petroleum Technology*, September 1994.

Aadnoy B.S., Andersen K., "Friction Analysis for Long-Reach Wells", *SPE/IADC Drilling Conference*, Dallas, Texas, March 1998.

Aadnoy B.S., Fabiri V.T., Djuurhus J., "Construction of Ultralong Wells Using a Catenary Well Profile", *SPE/IADC Drilling Conference*, Miami, February 2006.

Aadnoy B.S., Djuurhus J., "Theory and Application of a New Generalized Model for Torque and Drag", *IADC/SPE Asia Pacific Drilling Technology Conference and Exhibition*, Jakarta, Indonesia, August 2008.

Aadnoy B.S., Fazelizadeh M., Hareland G., "A 3-Dimensional Analytical Model for Wellbore Friction", *Journal of Canadian Petroleum Technology*, 2010.

Brett J.F., Beckett A.D., Holt C.A., Smith D.L., "Uses and Limitations of Drillstring Tension and Torque Models for Monitoring Hole Conditions", *SPE Drilling Engineering*, September 1989.

Bueno R.C.S., Morooka C.K., "Analysis Method for Contact Forces Between Drillstring-Well-Riser", *International Petroleum Conference and Exhibition of Mexico*, 1994.

Dykstra M.W., "Nonlinear Drillstring Dynamics", *PhD Dissertation*, University of Tulsa, United States of America, 1996.

Fazelizadeh M., Hareland G., Aadnoy B.S., "Application of New 3-D Analytical Model for Directional Wellbore Friction." *Modern Applied Science*, 2010.

Hamilton W.R., "On a General Method in Dynamics", *Philosophical Transaction of the Royal Society Part II*, 1834.

Ishak G., Daily J., Miska S., "Modeling Dynamic Behavior of Bottom Hole Assemblies Containing an Underreamer", *SPE Deepwater Drilling and Completions Conference*, 2012.

Johancsik C.A., Friesen D.B, Rapier D., "Torque and Drag in Directional Wells - Prediction and Measurement", *Journal of Petroleum Technology*, 1984.

Joshi S.D., "Horizontal Well Technology", PennWell Publishing Company, Tulsa, Oklahoma, 1991.

Joshi S.D., "Cost/Benefits of Horizontal Wells", SPE Western Regional/AAPG Pacific Section Joint Meeting, May 2003.

Keith M., Cech R., Dave H., "CBM Resource Potential in the Plains Area of Alberta", SPE/CERI Gas Technology Symposium, 2000.

Lalanne M., Ferraris G., "Rotordynamics Prediction in Engineering", Second Edition, 1998.

Mitchell R.F., Samuel R., "How Good Is the Torque/Drag Model?", SPE Drilling & Completion, March 2009.

Millheim K., Jordan S., Ritter C.J., "Bottom-Hole Assembly Analysis Using the Finite-Element Method", Journal of Petroleum Technology, 1978.

Newman K. R., "Finite Element Analysis of Coiled Tubing Forces", ICoTA Coiled Tubing Conference and Exhibition, 2006.

Reiber F., Vos B.E., Eide S.E., "On-Line Torque & Drag: A Real-Time Drilling Performance Optimization Tool", SPE/IADC Drilling Conference, Amsterdam, Netherlands, March 1999.

Reddy J.N., "An Introduction to the Finite Element Method", Third Edition, McGraw-Hill, New York, 2005.

Sheppard M.C., Wick, C., Burgess, T., "Designing Well Paths To Reduce Drag and Torque", SPE Drilling Engineering, December 1987.

Stephen H., "Unconventional oil and gas resource development", Journal of Unconventional Oil and Gas Resources, 2013.

Wilson E.L., "Nonlinear Dynamic Analysis of Complex Structures", Earthquake Engineering and Structural Dynamics, 1973.

Yang D., Rahman M.K., Chen Y., "Bottom hole assembly Analysis by Finite Difference Differential Methods", International Journal for Numerical Methods in Engineering, 2008.

"Estimated Production of Canadian Crude Oil and Equivalent". National Energy Board, 2009.

“Total Crude Oil Exports (m³ and bbl) – Annual”. National Energy Board of Canada, 2009.

“Regulating Unconventional Oil & Gas in Alberta”, Energy Resources Conservation Board, 2012.